UNIVERSITAT POLITÈCNICA DE CATALUNYA
BARCELONATECH

Departament de Teoria del Senyal
i Comunicacions

Doctor of Philosophy Dissertation

Design Rules and Optimization of Electro-Optic Modulators Based on Coplanar Waveguides

by

Jose Antonio Ibarra Fuste

Supervisor: Maria Concepcion Santos Blanco

Barcelona, 2013

To my parents and my beloved wife

Acknowledgements

I would like to thank my supervisor Maria Concepcion Santos Blanco for giving me the opportunity to start my PhD, for her confidence, patience and helpful discussions. Thanks for the support during these years.

I would like to thank to the Agencia de Gestio d'Ajuts Universitaris i de Recerca (AGAUR) of the Generalitat of Catalunya.

I would like to thanks my parents and my wife Leslie for help me making this possible.

Abstract

Electro-optical traveling wave modulators (EO-TWM) are basic building blocks of the optical communications industry which is leading a revolution in the way we communicate, work and live. As a result, the demand for high-speed data transmission with low driving voltage is continuously growing up with costs that should be kept below a minimum. Besides communications, a growing number of applications for EO-TWM is continuously emerging with equally stringent requirements. This Thesis is concerned with advances in the field of systematic design and optimization of EO-TWM for coping with the industrial demands.

In EO-TWM, the accumulated electro-optic effect over the optical wave grows with the co-propagated traveling wave (TW) length, allowing to reduce the required RF driving power. However, in typical electro-optic materials for modulators, among which $LiNbO_3$ stands up, due to the natural mismatch between the velocity of the RF and the optical waves, the modulation bandwidth decreases with the TW length, giving place to a well-known trade-off. In typical $LiNbO_3$ substrates, in which this Thesis is focused, this trade-off is seen to mainly depend on the values of the electrical loss constant and the effective wave velocity mismatch in the TW structure that forms the electrodes, usually a coplanar waveguide (CPW).

Special emphasis has historically been placed on the optimized design of the CPW in EO-TWM. In this Thesis the study of closed-form expressions for the propagation parameters of CPW as a function of the geometry, has proven useful for the design and optimization procedures sought. Although some interesting approaches to closed-form formulations have been found in literature, none of them completely fulfills the desired requirements of providing a reliable yet simple description of propagation in CPW, appropriate to systematic and easy to follow design rules for EO-TWM, and therefore new simplified closed-form expressions for the CPW transmission parameters have been developed.

In a second part of the Thesis, the bandwidth-length trade-off has been examined. To date, two bandwidth-length rules have been proposed: a constant bandwidth-length product proportional to the

inverse of the velocity matching constant has been shown to govern the low-loss limit (LL), while in the velocity matching limit (VM), a constant bandwidth times squared-length rule proportional to the inverse of the squared loss constant has been found more appropriate. In this work we provide insights into the trade-off issue in EO-TWM, and a complete picture of the applicable figures of merit for every operative range. Besides the known LL and VM figures of merit, two intermediate ranges, the quasi-low loss (QLL) and the quasi-velocity matching (QVM), have been identified.

Also novel closed-forms expressions fully accounting for the effects of the skin-effect electrode loss and optical-electrical wave velocity mismatch, explicitly relating the operative bandwidth and the electrode length in EO-TWM, have been found. Novel bandwidth and electrode-length charts have been created, which constitute a useful tool for the optimization and design of this modulators.

A graphical interface tool called MZM-GIT has been built integrating the analytical optimization and design strategies developed throughout the Thesis. With the aid of the MZM-GIT, several proposals of optimized MZM designs based on practical structures described in literature, and also based on the industry trends, are made and analyzed.

Contents

1

Introduction

1.1 Motivation

Over the past decades, due to the ever-increasing demands of telecommunication services and the need of wider bandwidth, the advantages of electro-optic external modulation in fiber optic transmission systems have been firmly established. Despite recent developments in novel materials such as graphene [3] [4] [5], electrooptical polymers [6] [7] [8], barium titanate ($BaTiO_3$) [9] [10] [11] and silicon [12] [13] [14], lithium niobate ($LiNbO_3$) continues to be the common material chosen for the fabrication of electro-optical modulators due to its combination of high electro-optical coefficients and high transparency in the near infrared wavelengths used for optical telecommunication [15] [16] [17]. Also recently, the development of new micro-engineered techniques, which rely on the ferroelectric properties of $LiNbO_3$, has opened the door to a new generation of integrated devices based on $LiNbO_3$ [18] [19].

The electro-optical modulation is based on the Pockels effect, by which an applied electrical field gives rise to a phase shift on a propagating optical wave which is proportional to the electrical field amplitude. Optical phase modulations thus achieved can be converted into optical amplitude modulations either in bulk free-space arrangements that exploit the effect on the wave polarization or in integrated Mach-Zehnder interferometric configurations [15].

In contrast to lumped electrode configurations, traveling wave (TW) structures, in which the optical and radio frequency (RF) waves are made to travel collinearly, allow lower electrical driving power levels with longer modulator lengths. The parameter that quantifies the required driving power is the half wave voltage or V_π, defined as the required voltage to induce a π phase shift on the optical wave. Early designs of Mach Zehnder modulators considered a variety of transmission line structures, but presently they mainly rely on coplanar waveguides (CPW) [20] [21].

This work is concerned with integrated electrooptical CPW traveling wave Mach Zehnder modulators (MZM) which presently account for an estimated total available market of around $ 450 millions according to studies conducted by Gigoptix Company. The study will mainly consider $LiNbO_3$ as the electrooptical material, even though other materials could also be included into the analysis. Basically due to both the inherent wave velocity mismatch between the optical and the electrical waves in $LiNbO_3$ and to ohmic loss in the electrodes, low V_π achieved by long device lengths (L) is accompanied by a reduction of the operative bandwidth (B) [22] [23]. The selection of L thus exhibits a trade-off between V_π and B, which depends on the values of the RF propagation parameters in the transmission CPW line forming the electrodes [20] [21].

On the other hand, it is also important to ensure that the MZM electrical connection is well matched to the impedance of the driving source. Reference impedance of most applications of MZM is 50Ω, while typical characteristic impedance values (Z_0) of CPW over $LiNbO_3$ substrates lie around 30Ω. In order to guarantee a broadband impedance matching, the MZM design should include strategies to increase the Z_0 of the CPW transmission line forming the electrodes.

Applications of MZM are mainly, but not limited to, the optical communications field, specially in high speed and long haul links, where they have largely replaced the direct-current modulation of laser diodes. Due to their flexibility, MZM has widely spread out to a variety of uses such as providing arbitrary constellation modulators for high efficiency signal transmission [24] [25], frequency comb sources [26] [27], photonic local oscillators [28], short pulse generators [29] and a long list which includes an increasing diversity of military and space applications [18] [30] [31] [32] [33] [19].

Figure 1.1: Commercial $LiNbO_3$ MZM from Photline.

By and large, the technical trends of modern MZM point towards four directions. First trend is

addressed to increase performances in terms of high bandwidth. Commercial MZMs are fabricated to reach 10, 40 and lately 100 Gb/s. According to ElectroniCast, a leading market research and technology consultancy, in 2015, the 40 Gb/s modulator use is forecast to represent nearly 41% of the worldwide relative market share (consumption value), even though in terms of volume (number of units), the 10 Gb/s category will maintain the worldwide lead in relative market.

The second trend is to assure inexpensive control electronics, where mainly low V_π is needed. Current 40 Gb/s MZMs require about 5 V for a single drive and 3 V for dual drive, where the drivers have to be composed of a Si-based logic integrated circuit (IC) (SiGe HBT) and a driving amplifier made of a compound semiconductor such as GaAs. If the drive voltage could be reduced to less than 2 V, which is the breakdown voltage of Si-Ge, the logic ICs and drive circuit can be integrated on one simple and inexpensive Si-Ge chip [29].

The third direction is to reduce L to decrease the package size, e. g. to make the device more compact as needed for small-form-factor transponders [29] [34].

The four trend is related to the unique flexibility properties of optical modulation based on $LiNbO_3$, such as the ability to provide a wide variety of modulation functions over the optical wave by combinations of optical phase and amplitude control by electrical signals. Examples include chirp control through electrode gap asymmetry [35], and differential quadrature phase shift keying modulation (DQPSK) [24] [25].

Towards achievement of the above mentioned goals it is important to bear in mind that in MZM the parameters B, V_π and L are closely related through figure of merit trade-offs, which basically depend of the electro-optic waves velocity mismatch and the electrode loss. At the same time, it is also important to maintain a good impedance matching to driving sources. Traditionally the MZM cross-section has been tailored to increase Z_0 while n_m and α decrease.

Low permittivity buffer layers beneath the electrodes and the electro-optic substrate have been employed as a means to reduce n_m. They further allow for increases of the line impedance that help to achieve the impedance matching. The downsides are that the voltage drop across this buffer layer reduces the field intensity into the electro-optical substrate decreasing the modulation efficiency [23], and the associated bias-drift related to the flow and redistribution of electrical charge in the device structure [36] [37] [38].

Increases in the conducting electrode thickness have also traditionally been exploited to achieve the velocity matching. In this case though, a lower n_m is accompanied by a lower Z_0 value that works against the electrical impedance matching [23].

More recently, thin film electro-optical substrate designs of just a few microns have been shown to both reduce n_m and to increase Z_0 [2] [39]. Here, the challenge is to achieve the $LiNbO_3$ thickness that satisfies both requirements simultaneously while properly housing the optical guides.

Techniques such as ridge structure [40] [41] [42], etched cross-section [43] [44], back-slotted cross-section [45] [46] [47], phase reversal and domain inversion [48] [49] [50] [51] have also been common optimization strategies, Fig.(1.2).

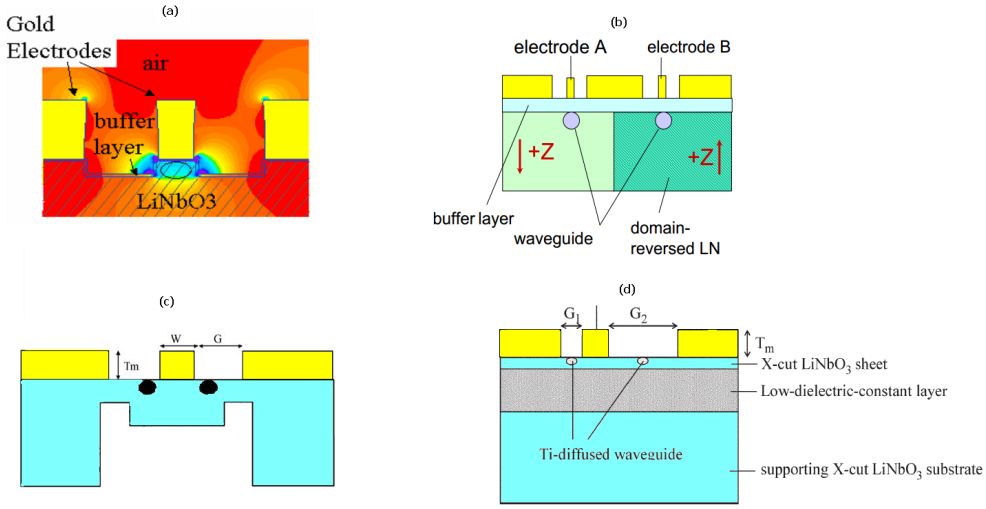

Figure 1.2: Types of MZM (a)Ridge structure [52], (b) domain inverted [52], (c) back-slotted cross-section [45], and (d) $LiNbO_3$ thin film [35].

The design and optimization of MZM can thus be regarded as a two-sided problem. On the one side there is the choice of a CPW cross-section structure which determines the transmission line propagation parameters (n_m, α, Z_0), and on the other the relationship of these parameters with the MZM system features (B, V_π, L). Therefore, a systematic approach to MZM optimization should rely on mathematical expressions and models which could bridge the gaps between design and performance parameters as sketched on Fig. (1.3). Those expressions should be simple enough for both allowing to develop an intuitive understanding of the underlying trade-offs, and also enabling smooth integration into systematic design and optimization algorithms, while at the same time showing flexibility and holding potential for encompassing a broad variety of different MZM structures and design strategies.

This is expressed graphically on Fig. (1.3), along with the chapters of the present dissertation where the relevant work on each of the sides of the problem is presented.

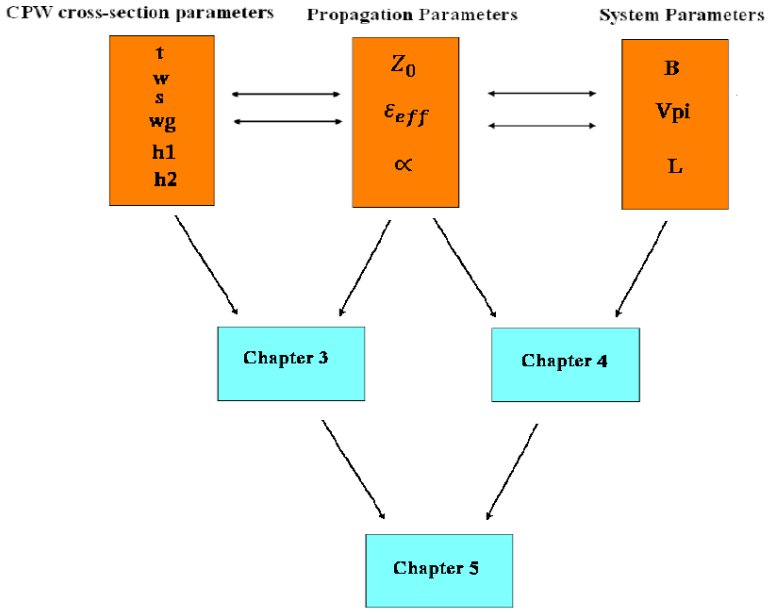

Figure 1.3: Scheme of the Thesis.

1.2 Aim of the thesis

This Thesis will focus in the optimization of MZM through development of simple models that could provide a base to build a set of easy to follow design rules and systematic analysis tools, that could help to develop present and future MZM evolution trends.

A complete and thorough revision of the field is targeted with an eye to firmly establish the fundamental concepts and definitions and to clearly define strategies that could allow to reach the full potential of state of the art technologies.

The principal goals of the thesis are:

1. A complete study of the CPW forming the MZM which could allow to derive approximated closed-form expressions for the RF propagation parameters including conductor thickness, skin effect, gap and conductor ground asymmetry, and multilayer substrates such as a $LiNbO_3$ thin film or SiO_2 buffer layer structures. These equations would constitute a powerful tool in a systematic

CPW design that would allow to optimize the MZM features mainly in terms of bandwidth and voltage driver.

The analysis of the propagation parameters of a CPW has traditionally relied on the quasi-transverse electromagnetic (TEM) approximation. Conformal mapping techniques have been exploited to obtain the propagation parameters as a function of the CPW geometry. However effects such as thick electrodes, multilayer substrates and cross-section asymmetries, which are much relevant to MZM design, are not easily included into the model with the required accuracy.

Too often, the CPW design for MZM optimization needs to depend on cumbersome and lengthy numerical electromagnetic simulations which hinder a systematic approach to the optimization of MZM and the development of intuitive insights.

The derivation of closed-form equations, embracing all the relevant effects commented before, that accurately models the behavior of the CPW as a function of the geometry, and also allows for simply addition of a variety of different structures, is key for the design and optimization of MZM.

Once the propagation parameters are clearly linked to a specific CPW geometry, it should be interesting to know how the cross-section parameters impact the achievable B and V_π. That is the goal of objective 2 of this Thesis.

2. An analysis of the bandwidth-length trade-off that could bring some light into the appropriate figures of merit and thus help to exploit the potential of a specific CPW cross-section to achieve specially targeted B and V_π values, while maintaining Z_0 matched.

   To elucidate which CPW cross-section is more suited to a specific application, a figure of Merit BL or B/V_π has been traditionally used [53] [54]. However, this has been shown to be valid only in the low-loss approximation which is not always the case of a MZM. It has been also proved that when near velocity matching is achieved, the figure of Merit is better defined as BL^2 or B/V_π^2 [55]. The intermediate cases, when the loss or velocity mismatch are not negligible, have not been contemplated to date.

   In a general case in which both losses and velocity mismatch are relevant, the $B-L$ relation is found from a numerical solution of a transcendental equation for every specific case. The aim of this objective is two-fold, on the one side we will try to find closed-form expressions that could relate B and L in a general case with both losses and velocity mismatch, and on the other we will

analyze the possible figures of merit that can be used to characterize a specific MZM cross-section in terms of achievable B and L values, and the range of validity of each figure of merit.

3. Integration of the analytical models to be developed into a systematic design and optimization tool which can straightforwardly be used to define optimized MZM structures with enhanced performance.

1.3 A thesis overview

The thesis is organized in the following manner: Chapter 2 gives a review of the state of the art of MZM, embracing its fundamentals, i. e. the mechanism of electro-optical modulation based in the Pockels effect [15], the frequency response and figures of merit. The overlap integral and its impact in the modulator performance is described. The CPW forming the electrodes is presented, emphasizing the cross-section influence in the RF propagation parameters.

Chapter 3 is devoted to analyze the presently available closed-form formulations for the CPW microwave properties and to compare with numerical simulations in commercial finite-element software HFSS in order to test their accuracy. Novel closed-form expressions for the microwave propagation parameters accounting for the main geometrical characteristics of the CPW cross-section relevant to MZM design and optimization are presented. The formulation has been validated by comparing with experimental measures available in literature, as well as with HFSS results.

In Chapter 4 novel $B-L$ closed-form equations, fully accounting for the effects of the electrodes attenuation and the electrical and optical velocity mismatch, are presented. From these, four $B-L$ trade-off figures of merit for different MZM operative ranges are identified and novel B and L charts are built and tested with experimental results found in literature.

In Chapter 5 a systematic approach to optimize the MZM cross-section is presented which combines the closed-form expressions obtained in Chapter 3 and the bandwidth and length equations of Chapter 4 in an integrated graphic interface tool. Two optimized MZM proposals, one for a broadband modulator and one for a reduced V_π, are proposed in a straightforward way using the graphic tool.

Finally, in Chapter 6 the conclusions of this work and possible future work directions are presented.

2

Basics

2.1 Introduction

This Chapter is devoted to the analysis of the basics of the MZM. In section 2.2, the fundamentals of the Pockel's electro-optic effect are reviewed. Section 2.3 deals with the overlap integral and the influence of the CPW physical geometry over it. Section 2.4 is dedicated to the principal characteristics of the CPW. In subsection 2.4.1 the finite element method (FEM) solver HFSS along with its features, is presented. As the MZM performance is strongly related to the cross-sectional CPW physical magnitudes, the influence of each one in the propagation parameters is analyzed through numerical simulations with HFSS in section 2.4.2.

2.2 Basics of MZM

The operating principle of the MZM is based on the linear electrooptic effect also known as Pockels effect, which is related to the change of the optical properties of a material under the influence of an external field at electrical frequencies [15].

Through the Pockels effect, the incremental change of the electric impermeability tensor η at optical frequencies due to the applied electric field $\vec{E}$ is given by

$$\eta(\vec{E}) = \eta_0 + r\vec{E}, \tag{2.1}$$

where r is the crystal's electrooptical coefficient, and η_0 is the linear impermeability which in a lossless media can be diagonalized in a system of reference given by the material's principal axes with elements $\frac{1}{n_x^2}$, $\frac{1}{n_y^2}$ and $\frac{1}{n_z^2}$, being n_x, n_y and n_z the principal refractive indices into each direction of the crystal

[15]. The $LiNbO_3$ is an uniaxial crystal meaning that from the three possible principal indices two of them are equal, and the third is along the direction of a symmetry axis known as the optical axis. The reference axes are usually chosen so that the optical axis follows the z direction and therefore

$$n_x = n_y = n_o, \tag{2.2}$$

$$n_z = n_e, \tag{2.3}$$

where n_o and n_e are the ordinary and extraordinary refractive indices, respectively.

The electrooptical coefficient r for $LiNbO_3$ in contracted notation is related to the tensor η as follows [15]

$$\begin{bmatrix} \eta_{xx} \\ \eta_{yy} \\ \eta_{zz} \\ \eta_{yz} \\ \eta_{xz} \\ \eta_{xy} \end{bmatrix} = \begin{bmatrix} \eta_{xx_0} \\ \eta_{yy_0} \\ \eta_{zz_0} \\ \eta_{yz_0} \\ \eta_{xz_0} \\ \eta_{xy_0} \end{bmatrix} + \begin{bmatrix} 0 & -r_{22} & r_{13} \\ 0 & r_{22} & r_{13} \\ 0 & 0 & r_{33} \\ 0 & r_{51} & 0 \\ r_{51} & 0 & 0 \\ -r_{22} & 0 & 0 \end{bmatrix} \begin{bmatrix} E_x \\ E_y \\ E_z \end{bmatrix}. \tag{2.4}$$

The most popular configuration is that where $\vec{E}$ is made to follow the optical axis, $\bar{E} = E_z\hat{z}$ [15]. In that case the crystal remains uniaxial with the same optical axis and the ordinary and extraordinary indices change their values according to

$$\frac{1}{n_o^2(E)} = \frac{1}{n_o^2} + r_{13}E_z, \tag{2.5}$$

$$\frac{1}{n_e^2(E)} = \frac{1}{n_e^2} + r_{33}E_z; \tag{2.6}$$

obtaining

$$n_{e,o}(E) = \frac{n_{e,o}}{\sqrt{1 + n_{e,o}^2 r_{e,o} E_z}} \approx n_{e,o} - \frac{1}{2} r_{e,o} n_{e,o}^3 E_z, \tag{2.7}$$

where $r_{e,o} = r_{33,13}$, and the approximation $n_{e,o}^2 r_{e,o} E_z << 1$ has been made [15].

Since $r_{33} > r_{13}$ in $LiNbO_3$ the strongest component of the optical field is usually made to also align with the z-axis of the crystal, so that the relevant optical index is the extraordinary index $n_{opt} = n_e$

[15]. Once the optical signal is modulated in phase in one or both arms of a Mach Zehnder structure, the output signal is recombined resulting in an amplitude modulation, Fig. (2.1).

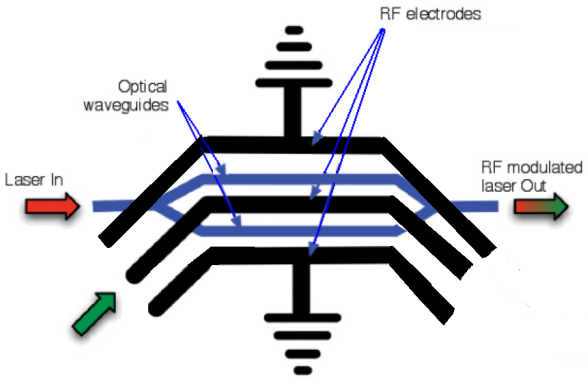

Figure 2.1: Basic electro-optic modulator structure.

A voltage signal is applied to the CPW. In a frame of reference moving with the photon velocity, the TW voltage can be written [18]

$$V(t,z) = V_0 e^{[j(2\pi f t - \beta z) - \alpha_0 \sqrt{f} z]}, \tag{2.8}$$

where V_0 is the amplitude of the wave; f is frequency and α_0 is the field attenuation coefficient in Nepers per unit length at 1 GHz, β is the propagation constant of the fundamental mode and z is the direction of propagation.

The accumulated phase shift after traveling along each of the MZM arms of length L is (Appendix B)

$$\Delta\phi(f) = -\frac{\pi}{\lambda_0} n_{opt}^3 r_{33} \frac{\Gamma}{s} \int_0^L V_0 e^{-j(2\pi\nu f - \alpha_0\sqrt{f})z} dz, \tag{2.9}$$

where $\nu = \frac{|n_m - n_{opt}|}{c}$ is the group velocity mismatch parameter, being n_m the effective microwave index and c the speed of light in vacuum, and Γ is the overlap integral [56] given as

$$\Gamma = \frac{s}{V_0} \frac{\int E_m \left|E_{opt}^2\right| \, ds}{\int \left|E_{opt}^2\right| \, ds}, \tag{2.10}$$

where E_m and E_{opt} are respectively the electrical and optical fields, and s is the electrode gap.

The DC voltage V_π, is often given as a measure of the efficiency of MZM. Defined as the required DC voltage over the electrodes to induce a π phase shift, following from (2.9), it is written by

$$V_\pi = \frac{s}{L}\frac{\lambda_0}{r_{33}n_{opt}^3\Gamma}. \tag{2.11}$$

The small-signal modulation response of a MZM with Z_0 matched, for a dominant conductor attenuation is given as (Appendix B) [54]

$$M(f) = \left|\frac{\Delta\phi(f)}{\Delta\phi(0)}\right| = e^{\frac{-\alpha_0\sqrt{f}L}{2}}\left[\frac{\sinh^2\left(\frac{\alpha_0\sqrt{f}L}{2}\right)+\sin^2\left(\pi f\nu L\right)}{\left(\frac{\alpha_0\sqrt{f}L}{2}\right)^2+\left(\pi f\nu L\right)^2}\right]^{1/2}. \tag{2.12}$$

In the characterization of the modulation speed of MZM two different definitions of B can be found, namely the electrical and the optical 3 dB bandwidth, verifying respectively $M(B^e) = 1/\sqrt{2}$ and $M(B^o) = 1/2$, in (2.12) [54]. This distinction reflects the fact that in conventional Intensity Modulation and Direct Detection (IM/DD) optical transmission systems, the electrical modulation signal B (B^e) differs from the B of the resulting modulated signal (B^o). This is a direct consequence of the square-law nature of electro-optical conversions, based on one-to-one electron-photon interchanges. While B^e bears the most significant relevance in terms of the data velocity that can effectively be conveyed, some authors prefer to give the B^o. Therefore, to be able to compare with measures, in this work we will provide results for both B^e and B^o.

The configuration and the cut of the $LiNbO_3$ crystal forming the substrate of the MZM is a key factor for its performance. The orientation of the optical axis determines the location of optical guides relative to the CPW electrodes. If the crystal is cut so that the optical axis lies in the plane of the crystal, we say the crystal has an x-cut, while z-cut refers to a crystal with optical axis perpendicular to the crystal plane. Fig. (2.2) shows the x-cut and z-cut different variants for the CPW cross-section, with the E field always pointing in the direction of the optical axis (z-axis). As shown, the optical waveguide should be placed in the substrate in the gap zone for a x-cut configuration and beneath the electrodes for z-cut. Because the electrodes are placed on top of the waveguides, z-cut devices require a buffer layer, generally SiO_2, to minimize the attenuation of the optical mode due to metal absorption [17].

In x-cut, a buffer layer is not required, even though it can be used to help the wave velocity matching at the expense of a reduction in Γ. The topology of the x-cut naturally results in a push-pull configuration and therefore is intrinsically chirp-free [17]. This does not apply to the z-cut configuration in which the E field is twice as intense below the hot conductor and therefore the difference between Γ in each z-cut arm results in a frequency chirp. The pre-chirp characteristic has been exploited to compensate for chromatic dispersion of optical fibers. In this sense, it is worth noting that asymmetrical

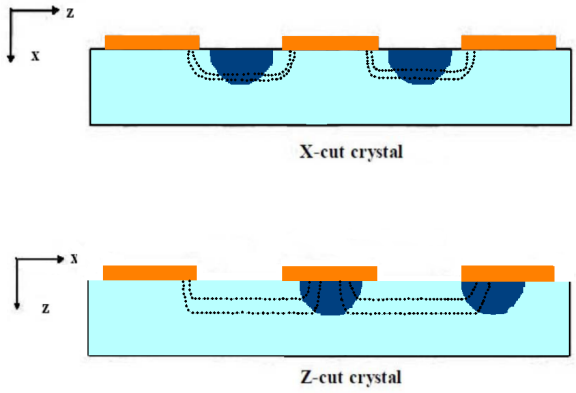

Figure 2.2: X-cut and Z-cut CPW Mach Zehnder cross-section.

CPW designs are useful for chirp control strategies [35]. Another common configuration is the dual drive CPW topology that achieves a factor of 2 in the overlap integral at the expense of higher design complexity, Fig. (2.3) [17] [35].

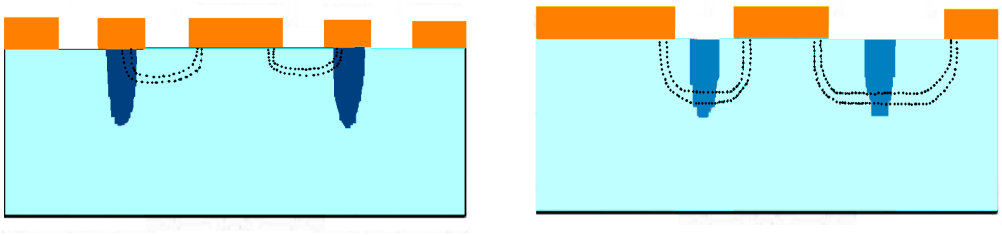

(a) (b)

Figure 2.3: (a) Dual drive CPW configuration (b) asymmetric configuration.

2.3 Overlap Integral Factor

The efficiency of an electro-optic modulator depends strongly on the overlap between the external electrical and optical fields. This overlap is determined by the geometry of the CPW and the position of electrodes relative to the optical guides. Optimizing the electrode spacing and their relative placement with respect to the optical waveguides is one of the key factors to improve the modulators performance [56] [57] [58] [59].

In this section we analyze the overlap integral, the influence of the geometrical CPW parameters on it, and therefore on the V_π, and how to increase its magnitude.

Definition on Γ is given in expression (2.10). In order to get an estimation of its value, we consider the available analytical expressions of the optical and electrical fields in the electrooptical substrate.

Starting with the modeling of the optical field, at present high quality optical waveguides are routinely obtained through two well-established technologies, Ti:in-diffusion and proton exchange [17] [18]. It has been shown that the fundamental mode field profile of the optical field of the weakly guiding mode in those waveguides can be well represented by the Hermite-Gaussian function [56] [57] [60].

$$|E_{opt}(x,y)|^2 = \frac{4y^2}{w_x w_y^3 \pi} e^{(-\frac{x-p}{w_x})^2} e^{(\frac{y}{w_y})^2}, \tag{2.13}$$

where p is the peak position of the optical field in the lateral direction, and w_x and w_y are width parameters in x and y directions, respectively.

While the x dependence of the field is well approximated by a Gaussian function, the y dependence is best described by the Hermite-Gaussian function since the guided mode field is very weak at the surface of the crystal. The function (2.13) is normalized for a unity integral over the infinite half space $0 < y < -\infty$, $-\infty < x < \infty$ [57].

As for the electrical field we will rely on a conformal approach which yields the expressions for the electrical field for coplanar strip electrodes [56]

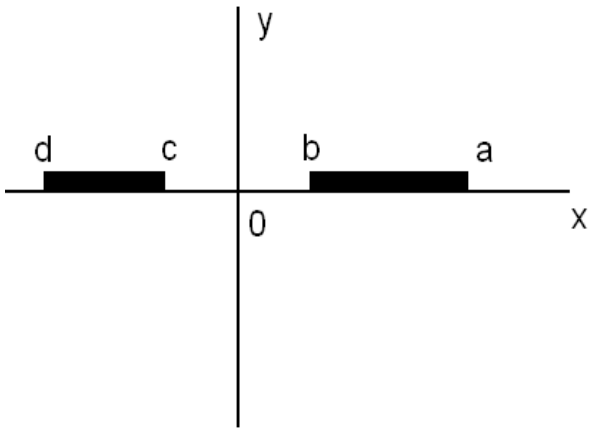

Figure 2.4: Coplanar strip electrodes.

$$E_x = \frac{V}{|2K(k)|} Im\left(\frac{dw}{dz}\right), \tag{2.14}$$

$$E_y = -\sqrt{\frac{\epsilon_x}{\epsilon_y}} \frac{V}{|2K(k)|} Re\left(\frac{dw}{dz}\right), \tag{2.15}$$

with

$$k = \left[\frac{(a-b)(c-d)}{(a-c)(b-d)}\right]^{1/2}, \tag{2.16}$$

$$\frac{dw}{dz} = \frac{[(a-c)(b-d)]^{1/2}}{(z-a)^{1/2}(z-b)^{1/2}(z-c)^{1/2}(z-d)^{1/2}}, \tag{2.17}$$

$$z = x + j(\sqrt{\varepsilon_x/\varepsilon_y})y, \tag{2.18}$$

where V is the voltage and $K(k)$ is the complete elliptic integral of the first kind. For z-cut substrate $\epsilon_x = 43$ and $\epsilon_y = 28$ while $\epsilon_x = 28$ and $\epsilon_y = 43$ for x-cut. The microwave field (E_m) will be E_x and E_y for the x-cut and z-cut structures, respectively.

Results for Γ through numerical computation of (2.10), using the E_{opt} and E_m expressions of (2.13) and (2.14)-(2.18) were obtained. As a validity check of our estimation of Γ we were able to reproduce the results for the symmetric x-cut CPW structure analyzed in [56]. Table 2.1 shows the characteristics of the CPW electrodes and the optical guide.

Parameter	Value
w (μm)	4
s (μm)	6
w_x (μm)	2
w_y (μm)	2

Table 2.1: Parameters of the CPW and the optical guides of [56].

Fig.(2.5) shows the Γ trend versus the peak position p along the x direction. Our numerical results match perfectly with outputs of Fig.8 of [56]. The plot agrees with the statements of [56] and [57], where it was pointed out that the maximum Γ is obtained approximately when the optical waveguide is placed in the middle of the electrode gap, with some shift toward the inner electrode edge where the electric field is higher. For this structure, the optical guide is in the center of the electrode gap when $p = w/2 + s/2 = 5\mu m$, and the highest value of Γ is reached when $p = 4\mu m$.

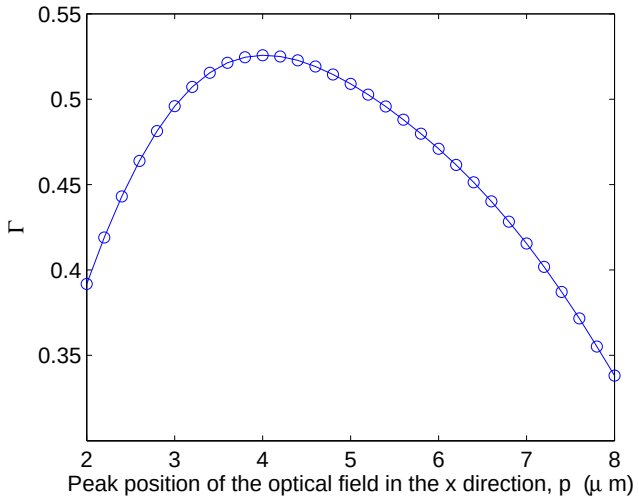

Figure 2.5: Overlap integral factor for the CPW on x-cut $LiNbO_3$ of [56].

For z-cut devices, conversely, the maximum Γ occurs when the inner edge of the electrodes is aligned with the optical waveguides [56] [57].

Using the above explained numerical computation of Γ, we analyzed the influence of the CPW parameters on its value. In Fig. (2.6a) and (2.6b) the overlap integrals for a x-cut branch of the CPW configuration of table 2.1, versus the electrode gap s and hot electrode width w are plotted, respectively, for a optical waveguide placed at the center of the gap.

As shown, Γ increases with s up to a maximum value ~ 0.55 , and then it remains almost constant. A similar behavior is observed as a function of the hot electrode width.

A first look to the graph of Γ of Fig. (2.6a) may induce to the idea that for $s < 8\mu m$ the efficiency of the MZM is reduced as Γ is decreased. This statement is not correct due to the fact that rather than Γ alone, V_π is dependent of the Γ/s ratio, as seen in (2.11) [56]. In Fig. (2.7) the ratio Γ/s against gap width is displayed, showing bigger values of Γ/s for smaller values of s, which translates into a lower V_π.

The buffer layer is also a factor of great impact in the Γ. An analysis reported by Burns et al. in [61] shows that the impact of the buffer layer on Γ may be taken to account using a correction factor due to the electric field reduction (EFR) of the form [60]

$$EFR = \frac{s}{2\varepsilon_1 \cdot \frac{h_2}{\varepsilon_2} + s}, \tag{2.19}$$

where s is the electrode gap, ε_1 and ε_2 are the dielectric constant of the $liNbO_3$ and the buffer layer, respectively, and h_2 is the thickness of the buffer layer.

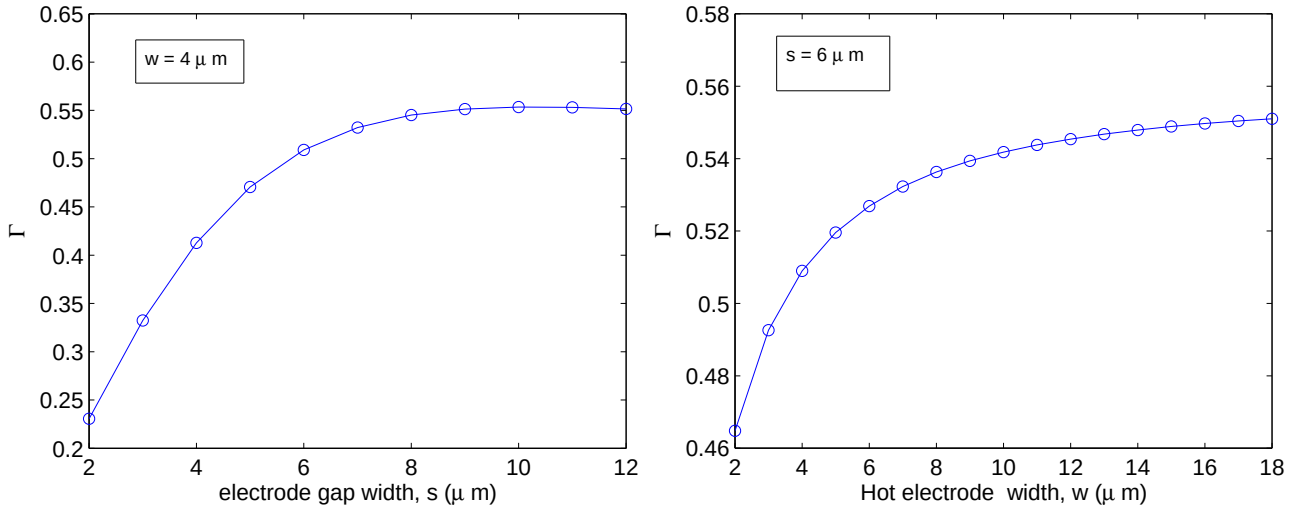

(a) (b)

Figure 2.6: Overlap integral Γ for a x-cut branch against (a) electrode gap width with $w = 4\mu m$ and, (b) hot electrode width with $s = 6\mu m$. The peak position of the optical field, p, was always taken at the center of the gap.

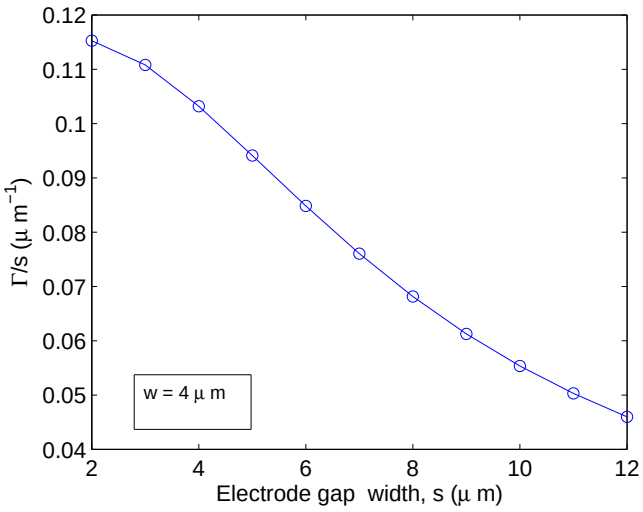

Figure 2.7: Relation between Γ/s and s for a x-cut branch with $w = 4\mu m$.

Using that result, we will estimate the Γ of a MZM structure with a buffer layer Γ_b, as the Γ from numerical computation of (2.10) using (2.13), and (2.14) to (2.18), and the EFR as $\Gamma_b = EFR \cdot \Gamma$.

The electrode gap width has also an important effect in the electric field value in buffered MZM. The values of Γ/s against s, for a SiO_2 buffer layer depth of $0.5\mu m$ and $1\mu m$ are plotted in Fig. (2.8). As shown, the value of Γ/s has a peak for $s = 6\mu m$ and $s = 6.5\mu m$, respectively. In both cases the change between the values of Γ/s for $s = 2\mu m$ and $s = 6\mu m$ is around 50%.

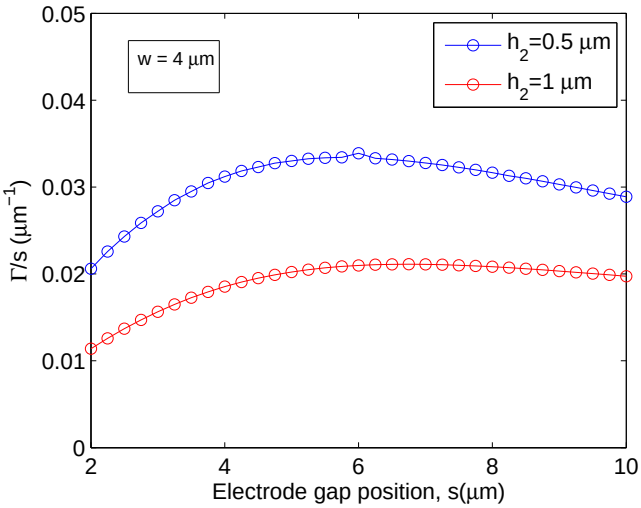

Figure 2.8: Γ/s against s for a SiO_2 buffer layer x-cut structure. The p position is fixed in the middle of the gap.

As observed, the values of s and h_2 are relevant to the V_π. Optimization of MZM performance in terms of V_π therefore comes through proper design of the CPW line electrodes. But as we know, the CPW geometry also has an impact on other MZM parameters through the values of α, Z_0 and n_m. Next section thus is devoted to an analysis of the CPW transmission line that basically allows to establish the main dependences of the propagation parameters on the CPW geometry in order to shed some light into potential design strategies for MZM optimization.

2.4 Coplanar waveguides

The CPW, proposed by Wen [20] in 1969, is a line composed by a center strip with two parallel grounded electrodes over a substrate material, as shown in Fig. (2.9). In order to reduce loss at RF frequencies these electrodes are commonly made of gold [17].

The configuration of uniplanar electrodes allows easy connections, and makes the thickness of dielectric less critical than in microstrip and stripline, thus eliminating the requirement for backside wafer processing and significantly lowering the fabrication costs [62]. In addition, the CPW line is less dispersive than microstrip offering an extended frequency range for TEM behavior [63].

2.4.1 Numerical analysis of CPW

In the context of this Thesis, the software HFSS, which is a commercial solver for electromagnetic structures, has been extensively used to get numerical results for the characteristics of the wave prop-

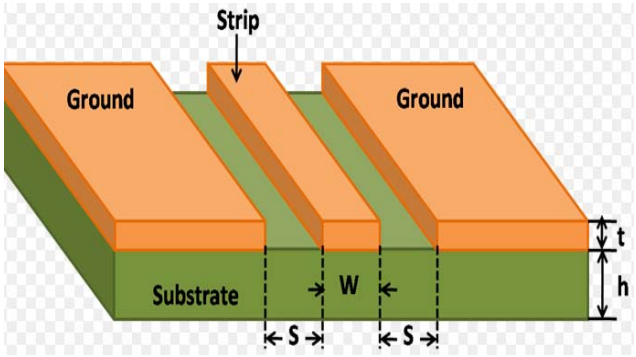

Figure 2.9: Coplanar waveguide.

agation along the CPW line structure. This software is widely used in the field of RF research [64] [65].

In order to generate an electromagnetic field solution, HFSS employs the finite element method (FEM). In general, FEM divides the full problem space into many of smaller regions (mesh) and represents the field in each sub-region (element) with a local function.

By default, the interface between all 3D objects and the background is a perfect E boundary through which no energy may enter or exit. Wave ports are typically placed on this interface to provide a window that couples the model device to the external world. HFSS assumes that each defined wave port is connected to a semi-infinitely long waveguide that has the same cross-section and material properties as the port.

The usual restrictions for a correct HFSS simulation in terms of wave port position and dimensions have been taken to account. Referring to Fig.(2.9), these can be summarized as follows:

- The port width should be no less than 3 times the overall CPW width, or $3(2s + w)$.
- The port height should be no less than 4 times the dielectric height, $4h$.
- The wave port should be centered horizontally on the CPW trace; if the port is on GCPW (grounded CPW), the port bottom edge should lie on the substrate bottom ground plane; if the port is on ungrounded CPW, the port height should be roughly centered on the CPW metal layer.

- The wave port outline must contact the side grounds (all CPWs) and bottom ground (GCPW) and should not exceed $\lambda/2$ in any dimension, to avoid a rectangular waveguide modal excitation. The range of frequency that will be used in the context of the Thesis is up to 100 GHz. This is very important for the wave port dimensions and for the radiation box used in the simulations.

Even though HFSS allows to explicitly take into account the anisotropy of $LiNbO_3$, no significant differences have been observed between HFSS simulations considering anisotropy and those employing the equivalent quasi-static isotropic relative dielectric permittivity given by $\varepsilon_r = \sqrt{\varepsilon_{11}\varepsilon_{33}} \approx 34.7$ [66], as displayed in Fig. (2.10). Therefore, in order to gain simplicity and rapidness in simulations, the equivalent quasi-static isotropic dielectric permittivity approach will be used along the Thesis.

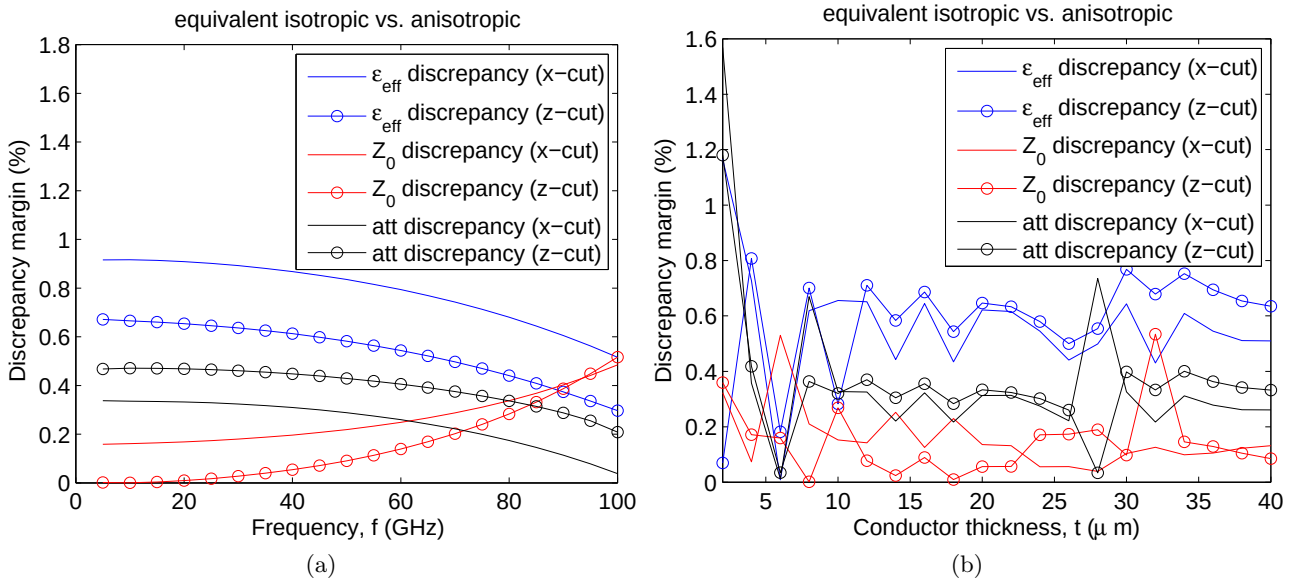

Figure 2.10: Discrepancy margin of modeling the usual quasi-static isotropic relative dielectric permittivity equivalent versus an anisotropic substrate.

2.4.2 Effects of the CPW cross-section over the RF propagation parameters

In order to gain insight into the effects of the typical CPW cross-section over the RF propagation parameters, a series of numerical experiments have been carried out in HFSS. Table 2.2 depicts the cross-sectional characteristics of a reference CPW that will be used as a benchmark along the Thesis. These values are in the usual range of typical MZM designs, where w is the hot electrode width, s is the gap between electrodes, t is the electrode thickness, w_g is the ground electrode width, h_1 is the lower

substrate layer thickness, and h_2 is the thickness of the upper substrate underneath the electrodes, as shown in Fig. (2.11). The electrode material is gold.

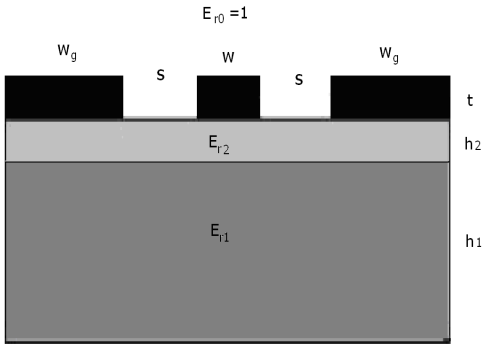

Figure 2.11: CPW cross-section geometrical parameters.

Parameter	Value
w (μm)	18
s (μm)	15
t (μm)	10
w_g (μm)	100
h_1 (μm)	50

Table 2.2: Physical parameters of the reference CPW.

Table 2.3 shows a general trending of the RF propagation parameters with the CPW cross-section parameters as observed in HFSS simulations, for the reference CPW, as shown in Fig. (2.11).

The up-facing arrow in the table means that the parameter shows an increasing trend while a down-facing arrow means the opposite.

	t ↑	s ↑	w ↑	h_2 (buffer) ↑	h_2 (thin film) ↑	w_g(50-200)↑	w_g (≥200)↑	h_1 (≥100) ↑
Z_0	↓	↑	slowly ↓	↑	↓	slowly ↓	const.	const.
n_e	↓	↓	slowly ↑	↓	↑	slowly ↓	const.	const.
α	↓	↓	slowly ↓	↓	↑	slowly ↓	const.	const.

Table 2.3: Variation of the propagation parameters with the changes in the physical ones.

As observed, t, s and h_2 are the parameters with a greater impact over the RF propagation parameters, but while the increase in h_2 is beneficial for both velocity and impedance matching points of view, increasing t improves the velocity matching but has a detrimental effect over Z_0. The trends observed as s is increased are similar to those in h_2, with the additional effect of a V_π increase coming from the reduction in the Γ/s ratio (see Fig. 2.7).

2.5 Summary

This Chapter has presented a review of the fundamentals of MZM. The geometry of the CPW has been identified as a key factor for the optimization of MZM. In general terms, it can be said that a laudable goal in MZM design s to always try to decrease α and ν and maintain Z_0 as close as possible to 50Ω. But at those conditions are difficult to reach simultaneously, the key problem is to find the appropriate balance in order to achieve a targeted performance. The influence of the CPW cross-section geometry on the MZM performance has been assessed, on the one hand by HFSS simulations of the RF propagation parameters and on the other by numerical computation of the overlap integral in order to determine its impact over the MZM driving power.

3

Closed-Form Expressions for CPW

3.1 Introduction

This Chapter focuses on finding closed-form approaches for the CPW propagation parameters (ε_{eff}, Z_0 and α) for systematic MZM design and optimization. To that goal, we first analyze in section (3.2.1) the most relevant closed-form expressions proposed in literature and test them using HFSS simulations.

The approaches analyzed here are based on extensions of conformal mapping techniques, curve fitting and empirical formulations such that the expressions usually only cover the quasi-TEM range and therefore two high frequency extension formulations are reviewed in subsection (3.2.5) [67] [68].

Novel closed-form expressions for ε_{eff}, Z_0 and α of CPW are derived in section (3.3), and an extended formulation including bi-layered substrates and asymmetry is presented in section 3.4.

An analysis of the new model performance through HFSS benchmarking and with measured results of experimental designs extracted from literature is carried out in section (3.5).

3.2 Closed-form approaches

Traditionally the CPW analysis has relied on conformal mapping techniques (CM) [69], which do not provide an easy way to include the electrode thickness, a key feature for a good MZM performance, as pointed out in previous chapters [17] [70]. Also as a consequence, the conductor attenuation is specially difficult to include in the formulas. The CPW line is basically affected by three kinds of attenuations: conductor loss, usually called skin effect loss, dielectric loss, and radiation loss which is only relevant

for frequencies over 200 GHz [67] [71] [72], thus the radiation loss will not be included in the context of this Thesis.

Other approaches have included the effect of the electrode thickness through empirical formulation and curve fitting. The expressions developed by Chung et. al. [73] and Heinrich [74] are analyzed in this Chapter. Since the quasi-TEM expressions are the base of these closed-form formulas, we start the analysis with them.

3.2.1 Quasi-TEM equations

The quasi-TEM expressions of ε_{eff}, Z_0 and α of a transmission line, as a function of the distributed line elements, are the base of a great number of closed-form approaches for CPW. We begin by reviewing their fundamentals. As seen from the derivation contained in Appendix C, they can be written as

$$\varepsilon_{eff} = c^2 LC, \tag{3.1}$$

$$Z_0 = \sqrt{\frac{L}{C}}, \tag{3.2}$$

$$\alpha = \frac{R}{2Z_0} + \frac{GZ_0}{2}, \tag{3.3}$$

where c is the speed of light in vacuum; R, G, L and C are the resistance, conductance, inductance and capacitance per unit length of the line, respectively. In order to get closed-form expressions for (3.1), (3.2) and (3.3), we consider that

$$L = L_{int} + L_{out}, \tag{3.4}$$

$$C = C_0 + C_s, \tag{3.5}$$

$$R = \omega L_{int}, \tag{3.6}$$

$$G = \omega C_s tan\delta, \tag{3.7}$$

where L_{out} is the contribution to inductance coming from the fields outside the conductors; L_{int}, also known as skin-effect inductance, is the contribution to inductance coming from the fields inside the

conductors; C_0 is the free-space capacitance of the line in the absence of dielectric; C_s is the dielectric layer capacitance; ω is the angular frequency and $tan\delta$ is the dielectric loss tangent.

For non-magnetic dielectrics the external capacitance and the free-space capacitance are related through

$$L_{out} = \frac{1}{c^2 C_0}. \tag{3.8}$$

The zero thickness assumption in CM implies a null resistance (R) and internal inductance (L_{int}) in expressions (3.6) and (3.4). Therefore the conductor attenuation is considered zero, thus reducing the problem of getting CM closed-form expressions to that of finding two cross-section capacitances: C_0 and C_s [69] [75] [76] [77] [78].

Next subsections are devoted to the conformal mapping approach [69], Chung-Chang [73] and Heinrich formulas [74]. Several simulations will be carried out to assess the validity of each approach. To that end, a parameter accounting for the agreement between the approach under analysis and HFSS simulated results will be defined as Discrepancy Margin (DM) given by

$$DM(approach)\% = 100 \left| \frac{R(HFSS) - R(approach)}{R(HFSS)} \right|, \tag{3.9}$$

where R(HFSS) and R(approach) are the results for a particular parameter of the HFSS and the approach, respectively.

3.2.2 Conformal mapping formulation

The CM has traditionally been used to obtain analytical closed-form expressions for CPW involving elliptical integrals. CM techniques provide a convenient means to analyze a great variety of different CPW cross-sections, but a fundamental drawback is the assumption of infinite dielectric substrate and zero metalization thickness.

Using these assumptions, $\alpha \approx 0$, and following equations (3.1) and (3.2), ε_{eff} and Z_0 are simplified to

$$\varepsilon_{eff} = \frac{C}{C_0}, \tag{3.10}$$

$$Z_0 = \frac{1}{c\sqrt{CC_0}}, \tag{3.11}$$

Fig. (3.1) features a CPW cross-section showing the electrical field lines and the partial distributed capacitances relevant to (3.10) and (3.11). The C_0 is the result of the parallel association of four equal partial capacitances $C_0^{'}$, corresponding to the fields into each of the four symmetrical quarter planes in which the cross-section is divided, $C_0 = 4C_0^{'}$, while C_s comes from the parallel association of two identical capacitances, due to the symmetry, between the strip and the lateral planes, $C_s = 2C_s^{'}$ over an equivalent substrate assumed to have permittivity $(\varepsilon_r - 1)$ [69].

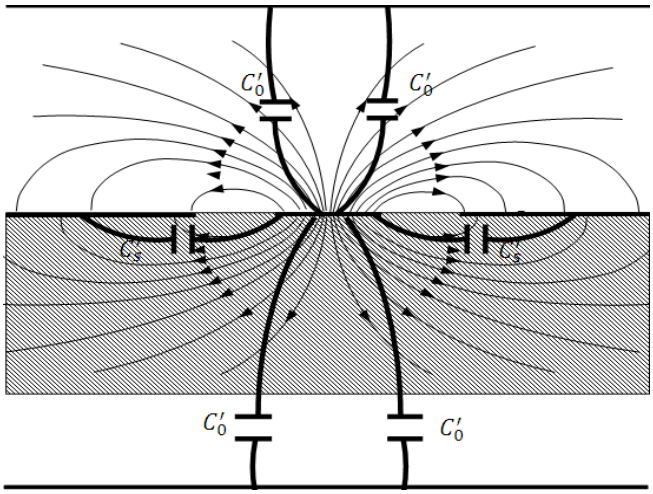

Figure 3.1: CPW cross-section field distribution and partial capacitances.

All these capacitances are computed using CM, and are given by

$$C_0 = 4\varepsilon_0 \frac{K(k_0)}{K(k_0^{'})}, \tag{3.12}$$

$$C_s = 2\varepsilon_0(\varepsilon_r - 1)\frac{K(k_1)}{K(k_1^{'})}, \tag{3.13}$$

with ε_0 the electric permittivity of free space, ε_r the dielectric constant and $K(k)$ the complete elliptic integral of the first kind which operates over the parameters k that are given by

$$k_0 = \frac{w}{w+2s}\sqrt{\frac{w_g(w+2s+wg)}{w_g(w+2s+w_g)+s(s+w)}}, \tag{3.14}$$

$$k_1 = \frac{\sinh(\pi w/4h)}{\sinh(\pi(w+2s)/4h)}\sqrt{\frac{\sinh^2[\pi(w/2+s+wg)/2h]-\sinh^2[\pi(w/2+s)/2h]}{\sinh^2[\pi(w/2+s+w_g)/2h]-\sinh^2(\pi w/4h)}}, \tag{3.15}$$

$$k_0^{'} = \sqrt{1-k_0^2}, \tag{3.16}$$

$$k_1^{'} = \sqrt{1 - k_1^2}, \tag{3.17}$$

where w is the strip width; s is the gap width; w_g is the ground conductor width and h is the substrate thickness, as shown in Fig. 2.9.

The CM, despite its simplicity and the ease with which different geometries such as ridge, back slotted structures and multi substrate layers can be added, does not provide an easy way of including the thickness of the electrodes.

In order to assess the validity range of the CM as the conductor thickness grows, several numerical simulations were performed, comparing the results versus HFSS. Fig. (3.2) shows the $DM(CM(\varepsilon_{eff}, Z_0))$ of the outcomes of (3.10)-(3.17) for the reference CPW (table 2.2) against t.

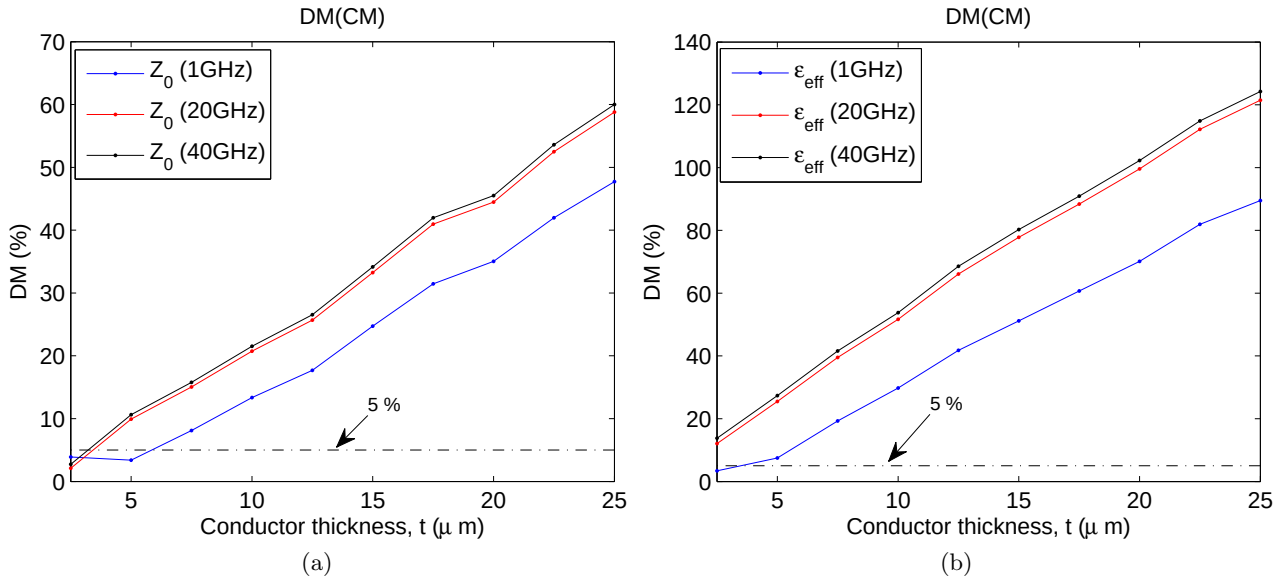

Figure 3.2: $DM(CM)$ for (a) Z_0, and (b) ε_{eff} versus t for the reference CPW of table 2.2.

As observed, setting as benchmark a $DM < 5\%$ the behavior of CM is only acceptable for low frequencies and thin conductors, not efficiently covering the usual range of frequency and electrode thickness of MZM. Though CM does not fully account for all relevant effects in MZM, it is a good start point to get improved closed-form expressions that actually take all these parameters into account.

Some authors [79] [80] suggest to include the effect of electrode thickness in a similar way to that used for microstrip, i. e. to consider that the effect of conductor thickness can be modeled by an effective increment of w and a reduction of s. However, due to the significant difference in terms of field lines between the microstrip and the CPW lines it is not clear that such an effective width

increase concept can be exported to CPW [81]. In fact, HFSS simulations have revealed remarkable inaccuracies in [82].

3.2.3 Chung-Chang formulation

Chung et. al. in [73], proposed a closed-form formulation for the propagation parameters of a CPW based on CM and some empirical coefficients, to include the effect of the electrode thickness.

The capacitances C^t and C_0^t are given by

$$C^t = 2\varepsilon_0(1+\varepsilon_r)\frac{K(k)}{K(k')} + 2C_t, \tag{3.18}$$

$$C_0^t = 4\varepsilon_0\frac{K(k)}{K(k')} + 2C_t, \tag{3.19}$$

where the expression for the extra capacitance C_t which is found through fitting and empirical values, given by

$$C_t = \pi\varepsilon_0\frac{a_1 - a_2\ln(w/g) + a_3\ln(a_4 + t/g)}{\ln(4g/t) + \frac{1}{8}(t/g)^2}, \tag{3.20}$$

where $a_1 = 0.49254$, $a_2 = 0.01709$, $a_3 = 0.21918$ and $a_4 = 0.10357$.

Fig. (3.3) shows plots of $DM(Chung{-}Chang)$ for Z_0 and ε_{eff} over a sweep of t for different f, using the reference CPW configuration. As compared with Fig. (3.2) this method yields an improvement in terms of DM values for an extended margin of t. The method is seen to work better for the high frequency range, where for $f > 20$ GHz, DMs are kept within tolerable margins ($\sim 10\%$) up to $30\mu m$. Beyond that value of t, the DM increases dramatically and the method is not suited for MZM modeling.

3.2.4 Heinrich formulation

Heinrich in [74] calculated the elements of the quasi-TEM distributed equivalent circuit R, L, G and C by using a combination of CM, perturbation approaches and curve fitting, including the effects of non ideal conductors as well as substrate loss and finite metalization thickness. A segmentation procedure for different ranges of frequency was used to obtain the resistance and total inductance by applying a perturbation approach, while the Wheeler's incremental rule [83] was applied to obtain L_{int} from the expression of L_{out}. The segmentation procedure employed requires that $w_g > w$ and $t < (9/2)w$. Since the Wheeler rule is used, the formulation is valid when $t > 3\delta$, being δ the skin depth, given by

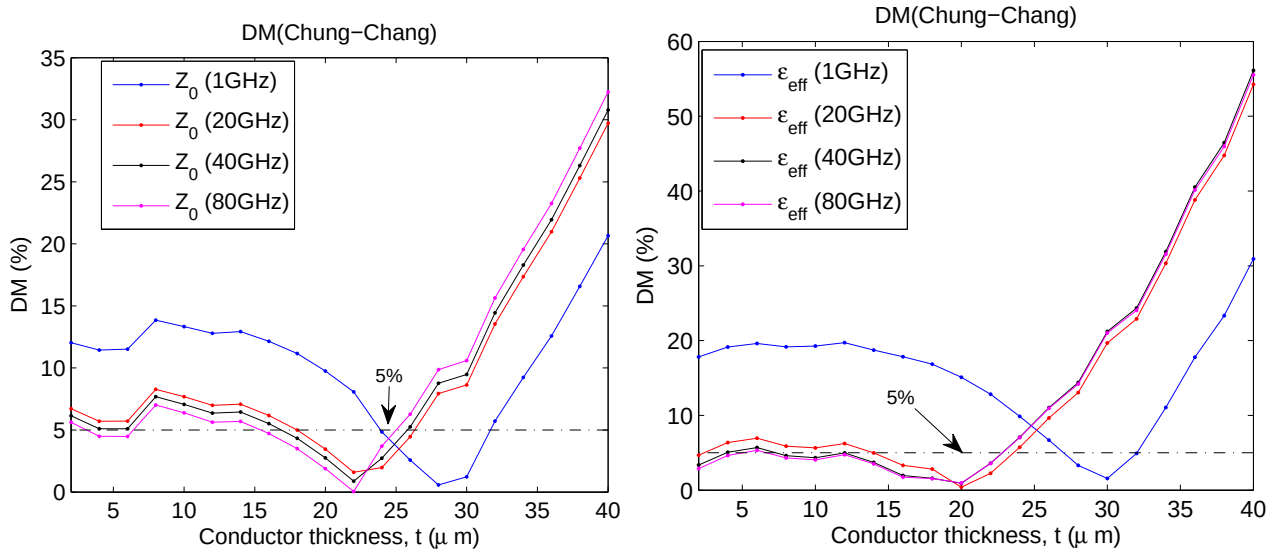

Figure 3.3: DM (Chung-Chang) for (a) Z_0 and (b) ε_{eff} versus t for the reference CPW of table 2.2.

$$\delta = \frac{1}{\sqrt{\pi f \mu \sigma}}, \tag{3.21}$$

where f is the frequency, μ the magnetic permeability and σ is the conductor conductivity.

Fig. (3.4) displays the $DM(Henrich(Z_0))$, $DM(Henrich(\varepsilon_{eff}))$ and $DM(Henrich(\alpha))$ trend for the reference CPW against t for different values of frequency. Since the formulation cannot take into account the buffer layer, we set $h_2 = 0$. We note that for all three cases the agreement is good, except for values $t < 3\mu m$, where the Wheeler bound of $t > 3\delta$ is not fulfilled. As shown, the results are better than the previous approaches with DM below 5% in the whole margin of up to $40\mu m$ thickness and 80 GHz. In the α plot, for $f = 1GHz$ the discrepancy margin seems to rise due to the problems of the Wheeler rule at low frequencies [84]. But it is only for very low f and t ($f < 1$ GHz, $t < 3\mu m$), that the method fails to predict the CPW propagation parameter values, and therefore we conclude that the Heinrich method is appropriate for accurate modeling of MZM. As a drawback we note that the formulation is cumbersome and that variation of the CPW basic structure, such as for example gap symmetries or bi-layered substrates are not easily included.

All the closed-form approaches analyzed rely on a quasi-TEM model while the ranges of f of interest to MZM reach up to 100 GHz. In the next subsection, in order to extend beyond the quasi-TEM range the evaluation of ε_{eff}, two empirical approaches accounting for the high frequency dispersion, are reviewed.

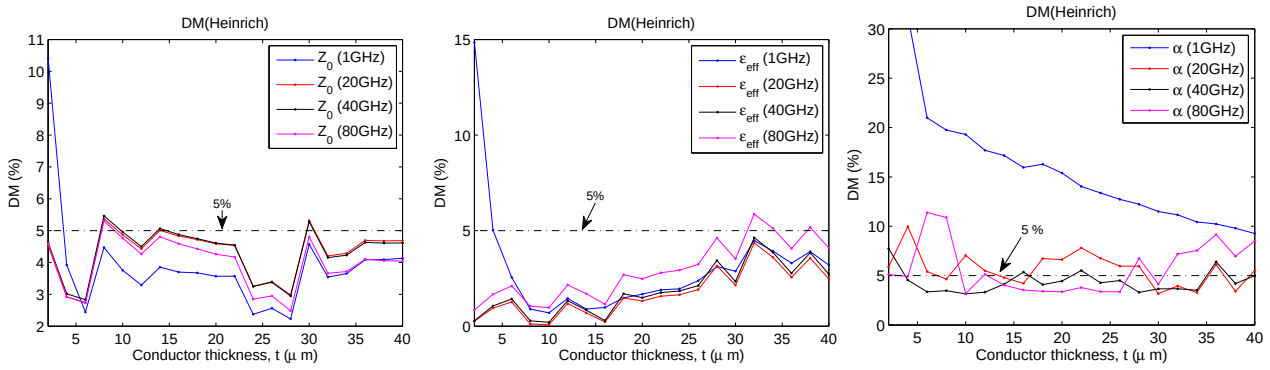

(a) (b) (c)

Figure 3.4: $DM(Heinrich)$ for (a) Z_0, (b) ε_{eff} and (c) α versus t for the reference CPW of table 2.2 with $h_2 = 0$.

3.2.5 High frequency dispersion formulation

Two analytical expressions have been found that allow to extend the TEM values of ε_{eff} to a higher frequency margin. Frankel et al. in [67] gave a semi empirical expression while Schnieder et al. [68] used a frequency domain method as a reference for fitting (see Appendix D).

Fig. (3.5) shows the DM of a sweep in frequency for ε_{eff} using each one of the high frequency dispersion extensions formulas applied over the quasi-TEM values of ε_{eff} calculated with Heinrich equation, and the case when none of them are used. With the increasing in frequency, the importance of these high frequency dispersion corrections is remarkable. It is observed that for different electrode thicknesses, the Frankel formulation is better than the Schnieder's, and therefore it will be the preferred one along this Thesis.

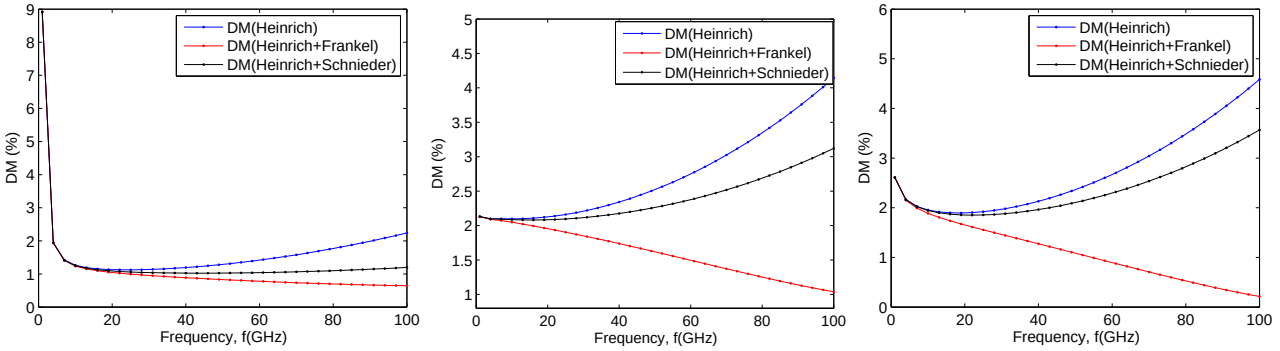

(a) (b) (c)

Figure 3.5: Discrepancy of ε_{eff} for the reference CPW of table 2.2 with $h_2 = 0$ using high frequency corrections for a) $t = 3\mu m$, b) $t = 20\mu m$ and c) $t = 40\mu m$.

Our analysis reveals that the Heinrich formulation is the most solid and efficient method found

in literature, the downside being that it is cumbersome and its use in some algorithm of design and optimization would be complicated, and that it is not flexible enough to include variations in the CPW geometry, such as asymmetry, two layer substrates, etc. Therefore in the next section a new closed-form approach for Z_0, ε_{eff} and α will be derived, including the thickness of the electrodes and the skin effect losses, in the quasi-TEM range, starting from the quasi-TEM distributed element model, (3.1), (3.2) and (3.3).

Since the new closed-form approach is based on the assumption that the contribution of t is to add a capacitance effect which can be simply calculated using a parallel plate approximation, we refer to it as the Parallel Plate (PP) model approach.

3.3 Parallel plate (PP) formulation

To start the development of the novel closed-form equations, it is good to bear in mind that two are basically the effects to consider when the CPW conductor thickness is to be taken into account. On one side, the cross-section field distribution changes, and so do the line capacitances, see Fig. (3.6). According to $L_{ext} = \frac{1}{c^2 C_0}$, the change in free-space capacitance will lead to a change in external inductance. On the other side, the skin effect field inside the conductors, gives rise to an additional line resistance R, and an internal inductance L_{int} which can be calculated from L_{ext} by using the Wheeler rule [85] [86]. Based on these ideas, in the next subsections C_0, C_s, L_{ext} and L_{int} will be obtained.

3.3.1 Free-space and substrate capacitances

We will consider that for the range of geometries of interest the capacitances due to the upper CPW space area (air region) and the lower CPW area (dielectric region), found in the $t = 0$ case (conformal mapping case), remain almost unaltered, and thus the effect of adding a certain electrode thickness will be simply to add the contribution of the capacitances coming from the fields in the space region comprised between the electrodes sidewalls, in the gap regions, as shown in Fig. (3.6).

This gap capacitance, C_g, is part of the free-space capacitance, and therefore the free-space capacitance for the $t \neq 0$ case is

$$C_0^t = C_0 + 2C_g. \tag{3.22}$$

The capacitance C_0 takes the form of (3.12), and for the gap capacitances we use the simplest form of the parallel plate capacitance, $C_g = \varepsilon_0 t/s$. The substrate capacitance C_s is obtained as in

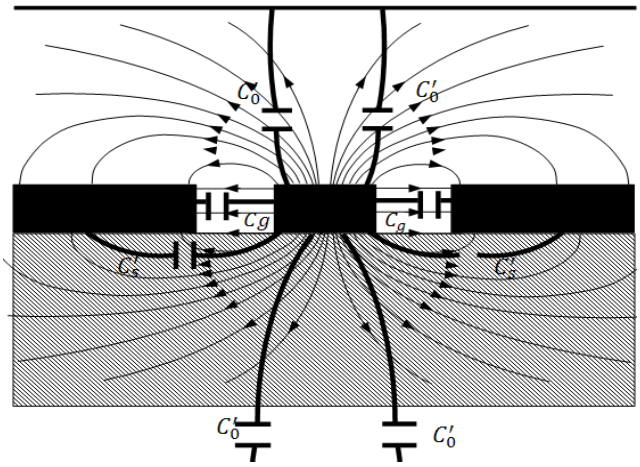

Figure 3.6: CPW cross-section field distribution and partial capacitances of a thick electrode CPW.

(3.13). These capacitances are substituted in the quasi-TEM overall capacitance given by (3.5), to finally arrive to

$$C^t = C_0^t + C_s. \tag{3.23}$$

Once the capacitances are obtained, the next step is to get the equations for L_0^t and L_{int}^t.

3.3.2 External and internal inductances

The external part of the inductance (3.8) is now obtained from the free-space capacitance of the line in the absence of dielectric as

$$L_{ext}^t = \frac{1}{c^2 C_0^t} = \frac{1}{c^2(C_0 + 2\varepsilon_0 t/s)}. \tag{3.24}$$

The above result may be exploited through the Wheeler's incremental inductance rule [83] to get L_{int}^t. Since this inductance is due to the skin-effect field penetration into the non-perfect conductors, an equivalent line model is considered where the non-perfect conductors are replaced with perfect conductors whose walls have shrunk by half the δ (3.21). Corresponding recessions in w and t, as well as extensions in s are shown in Fig. (3.7) [83]. The internal inductance values are then found as extensions of the external inductance by means of a Taylor expansion as follows

$$L_{int} = \sum_i \frac{\mu_i}{\mu_0} \frac{\delta_i}{2} \frac{\partial L_{ext}}{\partial z_i}, \tag{3.25}$$

where $\frac{\partial L_{ext}}{\partial z_i}$ denotes the derivative of L_{ext} with respect to the incremental recession of wall i; μ_i is the permeability of the dielectric i; z_i denotes the vector normal to this wall; μ_0 is the free-space permeability, and $\mu_i/\mu_0 = 1$, since we do not consider magnetic dielectrics [73] [83].

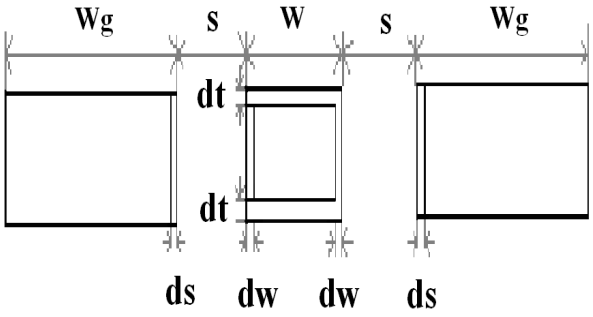

Figure 3.7: Conductor surface recessions to be considered for the calculations of inductance derivatives.

Following [83], recessions in w and t are included as well as extensions in s, see Fig. (3.7), through

$$L_{int}^{t} = \frac{\delta}{2}\left[2\frac{\partial L_{ext}}{\partial s} - 2\frac{\partial L_{ext}}{\partial w} - 2\frac{\partial L_{ext}}{\partial t}\right]. \tag{3.26}$$

Using equation (3.24) in (3.26), we get

$$L_{int}^{t} = \frac{\delta}{2\varepsilon_0 c^2(2A_0 + \frac{t}{s})^2}\left[\frac{t}{s^2} - 2\frac{\partial A_0}{\partial w} - 2\frac{\partial A_0}{\partial s} + \frac{1}{s}\right]. \tag{3.27}$$

In order to carry out the derivatives $\frac{\partial A_0}{\partial z_i}$ in (3.27), we consider the approximation for the elliptic integrals A_i of [77]

$$Ai = \frac{K(k_i)}{K(k_i')} = \left\{ \begin{array}{ll} \frac{\pi}{2\ln(\frac{4}{k_i})}; & \text{for } 0 < k_0 < 10^{-5} \\ \frac{\pi}{\ln(4\frac{1+k_i'}{1-k_i'})}; & \text{for } 10^{-5} \leq k_0 < \frac{1}{\sqrt{2}} \\ \frac{1}{4}\ln(4\frac{1+k_i}{1-k_i}); & \text{for } k_0 \geq \frac{1}{\sqrt{2}} \end{array} \right\}. \tag{3.28}$$

Solving the derivatives and rearranging (3.27) (Appendix E), finally the internal inductance is obtained as

$$L_{int}^{t} = \frac{\delta s}{2\varepsilon_0 c^2 (2A_0 s + t)^2} F, \tag{3.29}$$

with

$$F = \left\{ T \left[\frac{2s(s+w)}{w(w+2s)} - \frac{s/2}{w+2s+wg} + \frac{s/2}{s+wg} \right] + \left(\frac{t}{s} + 1 \right) \right\}, \tag{3.30}$$

where

$$T = \left\{ \begin{array}{ll} \frac{4A_0^2}{\pi}; & \text{for } 0 < k_0 < 10^{-5} \\ \\ \frac{4A_0^2}{\pi k_0'}; & \text{for } 10^{-5} \leq k_0 < \frac{1}{\sqrt{2}} \\ \\ \frac{4}{\pi (k_0')^2}; & \text{for } k_0 \geq \frac{1}{\sqrt{2}} \end{array} \right\}, \tag{3.31}$$

is a parameter that depends on the coplanar waveguide geometry.

3.3.3 PP formulation

According to the distributed line element quasi-TEM formulation and gathering results from the previous analysis, the CPW propagation parameters may be expressed as

$$\varepsilon_{eff} = c^2 (L_{ext}^{t} + L_{int}^{t})(C_s + C_0^{t}), \tag{3.32}$$

$$Z_0 = \sqrt{\frac{L_{ext}^{t} + L_{int}^{t}}{C_s + C_0^{t}}}, \tag{3.33}$$

$$\alpha = \frac{\omega L_{int}}{2Z_0} + \frac{Z_0 \omega C_s \tan\delta}{2}. \tag{3.34}$$

Using the equations for L_{ext}^{t} given by (3.24), L_{int}^{t} in (3.29), C_0^{t} in (3.22) and C_s in (3.13), and substituting in (3.32), (3.33) and (3.34), we finally get

$$\varepsilon_{eff} = \left[1 + \frac{(\varepsilon_r - 1) A_1 s}{2A_0 s + t} \right] \left[1 + \frac{\delta}{2A_0 s + t} F \right], \tag{3.35}$$

$$Z_0 = \frac{s}{2\varepsilon_0 c \sqrt{(2A_0 s + t)(2A_o s + (\varepsilon_r - 1) A_1 s + t)}} \sqrt{\left[1 + \frac{\delta}{2A_0 s + t} F \right]}, \tag{3.36}$$

$$\alpha_c = \frac{\pi f \delta s}{2\varepsilon_0 c^2 Z_0 (2A_0 s + t)^2} F + \omega \varepsilon_0 (\varepsilon_r - 1) A_1 Z_0 \tan\delta. \tag{3.37}$$

These expressions include electrode thickness, finite substrate height and finite ground plane effects. Definition of a geometrical parameter F greatly simplifies the notation and helps to derive intuitive insights. One important feature of the new PP closed-form model is that it has been developed as an extension of CM formulation, and as such, it shares the property of being able to embrace a great variety of different electrode transmission line geometries. In the next section the versatility of the PP model will be exploited to include into the formulation the cases of bilayer substrates and CPW asymmetrical cross-sections. The bilayer cross section includes both the buffer layer and the thin film MZM configurations.

3.4 Extended PP model

As we previously pointed out, the asymmetry of the electrode gap has become an usual strategy to pre-chirped MZM. The use of a buffer layer, usually SiO_2, and the use of a $LiNbO_3$ thin film have been common strategies to improve the MZM performance. However, the literature does not offer a simple, compact and effective formulation that takes these into account.

In this section, we derive an extended closed-form formulation based in the previously presented PP model which includes the effects of the asymmetry and bi-layered substrates.

3.4.1 Free-space and substrate capacitances

Fig. (3.8) represents the cross-section field distribution and partial capacitances of the CPW. The asymmetry in the "y" axis is considered by identifying with a "-" super index the parameters referring to the $y < 0$ half-space, and with a "+" super index the parameters of $y > 0$. Just as before, the problem of getting closed form expressions for the propagation parameters, is reduced to find two cross-section capacitances: the free-space capacitance of the line in the absence of dielectric (C_0) and the substrate capacitances (C_s)

As shown in Fig. (3.8), C_0 is obtained from the parallel association of C_0^-, C_0^+, C_g^- and C_g^+

$$C_0 = 2C_0^- + 2C_0^+ + C_g^- + C_g^+, \tag{3.38}$$

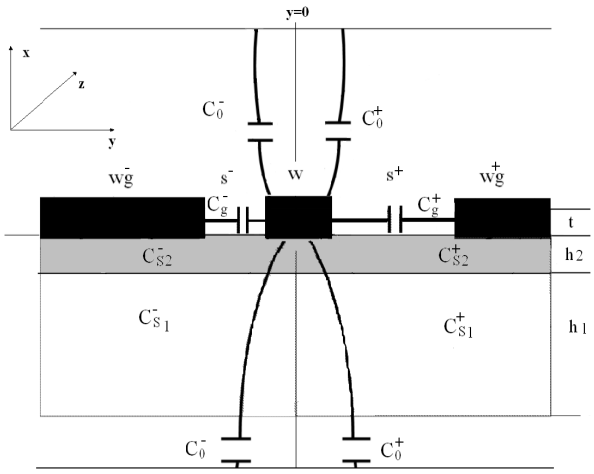

Figure 3.8: Asymmetric and bi-layered coplanar waveguide with partial capacitances.

where the $C_0^{\pm}$ refer to the capacitances of electrodes in the absence of dielectric which can be obtained by conformal mapping, [69]. The $C_g^{\pm}$ represent the capacitances due to the gap regions between conductors, which as done in the previous section, are simply approximated as parallel plate capacitances $C_g^{\pm} = \varepsilon_0 \frac{t}{s^{\pm}}$.

The total substrate capacitance, C_S, depends on both the lower and upper substrate layer capacitances, C_{S1} and C_{S2}, and each one is in turn obtained by the parallel combination of the partial substrate capacitances of the homogeneous subregions at $y < 0$ and $y > 0$, $C_{S1}^{\pm}$ and $C_{S2}^{\pm}$ as

$$C_{Si} = C_{Si}^{-} + C_{Si}^{+}, \tag{3.39}$$

with $i = 1, 2$.

To calculate C_S, according to [84], for a two layered CPW, the relation between upper and lower substrate material permittivities is determinant to select either a serial or else a parallel association between the two substrate capacitances. The fundamental difference between those two cases is that the former is characterized by an upper layer of smaller relative permittivity and in the later the smaller permittivity layer corresponds to the lower layer. These cases should be treated in a different way. If the upper layer permittivity is bigger ($\varepsilon_{r2} > \varepsilon_{r1}$), a parallel association is more adequate, while in the opposite case ($\varepsilon_{r2} < \varepsilon_{r1}$), a serial association should be used. [84] That is

$$C_S = C_{S1} + C_{S2}; \quad \varepsilon_{r2} > \varepsilon_{r1}, \tag{3.40a}$$

$$(C_s)^{-1} = (C_{S1})^{-1} + (C_{S2})^{-1}; \quad \varepsilon_{r2} < \varepsilon_{r1}. \tag{3.40b}$$

The use of conformal mapping techniques allows to derive expressions for $C_0^{\pm}$, $C_{S1}^{\pm}$ and $C_{S2}^{\pm}$ which involve elliptic integrals [77]. By letting

$$A_i^{\pm} = \frac{K(k_i^{\pm})}{K((k_i^{\pm})')}, \tag{3.41}$$

with $i = 0, 1, 2s, 2p$ where "0", "1", "2s" and "2p" are labels which refer to the free-space, lower substrate layer, upper substrate layer for the serial case and upper substrate layer for the parallel case, respectively, and being $K(k)$ the complete elliptic integral of the first kind, we have

$$C_0^{\pm} = \varepsilon_0 A_0^{\pm}, \tag{3.42}$$

with

$$k_0^{\pm} = \frac{w}{w + 2s^{\pm}} \sqrt{\frac{w_g(w + 2s^{\pm} + w_g^{\pm})}{w_g^{\pm}(w + 2s^{\pm} + w_g^{\pm}) + s^{\pm}(s^{\pm} + w)}}, \tag{3.43}$$

for the vacuum capacitance, and

$$C_{S1}^{\pm} = \varepsilon_0(\varepsilon_{r1} - 1)A_1^{\pm}, \tag{3.44}$$

with

$$\begin{aligned} k_1^{\pm} \quad = \quad & \frac{\sinh(\pi w/4h_1)}{\sinh(\frac{\pi(w+2s^{\pm})}{4h_1})} \times \\ & \sqrt{\frac{\sinh^2[\frac{\pi(\frac{w}{2}+s^{\pm}+w_g^{\pm})}{2h_1}] - \sinh^2, [\frac{\pi(\frac{w}{2}+s^{\pm})}{2h_1}]}{\sinh^2[\frac{\pi(\frac{w}{2}+s^{\pm}+w_g^{\pm})}{2h_1}] - \sinh^2(\pi\frac{w}{4h_1})}}, \end{aligned} \tag{3.45}$$

for the lower layer capacitance. The term $(k_i^{\pm})'$ is obtained as

$$(k_i^{\pm})' = \sqrt{1 - (k_i^{\pm})^2}, \tag{3.46}$$

where $i = 0, 1, 2s, 2p$.

As for the upper layer substrate capacitance, C_{S2}, following [84], a different analysis is required depending on whether the upper layer material permittivity is either bigger or lower than the lower layer material permittivity. The next subsections show this analysis.

Total substrate capacitance when $\varepsilon_{r2} > \varepsilon_{r1}$ (thin film)

The partial upper layer capacitances $C_{S2}^{\pm}$ are found in this case by applying conformal mapping techniques and using an equivalent relative dielectric permittivity $(\varepsilon_{r2} - \varepsilon_{r1})$ [77] as follows

$$C_{S2}^{\pm} = \varepsilon_0(\varepsilon_{r2} - \varepsilon_{r1})A_{2p}^{\pm}, \tag{3.47}$$

with A_{2p} as given in (3.41). The terms $k_{2p}^{\pm}$ for this case are obtained as [77]

$$k_{2p}^{\pm} = \frac{\sinh(\pi w/4h_2)}{\sinh(\frac{\pi(w+2s^{\pm})}{4h_2})} \times \sqrt{\frac{\sinh^2[\frac{\pi(\frac{w}{2}+s^{\pm}+w_g^{\pm})}{2h_2}] - \sinh^2[\frac{\pi(\frac{w}{2}+s^{\pm})}{2h_2}]}{\sinh^2[\frac{\pi(\frac{w}{2}+s^{\pm}+w_g^{\pm})}{2h_2}] - \sinh^2(\pi\frac{w}{4h_2})}}. \tag{3.48}$$

The total substrate capacitance for this case is the parallel combination of C_{S1} and C_{S2}. Substituting in equation (3.40a), we get

$$C_{SP} = \varepsilon_0(\varepsilon_{r1} - 1)(A_1^- + A_1^+) + \varepsilon_0(\varepsilon_{r2} - \varepsilon_{r1})(A_{2p}^- + A_{2p}^+). \tag{3.49}$$

Total substrate capacitance when $\varepsilon_{r1} > \varepsilon_{r2}$ (buffer layer)

In this case, the assumption of serial capacitances is more accurate than the parallel assumption [84]. The contribution of the upper layer capacitance is evaluated as the capacitance of a CPW backed by an electric wall [87]. The partial upper layer capacitances are

$$C_{S2}^{\pm} = \varepsilon_0(\varepsilon_{r2} - 1)A_{2s}^{\pm}. \tag{3.50}$$

The terms $k_{2s}^{\pm}$ for this case are more appropriately expressed as [87]

$$k_{2s}^{\pm} = \frac{\tanh(\pi w/4h_2)}{\tanh(\pi(w + 2s^{\pm})/4h_2)}. \tag{3.51}$$

The total substrate capacitance is in this case the serial combination of C_{S1} and C_{S2}. Substituting in expression (3.40b), we obtain

$$C_{SS} = \frac{\varepsilon_0(\varepsilon_{r1} - 1)(\varepsilon_{r2} - 1)(A_1^- + A_1^+)(A_{2s}^- + A_{2s}^+)}{(\varepsilon_{r1} - 1)(A_1^- + A_1^+) + (\varepsilon_{r2} - 1)(A_{2s}^- + A_{2s}^+)}. \tag{3.52}$$

3.4.2 External and internal inductances

Once the partial capacitances have been obtained, the next step is to find the external and the internal inductances. From the value of C_0 of equation (3.38), the external inductance is found as

$$L_{ext} = \frac{1}{c^2 C_0}. \tag{3.53}$$

The expression for internal inductance can be derived by applying the Wheeler formula [83]. Taking into account the asymmetry of the CPW line,

$$L_{int} = \frac{\delta}{2}\left[\frac{\partial L_{ext}}{\partial s^-} + \frac{\partial L_{ext}}{\partial s^+} - \frac{\partial L_{ext}}{\partial w} - \frac{\partial L_{ext}}{\partial t}\right]. \tag{3.54}$$

To solve the derivatives we use the approximations for the term $A_0^{\pm}$, included in L_{ext} through C_0, given in [77]

$$A_0^{\pm} = \begin{cases} \frac{\pi}{2\ln(\frac{4}{k_0^{\pm}})}; & \text{for } 0 < k_0^{\pm} < 10^{-5} \\ \frac{\pi}{\ln(4\frac{1+(k_0^{\pm})'}{1-(k_0^{\pm})'})}; & \text{for } 10^{-5} \leq k_0^{\pm} < \frac{1}{\sqrt{2}} \\ \frac{1}{4}\ln(4\frac{1+k_0^{\pm}}{1-k_0^{\pm}}); & \text{for } k_0^{\pm} \geq \frac{1}{\sqrt{2}} \end{cases} \tag{3.55}$$

arriving to

$$L_{int} = \frac{\delta}{\varepsilon_0 c^2\left[2(A_0^- + A_0^+) + \frac{t}{s^-} + \frac{t}{s^+}\right]^2} F, \tag{3.56}$$

where

$$F = F^- + F^+, \tag{3.57}$$

and

$$F^{\pm} = T^{\pm}\left[\frac{2(s^{\pm}+w)}{w(w+2s^{\pm})} + \frac{1}{2(s^{\pm}+w_g^{\pm})} - \frac{1}{2(w+2s^{\pm}+w_g^{\pm})}\right] + \frac{1}{s^{\pm}}\left(\frac{t}{s^{\pm}}+1\right).$$

The term $T^{\pm}$ is given by

$$T^{\pm} = \begin{cases} \frac{4(A_0^{\pm})^2}{\pi}; & \text{for } 0 < k_0^{\pm} < 10^{-5} \\ \frac{4(A_0^{\pm})^2}{\pi(k_0^{\pm})'}; & \text{for } 10^{-5} \leq k_0^{\pm} < \frac{1}{\sqrt{2}} \\ \frac{4}{\pi((k_0^{\pm})')^2}; & \text{for } k_0^{\pm} \geq \frac{1}{\sqrt{2}} \end{cases} \tag{3.58}$$

3.4.3 Extended PP formulation

Substituting the expressions of C_0 (3.38), C_{SS} (3.52) for the serial case, or C_{SP} (3.49) for the parallel case, L_{ext} (3.53) and L_{int} (3.56) into the quasi-TEM formulation we arrive to the simplified compact quasi-TEM PP closed-form expressions given by equations (3.59), (3.60) and (3.61). These simple expressions include finite electrode thickness, finite substrate height, finite and asymmetric ground planes and asymmetric gap widths, as well as two layered CPW structures.

$$\varepsilon_{eff} = \left[1 + \frac{(\varepsilon_{r1} - 1)(A_1^- + A_1^+)}{2A_0^- + 2A_0^+ + \frac{t}{s^-} + \frac{t}{s^+}} B\right] \left[1 + \frac{\delta}{2A_0^- + 2A_0^+ + \frac{t}{s^-} + \frac{t}{s^+}} F\right], \tag{3.59}$$

$$Z_0 = \frac{\sqrt{1 + \frac{\delta}{2A_0^- + 2A_0^+ + \frac{t}{s^-} + \frac{t}{s^+}} F}}{c\varepsilon_0 \sqrt{\left(2A_0^- + 2A_0^+ + \frac{t}{s^-} + \frac{t}{s^+}\right)\left[2A_0^- + 2A_0^+ + \frac{t}{s^-} + \frac{t}{s^+} + (\varepsilon_{r1} - 1)(A_1^- + A_1^+)B\right]}}, \tag{3.60}$$

$$\alpha = \frac{\pi f \delta}{\varepsilon_0 c^2 Z_0 \left[2A_0^- + 2A_0^+ + \frac{t}{s^-} + \frac{t}{s^+}\right]^2} F + \frac{\omega}{2} \varepsilon_0 (\varepsilon_{r1} - 1)(A_1^- + A_1^+) Z_0 B \tan\delta. \tag{3.61}$$

The term B depends on the relation between upper and lower layer permittivities, and takes values of

$$B = \begin{cases} 1; & \text{no intermediate layer} \\ 1 + \frac{(\varepsilon_{r2} - \varepsilon_{r1})(A_{2p}^- + A_{2p}^+)}{(\varepsilon_{r1} - 1)(A_1^- + A_1^+)}; & \text{for } \varepsilon_{r2} > \varepsilon_{r1} \\ \frac{(\varepsilon_{r2} - 1)(A_{2s}^- + A_{2s}^+)}{(\varepsilon_{r1} - 1)(A_1^- + A_1^+) + (\varepsilon_{r2} - 1)(A_{2s}^- + A_{2s}^+)}; & \text{for } \varepsilon_{r1} > \varepsilon_{r2} \end{cases} \tag{3.62}$$

Extension to frequencies over the quasi-TEM range will be accounted by the dispersion formulas presented in section (3.2.5).

These formulas are well suited to computer-aided design and optimization of CPW due to their simplicity and flexibility to easily include changes in the CPW cross-section. Next section will deal with the PP model benchmarking against HFSS simulations and CPW designs extracted from literature.

3.5 Benchmarking

This section presents a summary of the more relevant results on the extensive accuracy tests performed over the PP formulas.

As a first test, we found the discrepancy margin against HFSS results for the reference CPW of table 2.2, see Fig. (3.9). As seen the $DM(PP)$ values are in close resemblance to the $DM(Heinrich)$ of Fig. (3.4). For more extensive comparisons of the PP model against Heinrich approach see [85].

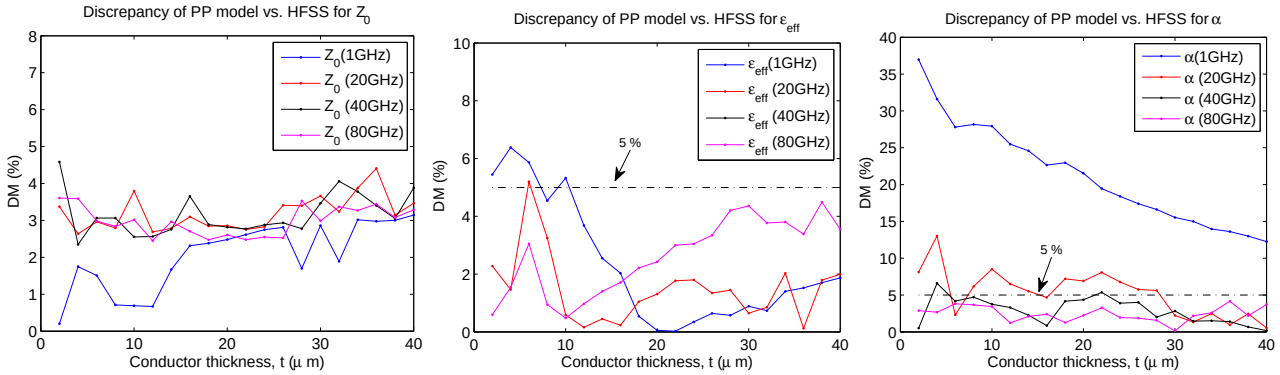

Figure 3.9: Discrepancy margin between PP model and HFSS for (a) Z_0, (b) ε_{eff} and (c) α versus t for the reference CPW of table 2.2 with $h_2 = 0$.

In order to check the accuracy and efficiency of the PP model, extended to the cases of asymmetry and bi-layer cross-section, several simulations were done. Benchmarking against HFSS simulation results first, and later against measures over CPW designs reported in literature, has been made for the cases of a SiO_2 buffer layer CPW in subsections 3.5.1 and 3.5.2, a $LiNbO_3$ thin film in subsections 3.5.3 and 3.5.4, and an asymmetry design in subsection 3.5.5.

We chose to provide here the absolute value of the propagation parameter under test instead of just the DM because the goal of this section is two-fold, besides testing the accuracy of the PP model, we also analyze how to improve the propagation parameters simulated and how a propagation parameter optimization may affect the others. A maximum DM bound is provided in each plot for accuracy assessment.

3.5.1 SiO_2 buffered CPW

A strategy commonly used for MZM optimization is the use of a buffer layer, usually SiO_2 due to its low permittivity, $\varepsilon_r = 4$. Simulations of Z_0, ε_{eff} and α over the reference CPW of table 2.2 with a SiO_2 buffer layer are performed in this subsection.

Fig. (3.10) shows the variation of the propagation parameters for a frequency range of $5 - 100$ GHz. Results of Z_0, ε_{eff} and α are in accordance with the results of HFSS, with maximum discrepancy values of 1.15%, 1.25% and 13%, respectively, over the whole 100 GHz range.

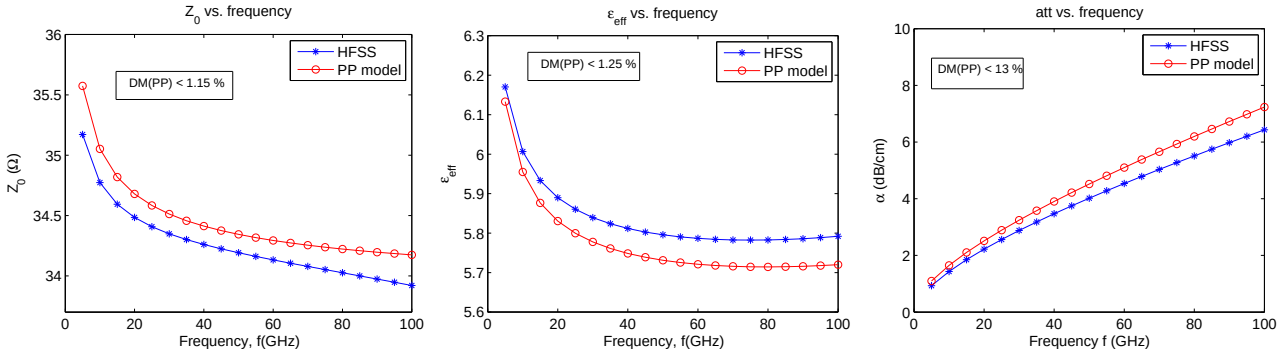

(a) (b) (c)

Figure 3.10: (a) Z_0, (b) ε_{eff} and (c) α versus f for the reference CPW of table 2.2 with $h_2 = 1.5\mu m$.

Fig. (3.11) displays the dependence of the propagation parameters over t. Excellent agreement between the PP model and the HFSS is found, with $DM(PP)$ bounds of 2.34%, 4.5% and 11% for the Z_0, ε_{eff} and α, respectively.

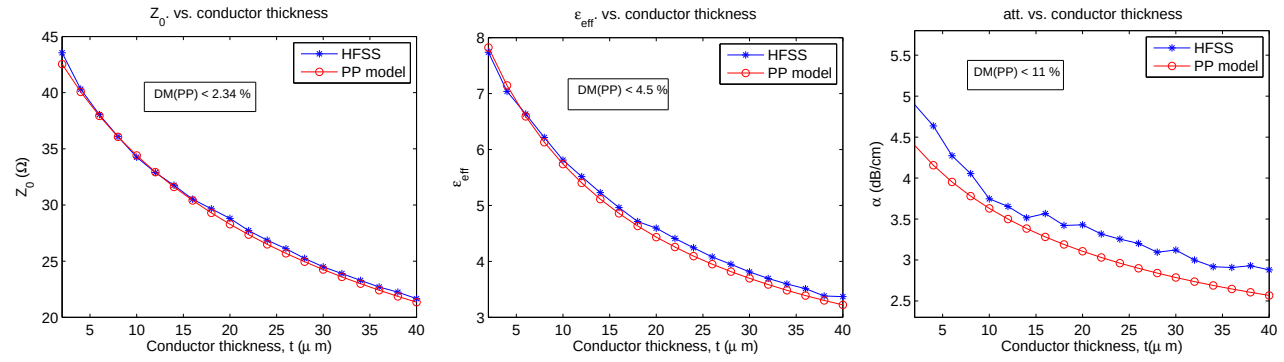

(a) (b) (c)

Figure 3.11: (a)Z_0, (b) ε_{eff} and (c) α versus t for the reference CPW of table 2.2 with $h_2 = 1.5\mu m$. The frequency used was 40GHz.

As it was pointed out in the previous Chapter, the increase of t brings a decrease in all the RF

propagation parameters, which is good for achieving low α and velocity matching but really bad for impedance matching. For the reference CPW configuration, if a thickness of $t > 22\mu m$ is selected, then $n_m = \sqrt{\varepsilon_{eff}}$ drops below $n_{opt} = 2.15$, mismatching the wave velocities. In this case the thickness for velocity matching would be around $20\mu m$, but for this value $Z_0 \sim 30\Omega$, is far away of the impedance matching condition.

Fig. (3.12) presents the evolution of the parameters for different values of h_2 for the reference CPW of table 2.2. Good agreement was found between our model and HFSS with maximum $DM(PP)$ of 1.9%, 3.5% and 9.6% for Z_0, ε_{eff} and α, respectively.

As observed, the increase in h_2 induces a rise in Z_0 and a drop in ε_{eff} and α. For $h_2 \sim 2.5\mu m$ the condition of velocity matching is reached, with a $Z_0 \sim 38\Omega$, a better value than the previous case, but still too low. Also in the downside is a reduction of Γ which impacts the V_π, as seen in section 2.3.

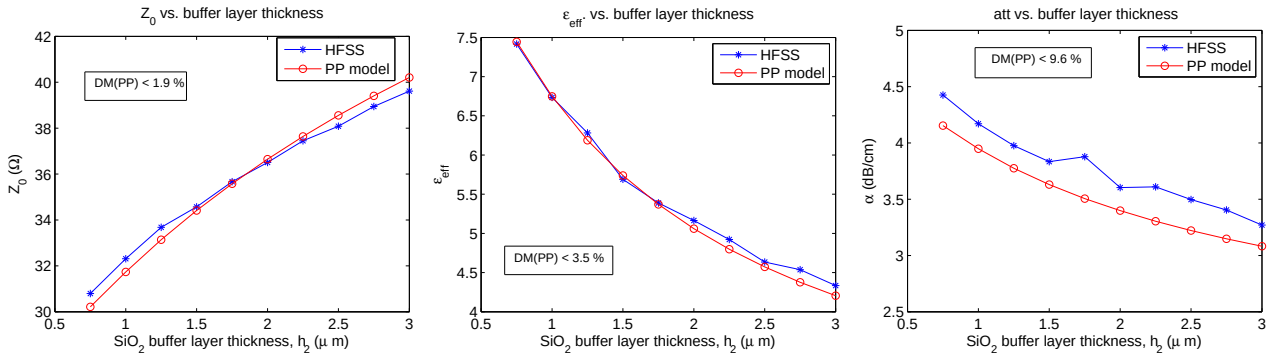

(a) (b) (c)

Figure 3.12: (a) Z_0, (b) ε_{eff}, and (c) α versus h_2 for the reference CPW of table 2.2. The frequency used was 40 GHz.

3.5.2 SiO_2 buffered CPW from [1]

The CPW design simulated using a spectral-domain approach for a SiO_2 buffer layer CPW in [1] is the subject of the PP formulas accuracy tests presented in this section.

The CPW physical parameters are shown in table (3.1). The attenuation values reported in [1] consider the field attenuation coefficient α_0 instead of α. These two quantities are related through $\alpha = \alpha_0\sqrt{f}$ at frequencies where the conductor attenuation is dominant as in this case. Only the losses due to the conductor were analyzed in [1], therefore we dropped the dielectric losses in our model for better comparison.

Simulations of the propagation parameters against h_2 show excellent $DM(PP)$, with values below 4% for n_m, 8% for α_0 and 2.8% for Z_0, as displayed in Fig. (3.13). In this case we decided to plot

Parameter	Value
w (μm)	8
s (μm)	15
t (μm)	10
w_g (μm)	100
h_1 (μm)	50
h_2 (μm)	1.5

Table 3.1: Parameters of the CPW of [1].

$n_m = \sqrt{\varepsilon_{eff}}$ instead of ε_{eff} for comparison with results provided in [1]. Also a good agreement is observed against computed results of Figs. 2 and 3 in [1], where it is possible to see that near velocity and impedance matching are reached for $h_2 = 1.5\mu m$ ($n_{opt} = 2.2$). Our results are consistent with that yielding values of $n_m = 2.21$ and $Z_0 = 53\Omega$ for this particular CPW configuration.

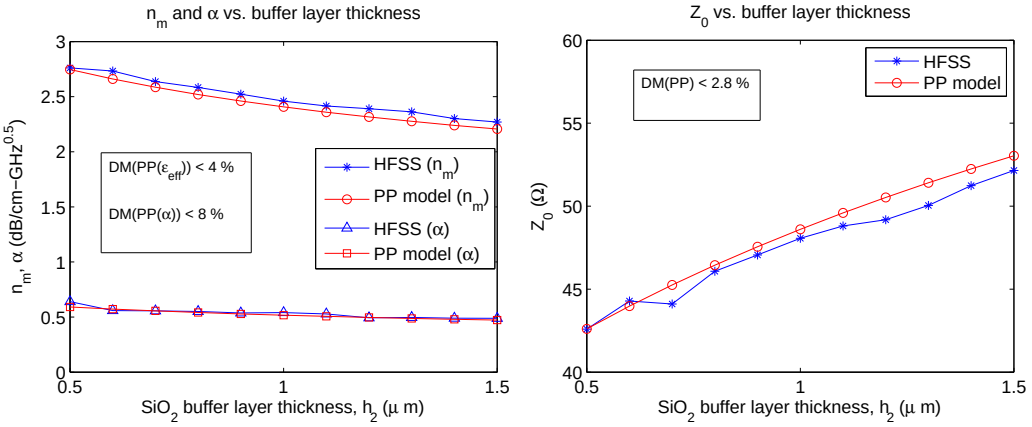

(a) (b)

Figure 3.13: (a) ε_{eff} and α_0, and (b) Z_0 for the buffered CPW of [1] (table 3.1). The frequency used was $10GHz$.

3.5.3 $LiNbO_3$ thin film

In this subsection several simulations are presented for the reference CPW of table 2.2, with a thin film of $h_2 = 5\mu m$. In each case, the parameter under test will vary while the others will remain constant.

The evolution of the propagation parameters with f is shown in Fig.(3.14), with maximum $DM(PP)$ of 6%, 2.1% and 12% for Z_0, ε_{eff} and α, respectively.

Fig. (3.15) displays the propagation parameter values against t. The maximum DM(PP) are 7%, 4.5% and 3.6% for Z_0, ε_{eff} and α, respectively. For this configuration the velocity matching is reached for $t \sim 25\mu m$, but for this value the impedance is around 33Ω, far away of the impedance matching

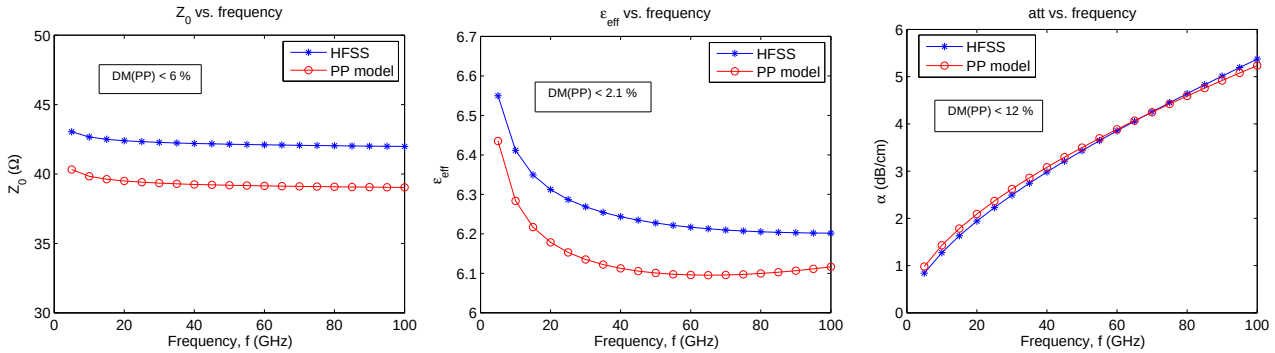

(a) (b) (c)

Figure 3.14: (a) Z_0, (b) ε_{eff}, and (c) α versus f for the reference CPW of table 2.2 with a $LiNbO_3$ thin film of $h_2 = 5\mu m$.

condition.

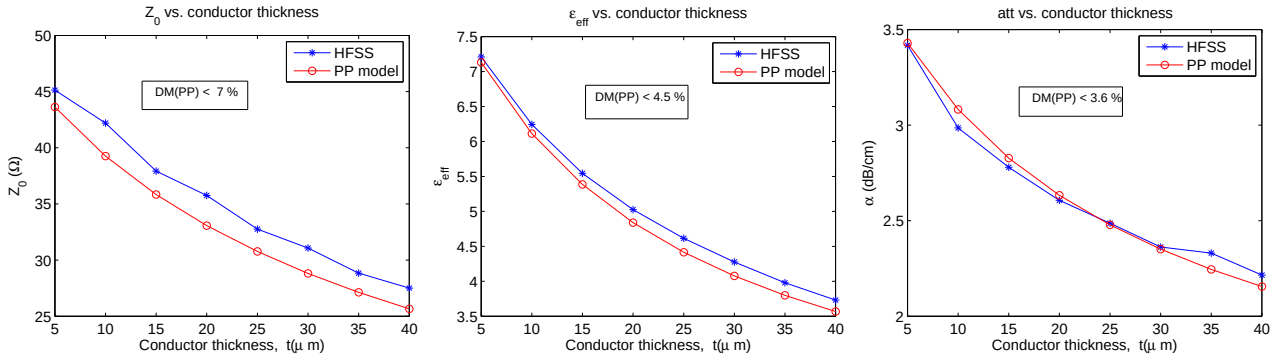

(a) (b) (c)

Figure 3.15: (a) Z_0, (b) ε_{eff} and (c) α versus t for the reference CPW of table 2.2 with a $LiNbO_3$ thin film of $h_2 = 5\mu m$. The frequency used was $40GHz$.

The behavior of the propagation parameters versus the variation of the $LiNbO_3$ thin film thickness, h_2, is represented in Fig. (3.16). Maximum $DM(PP)$ are 5.5%, 2.7% and 5.1% for Z_0, ε_{eff} and α, respectively.

Observing the graphics when making the $LiNbO_3$ film thinner the impedance rises, and ε_{eff} and α decrease. For $h_2 \sim 3\mu m$ the velocity matching is achieved with $Z_0 \sim 45\Omega$, which is better than the previous results, and α is about $2.7dB/cm$. This thin film thickness is already in the range of typical optical waveguide dimensions and it may be technologically challenging for a practical MZM prototype [39].

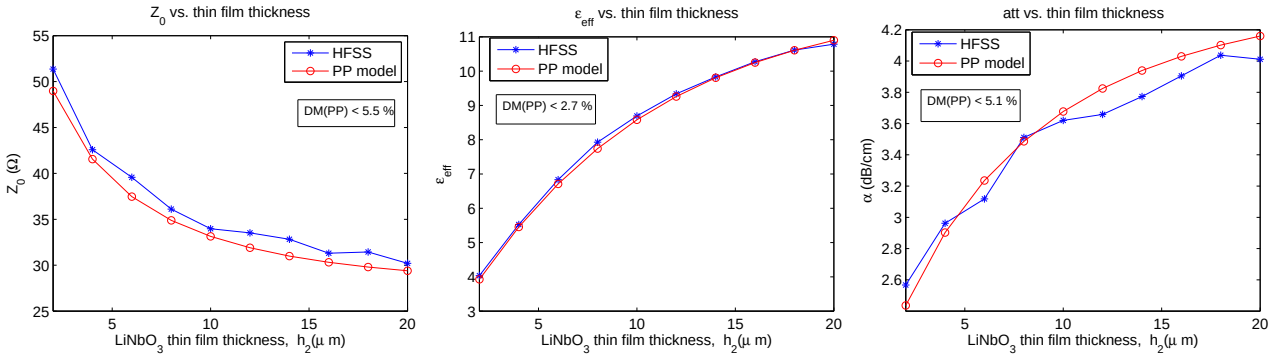

(a) (b) (c)

Figure 3.16: (a) Z_0, (b) ε_{eff}, and (c) α versus $LiNbO_3$ thin film thickness for the reference CPW of table 2.2. The frequency used was $40GHz$.

3.5.4 $LiNbO_3$ thin film MZM from [2]

Benchmarking of the PP model against the MZM propagation parameter outcomes of the $LiNbO_3$ thin film design of Gheorma et.al. [2], and also against HFSS will be presented here. The CPW physical parameters are shown in table 3.2.

Parameter	Value
w (μm)	8
s (μm)	25
t (μm)	16
w_g (μm)	100
h_1 (μm)	50
h_2 (μm)	5

Table 3.2: Parameters of the CPW of [2].

In Fig. (3.17) n_m, α and Z_0 against f are plotted. Results of $DM(PP)$ are excellent keeping within bounds of 0.6%, 14% and 0.8% for n_m, α and Z_0, respectively in the whole frequency range.

The values of the propagation parameters are in accordance to results obtained in the f range up to $40GHz$ of Fig. 4 in [2].

Fig. (3.18) shows the evolution of n_m, α_0 and Z_0 with the $LiNbO_3$ film thickness for a frequency of $10GHz$, and $w = 10\mu m$ for the reference configuration of table 3.2. In this case, in order to compare this value with Fig. 2 of [2], we calculated α_0 instead of α ($\alpha = \alpha_0\sqrt{f}$). Again, a good correspondence is encountered. As the thin film is reduced below $20\mu m$, the phase matching condition ($n_m = 2.15$) is approached, while Z_0 increases. A good trade-off between velocity and impedance matching is found around $h_2 = 5\mu m$, where $n_m = 2.3$ and $Z_0 = 52.8\Omega$. A better wave velocity matching is found for

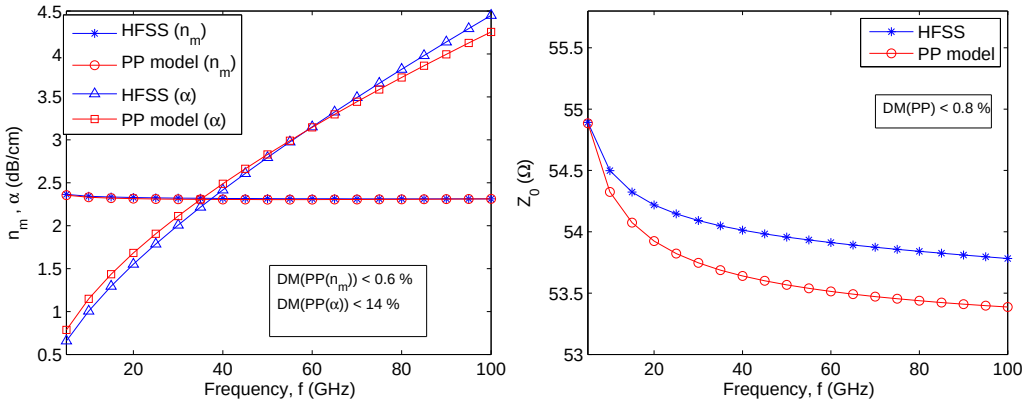

(a) (b)

Figure 3.17: (a) n_m, α, and (b) Z_0 for the $LiNbO_3$ thin film CPW design of [2] (table 3.2).

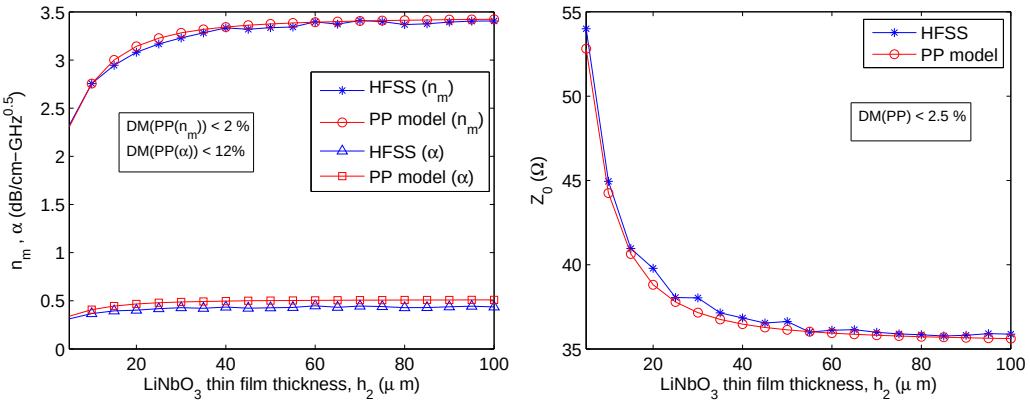

(a) (b)

Figure 3.18: (a) n_m, α_0 and (b) Z_0 vs. the $LiNbO_3$ thin film thicknesses for the MZM design of [2] (table 3.2) with $w = 10\mu m$. The frequency used was $10GHz$.

$h_2 = 4\mu m$, but Z_0 increases to 56Ω, which it is further away from the impedance matching condition.

The $DM(PP)$ shows excellent results below 2.5%, 2% and 12% for Z_0, n_n and α_0, respectively.

3.5.5 Asymmetric CPW

In order to test the PP model ability to include the CPW asymmetry, in this section the asymmetric CPW design of [35], specially tailored for a small-signal chirp parameter value of 0.65, was used along HFSS simulations for the PP model benchmarking. The physical cross-section parameters of the MZM are displayed in table 3.3.

Fig. (3.19) shows the evolution of ε_{eff}, Z_0 and α versus an asymmetric gap s^+ for a $f = 10$ GHz.

Parameter	Value
w (μm)	30
s^+ (μm)	90
s^- (μm)	20
t (μ m)	25
w_g (μ m)	100
h_1 (μ m)	50
h_2 (μ m)	8.5

Table 3.3: Parameters of the CPW of [35].

Even though ε_{eff} and α barely change with the increment of s^+, Z_0 does experience a significant increment. The $DM(PP)$ shows a good performance with values of 4.4%, 5.2% and 7% for the values of Z_0, n_m and α respectively.

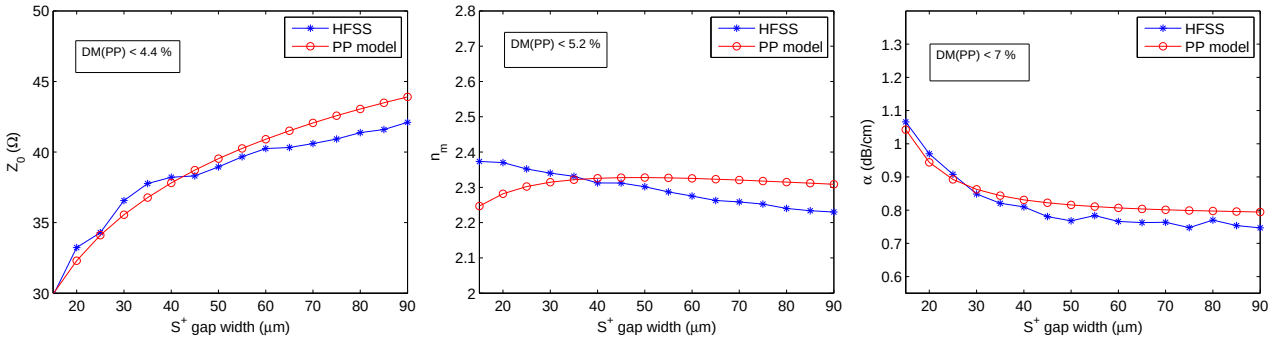

(a) (b) (c)

Figure 3.19: (a) Z_0, (b) n_m and (c) α_0 vs. s^+ gap width for the reference $LiNbO_3$ thin film MZM of table 3.3. The frequency used was $10GHz$.

The authors of [35] obtained measures of $n_m = 2.27$ and $Z_0 = 46\Omega$, for a frequency range of $45 - 50GHz$. Results from the PP closed-form expressions are $n_m = 2.2396 - 2.2405$, $Z_0 = 44.435 - 44.410\Omega$ and $\alpha_0 = 0.2765 - 0.2795 dB/cm\sqrt{GHz}$, for this range, in close proximity with the design, and with maximum $DM(PP)$ of 0.1%, 4% and 4% for n_m, α_0 and Z_0, respectively.

3.6 Summary of the Chapter

This Chapter has focused on finding CPW closed-form expressions for the propagation parameters of CPW suited to systematic MZM design. HFSS simulations have been used to test the accuracy of closed-form approaches found in literature for CPW configurations relevant to MZM. The conclusion is that only the Heinrich formulation provides accuracies within tolerable ranges. However these formulas

are cumbersome and not easily extended to consider variations in the line geometry such as a bi-layered substrates and gap asymmetry.

A simple and accurate closed-form approach for the propagation parameters of coplanar transmission waveguide, namely the parallel-plate (PP) approximation, was developed, including thick conductor, skin effect loss, asymmetric gaps and ground electrodes, as well as bi-layered substrates. Its accuracy was confirmed through benchmarking with finite difference full-wave HFSS simulations and with published results for MZMs with SiO_2 buffer layer, $LiNbO_3$ thin film and asymmetric gap widths. As the base of this new model is the CM, the formulation is flexible to variations in the CPW cross-section.

Due to its compact and simple formulation, the versatility to include new geometries, and the low discrepancy values found with respect to HFSS and also with respect to experimental designs, the PP closed-form expressions have great potential as a tool for the analysis and design of CPW structures in a wide variety of applications, specially MZM, and allow to tailor the cross-section geometry in order to get the desired propagation parameters.

In the next Chapter we close the loop in the MZM design and optimization process by analyzing which are the required CPW propagation parameters values that allow to meet a specific performance in terms of system features such as B, V_π and L.

4

Bandwidth-Length Expressions for Mach Zehnder Modulators

4.1 Introduction

The performance of MZM is mainly measured by the maximum modulation bandwidth B and the minimum driving power, usually given in terms of the required voltage for a π phase shift over a MZM branch, V_π. Since the Pockels electro-optical induced phase shift accumulates with the propagated distance L, V_π can always be reduced by increasing L. However, in presence of an optical-electrical mismatch and skin effect electrode loss, that comes at the expense of a reduction in B, and then, for any given MZM cross-sectional geometry, a trade-off between B and L (and hence V_π) exists.

An analysis neglecting the effect of loss shows that, for a given cross-section MZM design, BL is kept constant and therefore, the BL product has been used as a figure of merit by many authors [70] [54] [51] [88].

Nevertheless, when the effect of velocity mismatch is dropped from the model, a constant BL^2 relation is found, and therefore for configurations that are near velocity matching, a BL^2 figure of merit is more convenient. The analysis in [55] further showed that the range of validity of the figure of merit depends not only on the cross-sectional parameters (α, ν), but also on the targeted B and L values.

In this Chapter we look into the $B-L$ trade-off problem. In a first section the limiting $\alpha_0 \to 0$ and $\nu \to 0$ cases have been revisited and the optical and electrical B concepts have been clarified.

In a second section the constant B curves have been obtained by numerical procedures and then used as base for a curve-fitting which has allowed to cast the $B-L$ relation in closed-form for a general

case, valid for every α and ν value.

From the $B-L$ closed-form expressions a complete model of the $B-L$ trade-off in MZM has been derived and it is presented. Measures reported in literature over fabricated MZM designs have allowed to confirm the validity of the new $B-L$ trade-off model. In section 4.3, the most relevant results are presented.

In section 4.4, novel B and L charts obtained from the trade-off model are shown to provide a useful graphical approach to find the cross-section parameters allowing to meet a target performance in terms of B and L.

4.2 Figures of merit and trade-offs in MZM

We start the analysis from the frequency response expression of an impedance matched MZM in the presence of electrical losses and optical-electrical velocity mismatch [23]

$$M(f) = e^{\frac{-\alpha_0\sqrt{f}L}{2}}\left[\frac{\sinh^2\left(\frac{\alpha_0\sqrt{f}L}{2}\right)+\sin^2\left(\pi f\nu L\right)}{\left(\frac{\alpha_0\sqrt{f}L}{2}\right)^2+\left(\pi f\nu L\right)^2}\right]^{1/2}. \tag{4.1}$$

The electrical and optical bandwidths verify, respectively

$$M(B^e) = 1/\sqrt{2}, M(B^o) = 1/2. \tag{4.2}$$

In a general case the solutions to (4.2) need to be found numerically. Only in the limiting cases, when $\alpha_0 = 0$ and $\nu = 0$, have these solutions been obtained analytically. From (4.1), assuming $\alpha_0 = 0$ we get [54]

$$M(f)_{\alpha=0} = \frac{\sin \pi f\nu L}{\pi f\nu L} = sinc(\pi f\nu L). \tag{4.3}$$

The 3dB electrical and optical B in the limit of low-loss (LL) can be calculated by equating the expression (4.3) to $1/\sqrt{2}$ and $1/2$, respectively. Both members of equation are plotted to find the value of $u = f\nu L$, Fig. 4.1

The values of u are 0.4429 and 0.6033 for the electrical and the optical $3dB$ frequency response, respectively.

Therefore, we get,

$$B^{(e,o)}_{\alpha_0=0} = \frac{k^{(e,o)}_\nu}{\nu L}, \tag{4.4}$$

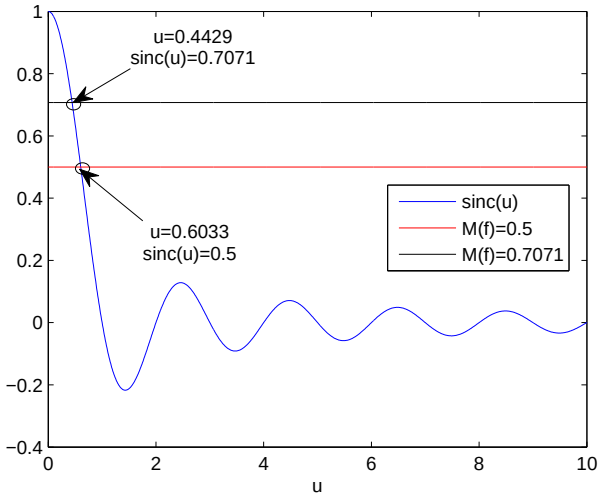

Figure 4.1: Sinc function and intersections with the optical and electrical $3dB$ response.

with $k_\nu^e = 0.4429$ for the electrical and $k_\nu^o = 0.6033$ for the optical 3 dB bandwidth, respectively.

To find the expression for a velocity matched MZM, from (4.1), and making $\nu = 0$, in the velocity matching limit (VM), we get [54]

$$M(f)_{\nu=0} = \frac{1 - e^{-\alpha_0\sqrt{f}L}}{\alpha_0\sqrt{f}L}. \tag{4.5}$$

In Fig. (4.2), a plot of the equation $(1-e^{-x})/x$, where in this case $x = \alpha_0\sqrt{f}L$, and its intersection with $1/2$ and $1/\sqrt{2}$ are shown. We obtain $x = 0.7384$ and $x = 1.5936$ for the electrical and optical 3 dB response, respectively. Substituting in (4.5) for the electrical and optical $3dB$ response, it is found

$$B_{\nu=0}^{(e,o)} = \frac{k_\alpha^{(e,o)}}{(\alpha_0 L)^2}, \tag{4.6}$$

with $k_\alpha^e = 0.5452$ and $k_\alpha^o = 2.5396$.

Apart from these limits in which an analytical form for the $B - L$ relation exists, for intermediate range values, this relation needs to be found in every specific case as a numerical solution to (4.2). Derivation of a closed-form expression that could analytically link B and L for every value of α_0 and ν is found of great interest, and it is the subject of the next section.

4.3 Bandwidth-length formulas for MZM

In Fig. (4.3), we plotted the constant $B - L$ curves for different combinations of α and ν. The curves seem to follow a parabolic pattern, and therefore a fitting using a second-order polynomial is proposed.

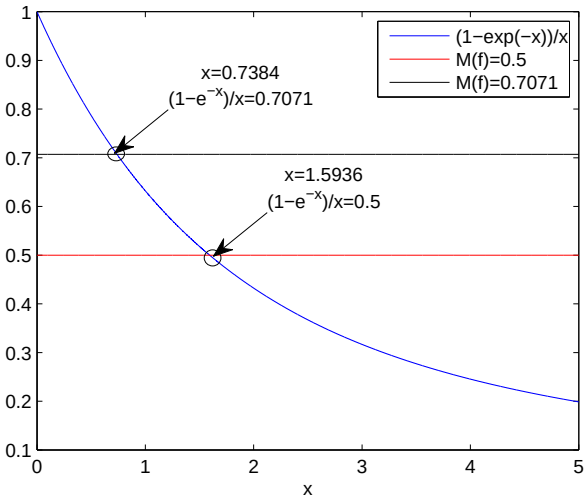

Figure 4.2: Function of (4.6) and intersections with the optical and electrical $3dB$ response.

An equation of the form ay^2+by+c from the two intersection points and a third one on the imaginary intersection in the negative ν axis is found (Appendix F) and it is given by (4.7).

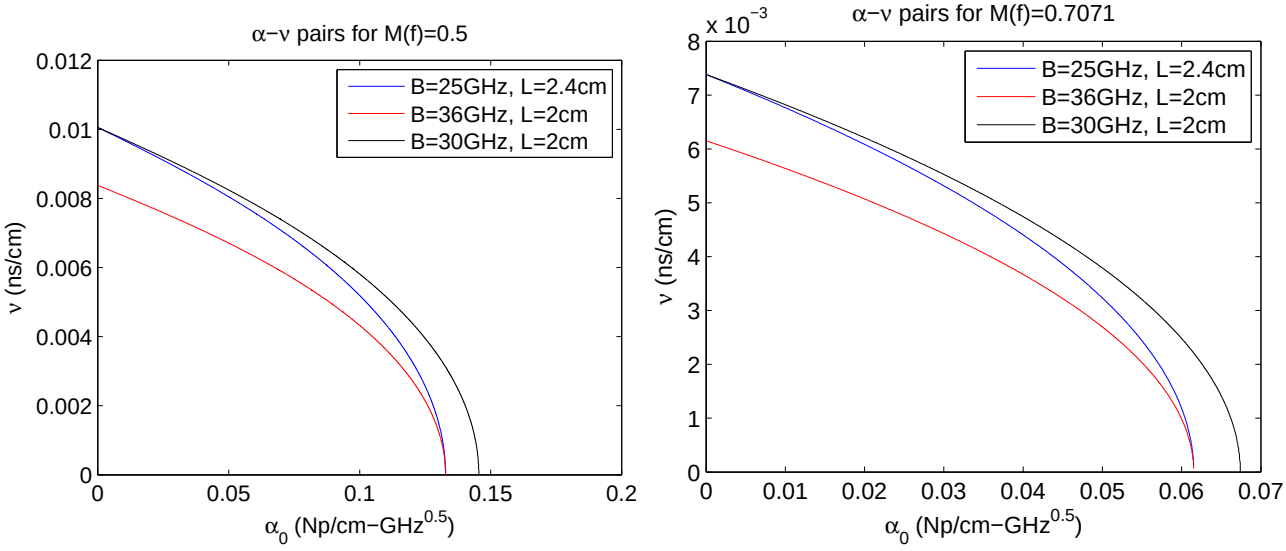

(a) (b)

Figure 4.3: The $\alpha_0-\nu$ plane for (a) $M(f)=0.5$ and (b) $M(f)=0.7071$.

From now on, the super-indices indicating electrical or optical B will be dropped, as the results are interchangeable by only using in the expressions the corresponding values of k_ν and k_α given in section (4.2).

$$B^2L^2 + \frac{k_\nu^2}{\sqrt{k_\alpha}}\frac{\alpha_0}{\nu^2}\sqrt{B}L = \frac{k_\nu^2}{\nu^2}. \tag{4.7}$$

From the cross section parameters, reference B and L values for the modulator may be defined as,

$$B_M = \frac{k_\nu^2}{k_\alpha}\frac{\alpha_0^2}{\nu^2}, \tag{4.8}$$

$$L_M = \frac{1}{2}\frac{k_\alpha}{k_\nu}\frac{\nu}{\alpha_0^2}. \tag{4.9}$$

Using the definitions above, the analytic solution to (4.7) can be given in compact form in terms of normalized quantities (Appendix F) as

$$B_N = \frac{B}{B_M} = (2L_N)^{-2/3}T[1 - \sqrt{T^{-3/2} - 1}]^2, \tag{4.10}$$

$$L_N = \frac{L}{L_M} = B_N^{-3/2}[\sqrt{4B_N + 1} - 1], \tag{4.11}$$

where

$$T = \frac{1}{2}W^{-1/3}(S^{1/3} - S^{-1/3}), \tag{4.12}$$

$$S = W + \sqrt{1 + W^2}, \tag{4.13}$$

$$W = \frac{3^{3/2}}{2^5}L_N. \tag{4.14}$$

Expressions (4.10)- (4.14) provide a useful analytical tool to calculate B and L for every specific TW configuration defined by its cross-sectional parameters α_0 and ν. Additionally, they allow to build a normalized $B_N - L_N$ chart such as that in Fig. (4.4).

The low-loss (LL) and velocity matching (VM) operative ranges, characterized by the BL and BL^2 trade-off rules, respectively, are clearly distinguished in the chart. As shown, the reference B_M and L_M values can be advantageously used to express the trade-off figures of merit in a compact and easy to remember way as $BL = 2B_ML_M$ and $BL^2 = 4B_ML_M^2$, respectively.

Two additional trade-off ranges, quasi low loss (QLL) and quasi velocity matching (QVM), have been identified in which the applicable trade-off figures of merit can be given as $BL^{\frac{7}{6}} = \frac{5}{4}B_ML_M^{\frac{7}{6}}$, and $BL^{\frac{5}{3}} = \frac{7}{4}B_ML_M^{\frac{5}{3}}$, respectively [89].

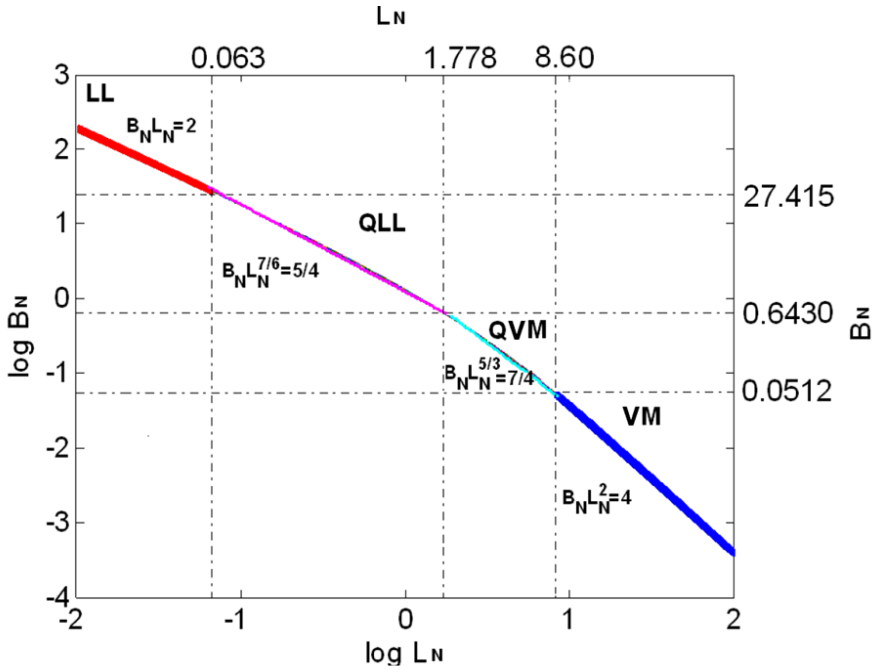

Figure 4.4: Normalized $B_N - L_N$ chart.

The limiting B_N and L_N values for a calculated 10% maximum departure of the trade-off rule against solutions to (4.2) are also given in the chart.

Table 4.1 summarizes the $L_N - B_N$ limits for each trade-off zone as well as the particular figure of merit corresponding to each one.

The chart in Fig. (4.4) offers an insightful and complete picture of the $B - L$ trade-off and clearly shows four operative margins where the B to L figure of merit takes simple forms. Any MZM configuration in terms of B, L, α_0 and ν can be graphically placed in this chart, and can be moved from one region to another for a desired performance, by changing the parameters.

It is worth noting that operation into a specific trade-off margin (LL, QLL, QVM, VM) is dependent not only on the values of α_0 and ν, but also on the target $B-L$ values of every specific application. Thus, one can always work into the VM margin for example, regardless of the cross-sectional configuration with only choosing to work with a long enough L/narrow enough B ($L > 8.60L_M, B < 0.0512B_M$), provided of course that the values obtained have a physical relevance and guarantee the applicability of the approximations of the model. This means that a MZM with an arbitrary value $\nu \neq 0$ can be considered approximately matched when its B_N and L_N are placed in the VM region of the chart, and therefore the BL^2 trade-off can be applied to this MZM.

This finding is in accordance with the work of Chowdhury and McCaughan [55] who concluded

	LL	QLL	QVM	VM
L_N	<0.0630	0.0630-1.7780	1.7780-8.600	>8.600
B_N	>27.415	0.6430-27.415	0.0512-0.6430	<0.0512
Fig. of Merit	$BL = 2B_M L_M$	$BL^{\frac{7}{6}} = \frac{5}{4} B_M L_M^{\frac{7}{6}}$	$BL^{\frac{5}{3}} = \frac{7}{4} B_M L_M^{\frac{5}{3}}$	$BL^2 = 4B_M L_M^2$

Table 4.1: L_N and B_N limits and figures of merit.

that the VM figure of merit, for a given $\alpha_0 = 6.9Np/m - \sqrt{GHz}$ and $|n_m - n_{opt}| \leq 0.03$, was valid to a 10% error for a $B < 30$ GHz and $L > 4.7$ cm. By applying the general expression in our model to those specific values of α_0 and ν, we obtain $B < 0.0512B_M = 35$ GHz and $L > 8.60L_M = 3.8$ cm.

The next step is to apply the trade-off rules to several MZM designs to test their accuracy. Five $LiNbO_3$ MZM designs were chosen as examples to test the performance of the MZM analytical model presented. Their characteristics are displayed in table (4.2). The relevant trade-off margin using the limits of table 4.1 has been determined for each case. We have listed also the B of each reference as measured, as given by the complete closed-form expression (4.10) and as approximated using the corresponding trade-off rule. Depending on the specific definition of B used in each reference, optical (o) or electrical (e), the appropriate k_ν and k_α constants had to be used in the reference L and B definitions in (4.8) and (4.9).

Cases	Lucchi et.al.	Noguchi et.al.	Aoki et.al.	Rangaraj et.al.	Minakata
Reference	[53]	[90]	[91]	[92]	[93]
$\alpha_0(Np/cmGHz^{-1})$	0.0470	0.0864	0.0288	0.1046	0.0461
ν (ns/cm)	0.0027	0.0017	0.0050	0.0043	0.0033
L(cm)	4.3	2.7	3.5	2.5	4
B (GHz)(measured)	10(e)	40(o)	14(e)	23(o)	28(o)
B (GHz) (Eq. 4.10)	11.2(e)	38.9(o)	16.8 (e)	24.4(o)	28.3(o)
B (GHz) (Rule)	10.4(e)	36.4(o)	16(e)	23.5(o)	27.6(o)
L_N	5.7158	5.6206	0.9433	3.0156	1.2212
B_N	0.1024	0.1054	1.4071	0.2888	1.0157
trade-off	QVM	QVM	QLL	QVM	QLL

Table 4.2: Characteristics of the reference modulator configurations.

As seen, excellent agreements with a discrepancy under the 20% confirm that the analytical model here described is well suited to assessment of the $B - L$ trade-off in MZM.

As an example of the usefulness of the trade-off rules, two representative MZM designs of the QVM and QLL zones, the MZM of [53] and [91], will be improved in terms of B at expenses of lower L, keeping their cross-section parameters α and ν constant.

The design of [53] will increase B from 10.4 to 15.6 GHz, a 50% improvement. The QVM trade-off is $BL^{5/3} = \frac{7}{4} B_M L_M^{\frac{5}{3}} = 118.25$ GHz $cm^{5/3}$. The limit values of B and L of the QVM zone for this

design are found through the normalized B_N and L_N, and shown in table 4.3.

Table 4.3: QVM zone limits for the MZM of [53].

L_{min} (cm)	1.33
L_{max} (cm)	6.47
B_{min} (GHz)	5.82
B_{max} (GHz)	70.1

We check that for this $B = 15.6$ GHz, the design is kept in QVM and therefore the trade-off rule can be used to predict the L value. Using the trade-off rules as follows

$$L = \left(\frac{118.25 GHz \cdot cm^{5/3}}{15.6 GHz} \right)^{3/5} = 3.37 cm, \tag{4.15}$$

reducing the L from 4.3 to 3.37 cm. Here, the decrease in L, and therefore the increment in V_π, is around 21%. Using the complete analytical closed-form expressions of (4.10)- (4.14) the value of $B = 16.8$ GHz is obtained.

As seen in table 4.3 the QVM margin encompasses a broad margin of B and L that almost exhausts the range of practical relevance to MZM design. Whenever a value outside QVM could be of interest, say VM, the VM figure of merit ($BL^2 = 4B_M L_M^2$) may be applied starting from the limiting values (5.82 GHz, 6.47 cm). For example, for a $B = 2.5$ GHz, the corresponding L would be 9.87 cm.

The design of [91] will be also improved in a 50% of B from 16 to 24 Ghz. Again the target B is located in the same figure of merit margin QLL, with limiting B and L values displayed in table 4.4.

Table 4.4: QLL zone limits for the MZM of [91].

L_{min} (cm)	0.23
L_{max} (cm)	6.59
B_{min} (GHz)	7.67
B_{max} (GHz)	327.25

The trade-off is $BL^{7/6} = \frac{5}{4} B_M L_M^{\frac{7}{6}} = 69$ GHz $cm^{7/6}$, and therefore L will be decreased to

$$L = \left(\frac{69 GHz \cdot cm^{7/6}}{24 GHz} \right)^{6/7} = 2.47 cm. \tag{4.16}$$

In this case L reduces in a $\sim 30\%$ and consequently V_π should rise approximately by the same amount. The B obtained with (4.10)- (4.14) is 25.6 GHz. We would like to stress here that even when

they are not as intuitive and straightforward, the complete $B-L$ closed-form relations in (4.10) to (4.14), may also be used to find B as a function of L and vice versa.

As observed, in the QVM zone the price to pay for an increment of V_π is a 9% lower than in the QLL region, for the same percentage of enlargement in B.

So far the potential values of the $B-L$ trade-off for a fixed CPW geometry have been analyzed. Whenever the trade-off can not satisfy a given $B-L$ requirement, an improvement of the cross-section parameters values may be targeted. In the next section normalized $B-L$ charts are defined which are shown to provide a useful graphical approach to assessment of different strategies for CPW cross-section parameters tailoring.

4.4 Normalized Bandwidth and length charts

A set of normalized parameters is defined as $H=\alpha_0 L$, $F=\nu L$, $J=\nu B$ and $K=\alpha_0\sqrt{B}$. The expressions (4.10) and (4.11) are rearranged as

$$B = 2^{-4/3} T \left(\frac{k_\nu^2}{\sqrt{k_\alpha}}\frac{H}{F^2}\right)^{2/3} \left[1-\sqrt{T^{-3/2}-1}\right]^2, \tag{4.17}$$

$$L = \frac{1}{2}\frac{k_\nu^2}{\sqrt{k_\alpha}}\frac{K}{J^2}\left[\sqrt{\left(2\frac{\sqrt{k_\alpha}J}{k_\nu K}\right)^2+1}-1\right], \tag{4.18}$$

with T as in (4.12) with

$$W = \frac{3^{3/2}}{2^4}\left(\frac{k_\nu}{k_\alpha}\frac{H^2}{F}\right). \tag{4.19}$$

Expressions (4.17) and (4.18) allow to build normalized B and L charts as a function of $\alpha_0 L$ - νL and νB-$\alpha_0\sqrt{B}$, respectively. These equations are very useful due to the fact that they relate all the parameters in one chart, which permit to better tailor the geometry in order to achieve the desired performance.

The MZM designs of [53], [90], [35], [92] and [93] are represented in their corresponding B chart of Fig. (4.5), depending on the electrical or optical character of each measure. As expected, the location of each design in the B chart agrees with their measured values, displayed in table 4.2. Also the L charts have been built for the optical and electrical case of the MZM references under analysis, Fig. (4.6).

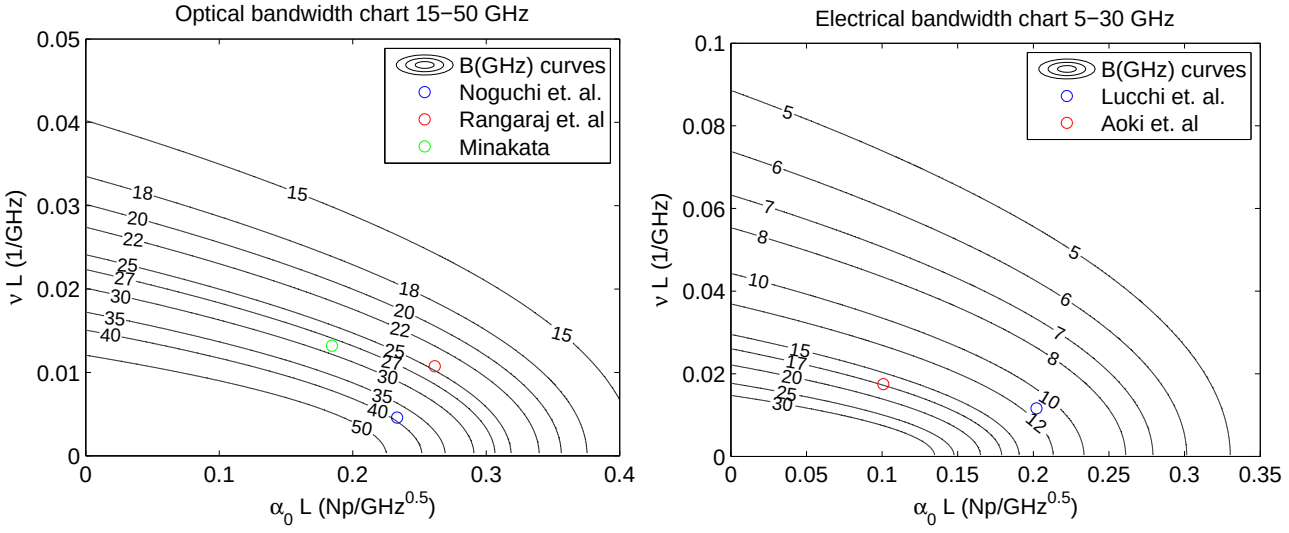

(a) (b)

Figure 4.5: MZM B chart for (a) optical, and (b) electrical B as a function of $\alpha_0 L$ and νL.

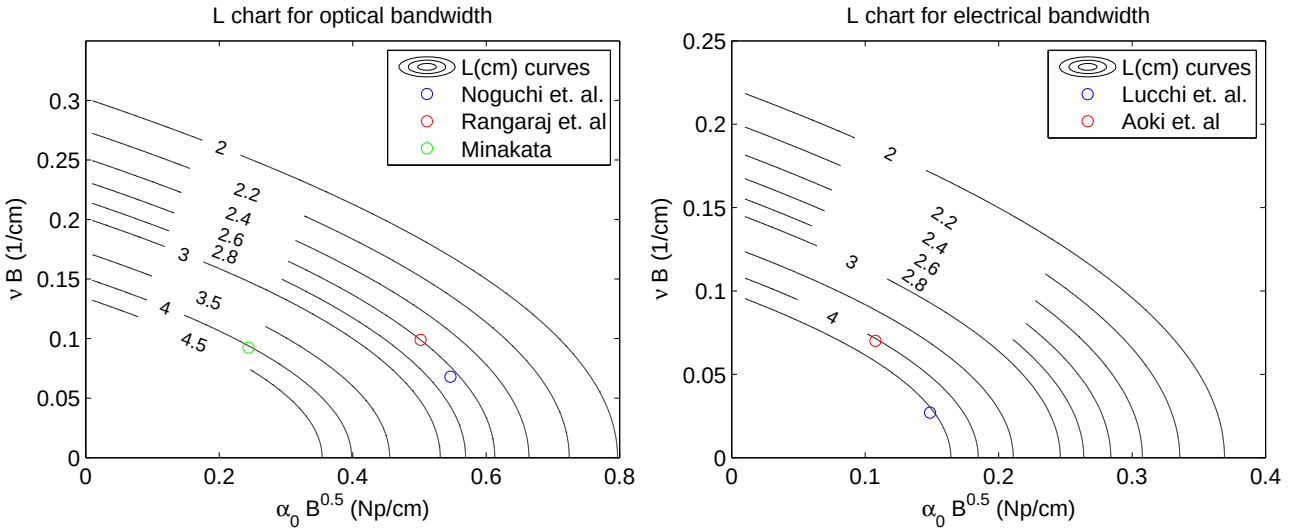

(a) (b)

Figure 4.6: MZM length charts for an (a) optical and (b) electrical B, as a function of $\alpha_0\sqrt{B}$ and νB.

In [73] Chung et.al. also proposed B and L contour plots as a function of α_0 and ν, but for a fixed L and B, respectively. The charts obtained here include the L and B values in the normalization, so that the charts may be used for any L and B. Any of the fixed B and L charts of [73] may be simply obtained as scaled versions of the normalized charts of Figs. (4.5) and (4.6)

4.4.1 Optimization of MZM using B-L charts

The MZM thin film design of [94] and the SiO_2 buffer layer design of [95] will be used as the base for optimized MZM proposals with specific performance in terms of extended B, and or, reduced V_π.

As seen in Fig. (4.7) the original configurations provide a starting point in the chart from where to reach a final B constant curve. The various paths represent different optimization strategies to achieve the goal, V1: ν is reduced while α_0 remains constant, V2: α_0 is the only parameter that decreases, and V3: both α_0 and ν are reduced.

Starting from the thin film design of [94], we plan on extending B^e from 24.2 GHz to 30 GHz while for the buffered design of [95] an increase of B^e from 16.4 GHz to 20 GHz is targeted.

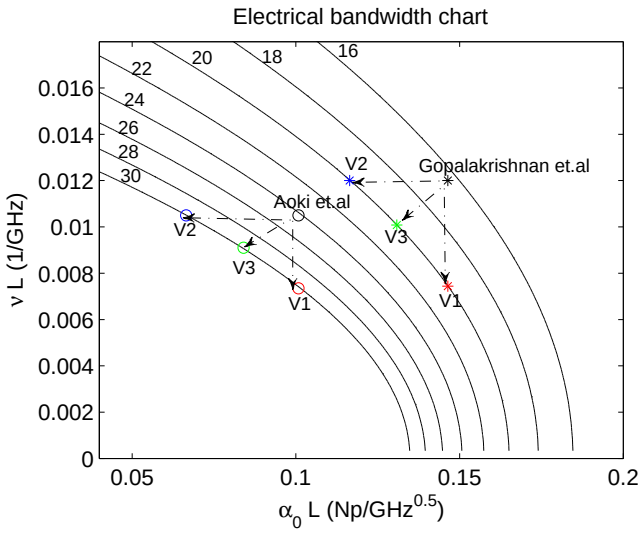

Figure 4.7: Electrical B chart. The reference [94] is represented with a circle and [95] with an asterisk.

The values of the pairs α_0-ν for their correspondent L value in each case are directly obtained from the charts. Tables 4.5 and 4.6 display the values of α_0 and ν for each optimized version of [94] and [95], respectively.

Table 4.5: Parameters of the structure of [94] and the optimized versions to reach $B = 30$ GHz with a constant $L = 3.5$ cm.

	[94]	V1	V2	V3
$\alpha_0(\frac{Np}{cm\sqrt{GHz}})$	0.0288	0.0288	0.0190	0.0240
ν (ns/cm)	0.0030	0.0021	0.0030	0.0026

The values of α_0 and ν of the different versions are the theoretical maximum values to achieve the minimum B desired. By selecting values below the α_0 and ν obtained, a larger B can be reached.

Table 4.6: Parameters of the structure of [95] and the optimized versions to reach $B = 20$ GHz with a constant $L = 2.4$ cm.

	[95]	V1	V2	V3
$\alpha(\frac{Np}{cm\sqrt{GHz}})$	0.0610	0.0610	0.0485	0.0545
ν (ns/cm)	0.0050	0.0031	0.0050	0.0042

Even though the optimization of L, and therefore of V_π, is performable in the B chart, it is not as intuitive as it is in L charts. For this reason, L charts are also built and L optimization examples are presented next.

To illustrate how an improvement in V_π through an increment in L can be performed, the same references will be used. The lengths of designs of [94] and [95] will be increased from 3.5 to 4 cm and from 2.4 to 3 cm, respectively, while keeping the same B. The L chart is built, as shown in Fig. (4.8), where the L curves range covers from 2.4 to 4 cm.

As seen, the target L can be reached by just decreasing ν (V4), reducing α_0 (V5), and reducing both α_0 and ν (V6). The reference structures and their improved versions are placed on the L chart Fig. (4.8), and the propagation parameters of the optimized versions are displayed in tables 4.7 and 4.8 for [94] and [95], respectively.

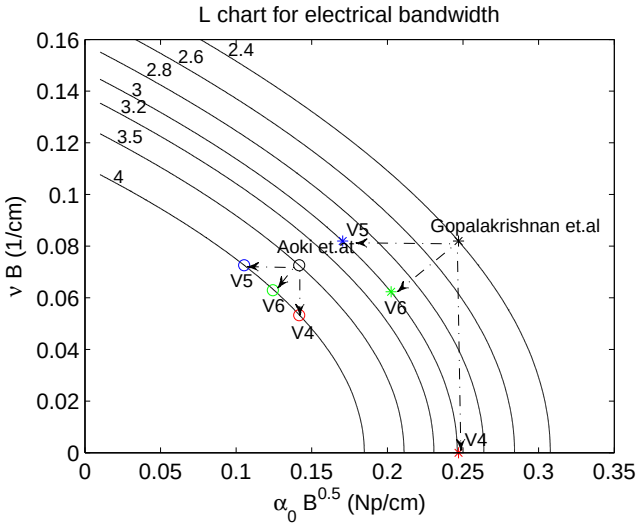

Figure 4.8: L chart for electrical B. The reference [94] is represented with a circle and [95] with an asterisk.

As L is increased we can expect V_π to decrease in approximately the same percentage as long as the cross-section parameters remain constant. As seen in section 2.3, some cross-section parameters have an almost negligible impact over the V_π value, such as t, w_g, h_1 and h_2 for thin film structures.

Table 4.7: Parameters of the optimized version structures of [94] to get $L = 4$ cm keeping constant $B = 24.2$ GHz.

	[94]	V4	V5	V6
$\alpha_0(\frac{Np}{cm\sqrt{GHz}})$	0.0288	0.0288	0.0214	0.2526
ν (ns/cm)	0.0030	0.0022	0.0030	0.0026

Table 4.8: Parameters of the optimized version structures of [95] to get $L = 3$ cm for constant $B = 16.4$ GHz.

	[95]	V4	V5	V6
$\alpha_0(\frac{Np}{cm\sqrt{GHz}})$	0.0610	0.0610	0.0421	0.0500
ν (ns/cm)	0.0050	0	0.0050	0.0038

Therefore, if we use these parameters to improve the $B - L$ condition, this will directly translate into an improvement of the $B - V_\pi$ trade-off. The opposite is also true, if the $B - L$ optimization comes from a change in parameters such as s, w and in the case of a buffer layer h_2, then it is not clear that the $B - V_\pi$ relation is optimized as well.

As observed from the charts, there are infinite combinations of $\alpha - \nu$ for a targeted $B - L$ pair, but their achievement in a practical CPW design will be limited by the technology and the geometry chosen for the CPW cross-section.

Next step is to find the CPW cross-section geometry that features a pair of α_0 and ν for a targeted $B - L$ performance. It is important to take into account that the physical CPW parameters also have to meet the impedance matching condition.

4.5 Summary of the Chapter

An analysis of the available MZM figures of merit was conducted in this Chapter. The limiting cases LL and VM, when the CPW cross-sectional parameters α and ν are neglected, respectively, were revisited.

Compact closed-form expressions which explicitly relate B and L with α and ν were derived by fitting to a parabolic function. The curves were formed by connecting together the points yielding the same B and L values, in a $\alpha_0 - \nu$ plane. Definition of reference normalization B and L values, as a function of the cross-sectional parameters, has allowed to cast the $B - L$ expressions in a compact way, providing a common framework for the analysis of the trade-off in any cross sectional configuration.

A total of four operative $B - L$ margins, LL, QLL, QVM and VM, have been identified, in which approximate and simple trade-off rules apply, defining two new figures of merit for the intermediate ranges besides of the well-known LL and VM figures of merit. The accuracy and convenience of the

model here developed for both, assessing the potential of different cross-sectional structures in terms of achievable B and L, and also for identifying valid strategies for advantageous improvement of the $B-L$ trade-off through appropriate design of the CPW cross-section, has been shown through examples extracted from the reported literature.

Novel B and L charts for the optimization of electro-optical modulators have been obtained, agreeing well with experimental measurements. The charts give an easy and reliable way to project a modulator, allowing to tailor α_0 and ν to meet specific requirements. Over the charts, the different alternative cross-sectional parameter pairs (α,ν) to reach a specific performance in terms of B and L may be understood as different paths taken over the chart to connect the original performance curve to the target performance curve.

Optimized versions of two MZM reported in literature were found with the charts aid improving the $B-L$ trade-off through changes in the CPW cross-sectional parameters.

The $B-L$ trade-off figures of Merit, the $B-L$ analytical expressions as well as the novel B and L charts show promise to constitute powerful tools in advancing the performance of MZM, which is key to the progress of optical communication systems toward meeting the requirements of the communication networks of the future.

Next natural step is to relate the α_0 and ν for the target optimized values to specific changes on the CPW cross-section structure, a task that is undertaken in the next Chapter, gathering results from Chapter 3.

5

Graphic interface tool for the design and optimization of MZM

The work presented in Chapter 3 has allowed to establish a link between the cross-section parameters of CPW (α_0, ν and Z_0) and the geometries that support them, in the form of compact closed-form expressions. It is worth noting that, unlike previous approaches, a great advantage of the PP expressions is that they allow to model accurately both the effect of the electrode thickness, and multilayer substrates, which are effective strategies for improving the MZM performance, and also the asymmetry in the electrodes cross-section, useful for tailoring the frequency chirp associated with the amplitude modulation.

On the other hand, in Chapter 4, a complete analytical model for determining the $B-L$ trade-off and the relation between the MZM system performance features, i. e. maximum modulation B and driving power V_π, with the cross-sectional parameters has been presented.

In this Chapter both results are brought together in an integrated graphical tool (MZM-GIT) developed in Matlab code, that provides a user-friendly approach to the MZM design and optimization problem. The analysis in previous chapters has revealed that the electrode thickening, the use of a thin $LiNbO_3$ film and the insertion of buffer layer are effective strategies for MZM optimization. Therefore, the MZM-GIT focuses on these strategies and comes up with an optimized CPW geometry that fulfills a set of system parameters.

The optimization strategies and the design alternatives offered by the MZM-GIT are illustrated through representative examples extracted from literature. Moreover, optimized MZM proposals, focusing in broadband and ultra low power operation are worked out exploiting the features of the MZM-GIT.

The Chapter is structured as follows: section 5.1 deals with the interface software and its parts. Section 5.2 describes the structure of the MZM-GIT. Section 5.3 is devoted to present examples of optimized design starting from MZM configurations extracted from literature. The design proposals are presented and analyzed in section 5.4.

5.1 Graphic Interface tool (MZM-GIT)

The graphic interface has been built over a Matlab environment. For the sake of clarity and visibility of all the parameters involved, the MZM-GIT is based on a single window which gathers all the relevant information classified into different categories: the input parameters panel, the output parameters panel, the visualization panel and the plot panel, respectively identified in Fig. (5.1) by a number 1, 2, 3 and 4.

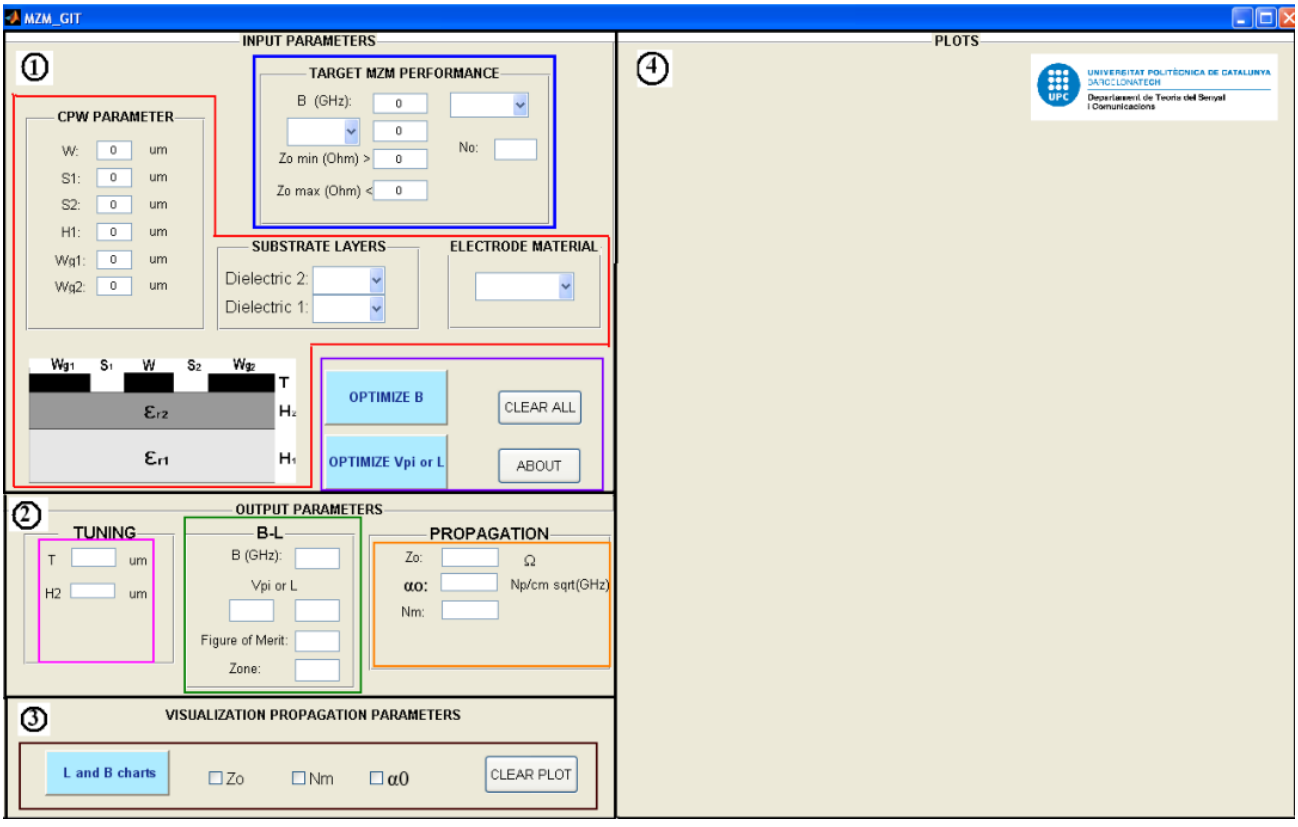

Figure 5.1: Graphic interface tool.

The input parameter panel, numbered with a "1" , contains the "fixed CPW geometry" window (red line square), the "Target MZM performance" window (blue line square) and the optimization buttons (purple line square). A sketch of the CPW cross-section is provided for an easy identification of all the magnitudes. The parameters $T - H_2$ are left as degrees of freedom for reaching the system performances. These parameters have been chosen based on common optimization strategies and as a trade-off between complexity and ability to reach the target performance values, but more degrees of freedom could be added for specific optimization problems.

The material of the substrate layers and the electrodes are also fixed CPW geometry input parameters within the "fixed CPW geometry" window. We have pre-defined SiO_2 and $LiNbO_3$ as possible materials for the substrates, and also the air for substrate 1, to account for backslot CPW cross-section structures, as in [93]. Gold, copper and aluminium for the conductors are pre-defined. In case that other materials would be needed, they can easily be added to the interface code. For single layer substrate, the same substrate material should be entered in both fields.

The "Target MZM performance" window, embraces the targeted system requirement in terms of B, V_π or L, as selected in the specific field, and the bounds for the Z_0 value. Targeting a B and L (V_π) values mean, that depending of the optimization procedure (B or L (V_π) optimization), the targeted parameter to be optimized will be the minimum starting point value to be improved while the other parameter remains constant. On the other hand, always a pre-defined margin for Z_0 needs to be set, restricting the acceptable Z_0 values in the resulting design. The type of B, electrical or optical, can also be selected here by the user, as well as the optical index value.

The purple line square encloses the "Optimize B" and the "Optimize V_π or L" buttons which will start the optimization algorithm targeting a maximum value of the specified parameter.

The output parameters panel, numbered with a "2" in Fig. (5.1), displays the resultant T and H_2 (square of pink line), and the resultant B and L (V_π), the applicable figure of merit and the corresponding trade-off zone (within the green line square). Also the CPW propagation parameters Z_0, α_0 and N_m are displayed in this panel (within the orange line square). Depending whether the V_π or the L optimization has been selected in the target MZM performance window, the output parameters set would be $B - L$ or $B - V_\pi$.

The visualization panel (brown line square) provides some options for the visualization of the propagation parameters against T, H_2 and f. Also the L and B charts can be given. These plots allow to envision possible optimization strategies. Examples of the plots are shown in Fig. (5.2).

Additional degrees of freedom, beyond the $T - H_2$, could easily be included to the MZM-GIT. For

simplicity, in this first version we focus on these two parameters, but the decision is up to the designer.

In the next section, a brief explanation of how the MZM-GIT Matlab code works, is provided.

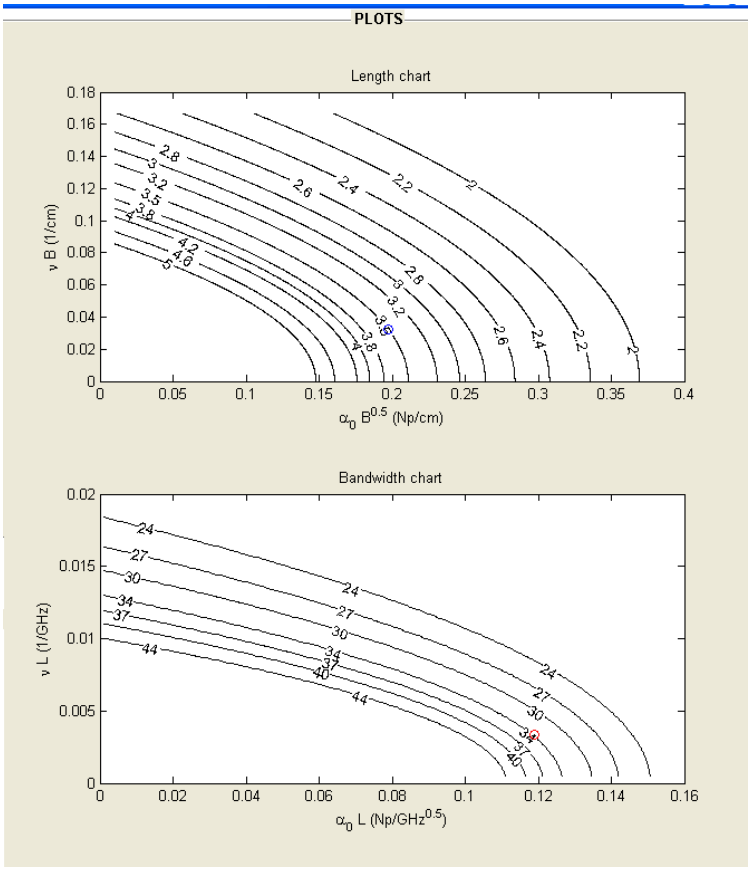

Figure 5.2: Plots of the graphic interface tool for $B - L$ charts.

5.2 MZM-GIT structure

This section describes the basic structure and working procedures followed by the MZM algorithm, as shown in Fig. (5.3).

Once the fixed CPW geometry parameters, and the target performance parameters have been correctly entered and an optimization button clicked, the software starts by first checking if a V_π or L selection has been made.

If the selection is L, then it is on to the next step. If it is V_π, a procedure to determine the relationship between L and V_π for the CPW geometry is run. The $V_\pi - L$ subroutine consists on application of expression (2.11). The core of this subroutine is the estimation of Γ, which follows

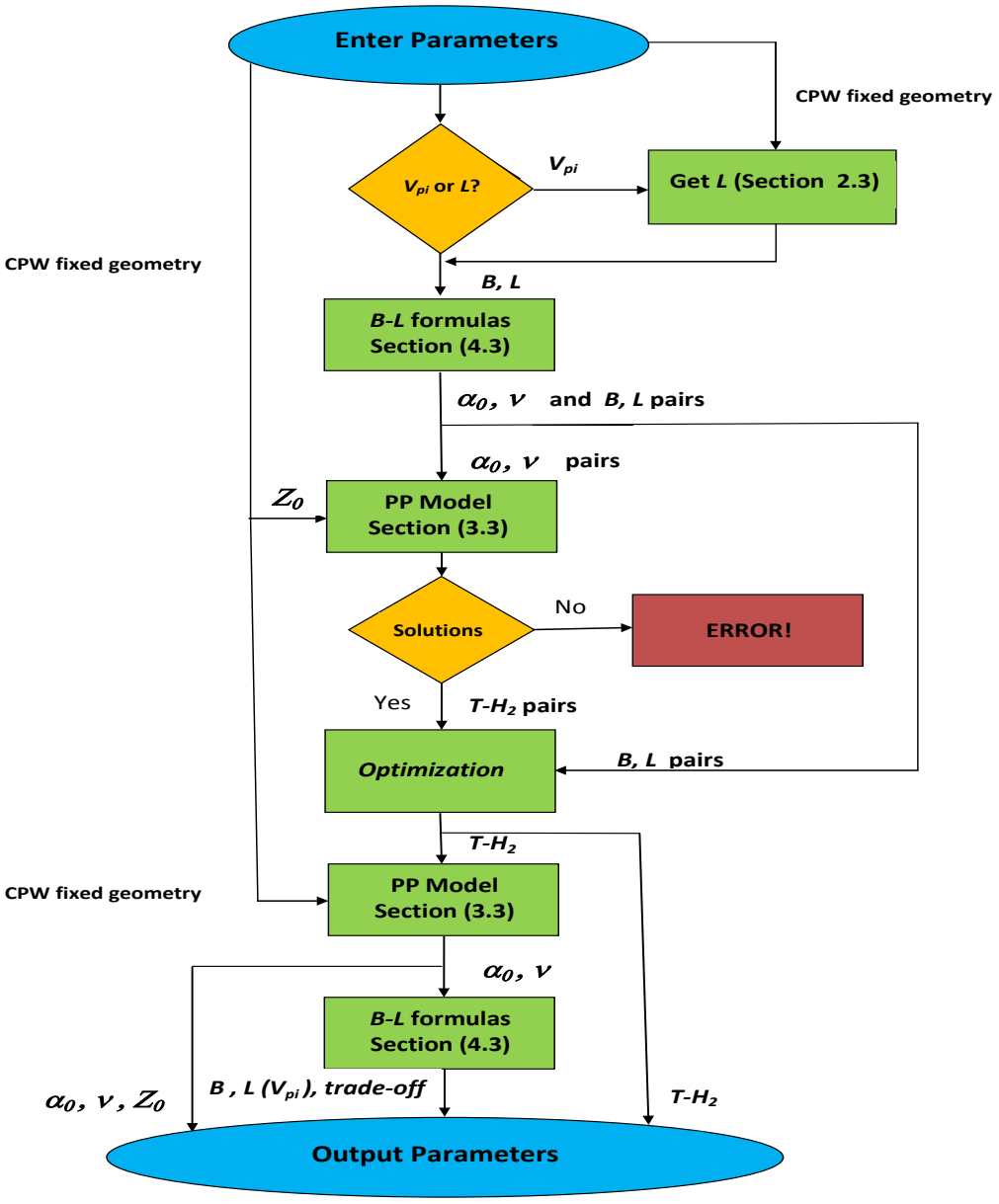

Figure 5.3: Algorithm's diagram of the graphic interface's program.

the process described in section 2.3. To that end, the structure of the optical waveguide needs to be provided.

At this point it is important to stress that the focus of the MZM-GIT is mainly on the optimized design of the electrical wave propagation structure, being that the one most susceptible to design choices and tailoring, while it could be said that the optical propagation structure is basically limited by technological constraints [39]. The optimization of the optical propagation structure is beyond the

scope of this Thesis and we will just make educated guess assumptions over its design with the main purpose of estimating the Γ values, and therefore the V_π.

In order to get a clear organization of the MZM-GIT main window, and to focus attention on the parameters of relevance in the optimization problem, we have chosen to maintain the optical guides design parameters inside the code and not as a user input, as most of the optimization problems of interest here do not show a critical dependence on that design. Instead, a generic optical waveguide design will be used, as described next.

Recalling the optical field expression of 2.13, we set $w_x = w_y = 4\mu m$ for the width parameter. These are typical choices found for example in [39]. As for the waveguide position parameter p, the study in section 2.3 has revealed that the best position for z-cut occurs when the inner edge of the electrodes is aligned with the optical waveguides, while for x-cut it is when the optical guide position is in the center of the gap, with some shift towards the inner electrode edge for wide electrode gaps [56] [58]. We will assume here an x-cut configuration and set $p = (w + s)/2$, in the middle of the gap. Whenever this is not an appropriate choice for the problem under study, the correct p value is easily changed inside the Matlab code.

Once the target B and L values are known, they enter the $B - L$ formulas subroutine, where trough a simple shooting method optimization [96], a set of $\alpha_0 - \nu$ pairs fulfilling the target $B - L$ are selected. The parameters of the shooting have been validated trough extensive testing and are listed in Appendix (G).

With the $\alpha_0 - \nu$ pairs selected, and the fixed CPW parameters, the PP model subroutine looks for valid $T - H_2$ pairs that allow to comply with the targeted Z_0 margin. These $T - H_2$ pairs together with their correspondent $B - L$ values go trough the optimization subroutine which select the best $T - H_2$ pair for an optimized solution. If no $T - H_2$ pairs can be found, an error message pops-up and the program ends. The final $T - H_2$ pair is combined with the fixed CPW geometry parameters to get the final α_0 and ν values, and from these through the $B - L$ formulas, the values of the final B (L). In case the optimization of V_π had been selected, this value would be obtained from L using the Γ as obtained in the "Get L subroutine". Finally, all the output parameters of the optimized MZM structure are provided by the software in the "Output parameters" panel.

Next section deals with the improvement of three MZM designs using the MZM-GIT developed. The examples of optimization will focus on an extension of B and improvement of the Z_0 matching through proper selection of T and H_2.

5.3 Improving the CPW for optimized MZM

The MZM designs of an asymmetric, $LiNbO_3$ thin film, and a SiO_2 structure of [35], [94] and [95], respectively, will be used as benchmark to shape their CPW cross-sections, in order to optimize their performance.

We start with the asymmetric CPW of [35], which has been tailored to provide a chirp value of 0.65. Fig. (5.4) displays the MZM-GIT window with all the relevant geometrical data, which can also be found in the first column of table 5.1. The α_0 value is not provided by the authors, therefore we calculate it with our PP model approach.

The values of S will be kept unalterable to preserve the chirp value, and also the $V_\pi = 2.7$ V, and we will focus on extending the value of B from 20 to 30 GHz and to increase the value of $Z_0 = 46\Omega$ to make it closer to 50Ω.

As seen in the screenshot of Fig. (5.4), we set the targeted B to 20 GHz, as the start point. The Z_0 range is fixed between 48.5 and 50Ω, and L is kept with its original value of 4 cm. After clicking the "B optimization" button, a failure message pops up, telling us that the optimization is not possible for the set target values and the degrees of freedom provided. Therefore, a change in the fixed geometry parameters or a reduction in the goal performance is required. The options of changing the CPW geometry, the L or the B are not acceptable, as we want to keep the chirp value and the V_π constant and to increase B. The only option is to relax the impedance range to $47 - 50\Omega$ in the next run.

As seen in Fig. (5.5), an improved $B = 23$ GHz is obtained which is better than the starting value but still below our expectations. A third attempt to increase B is performed, with a further reduction in the Z_0 to $46 - 50\Omega$.

The results are as shown in Fig. (5.6). This time the increment in B reaches up to 30 GHz, achieving our goal of a 50% extension in B, even though Z_0 could not be increased from its original value.

Table 5.1 summarizes the MZM parameters for the different versions of optimization for the MZM design of [35]. The CPW propagation parameter results have been compared with HFSS simulations with excellent values of DM, given in the table.

Version 1 of [35] barely improves the performance of the original MZM. The small decrease of T from 25 to $21.5\mu m$ yields a limited improvement over Z_0, but at the same time a deterioration of the velocity matching condition ($n_{opt} = 2.2$). This is compensated by a decrease of the $LiNbO_3$ thin film layer from 8.5 to $8\mu m$, which also contributes to the Z_0 increase and to some overall marginal

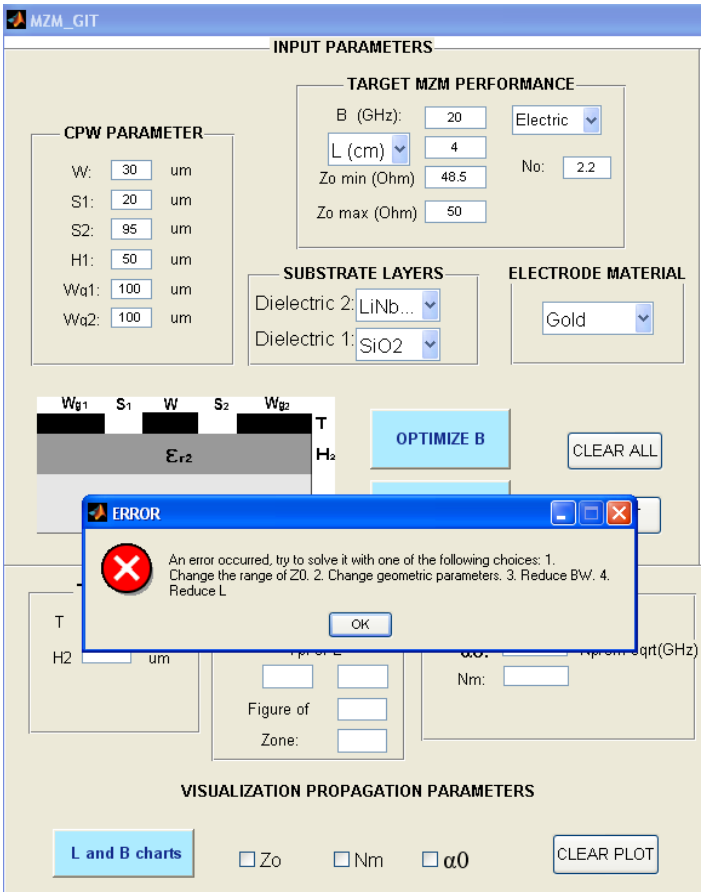

Figure 5.4: MZM-GIT screenshot of the unsuccessful improvement design of [35].

Table 5.1: Parameters of the CPW structure of [35] and the resultant versions for its optimization.

	[35]	Version 1	Version 2
L (cm)	4	4	4
B (GHz)	20	**23**	**30**
V_π (V)	2.7	2.7	2.7
Z_0 (Ω)	46	**47** ($DM = 3\%$)	46 ($DM = 1.3\%$)
α_0 $dB/cm - \sqrt{GHz}$	0.0296 (calculated)	0.0306 ($DM = 1.9\%$)	0.0307 (DM=1.7 %)
n_m	2.27	**2.266** ($DM = 1.4\%$)	**2.232** ($DM = 0.9\%$)
w (μm)	30	30	30
$s^{\pm}$ (μm)	20,95	20,95	20,95
h_1 (μm)	50	50	50
t (μm)	25	**21.5**	**23.6**
h_2 (μm)	8.5	**8**	**8**

improvement of the velocity matching allowing for only modest improvements of 15% in B and 2% in Z_0.

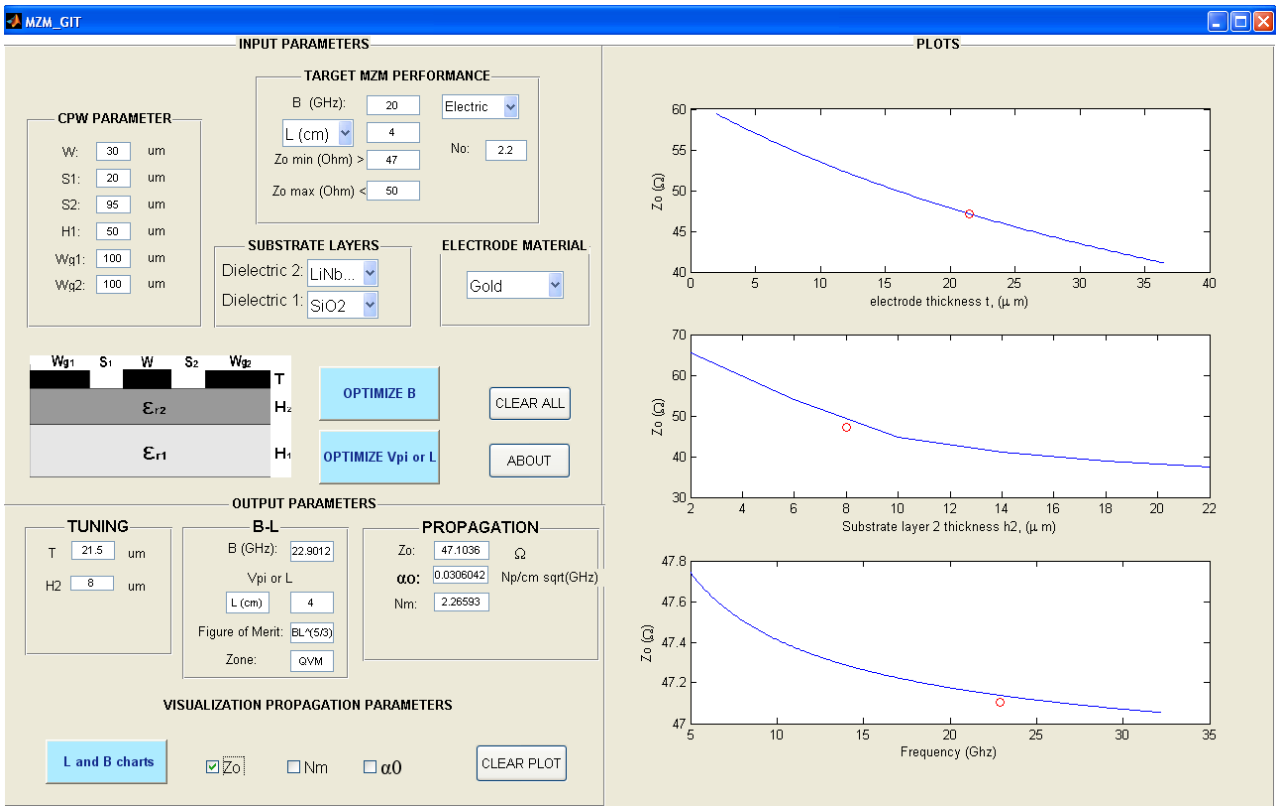

Figure 5.5: MZM-GIT screenshot of the optimized version 1 of the design of [35].

The second optimization (Version 2), with a larger margin for Z_0 $(46-50\Omega)$, provides a still smaller change in T from 25 to 23.6μm with the same reduction in H_2, which yields a more pronounced improvement over velocity matching allowing to reach the 30 GHz targeted B, but then no gain over the impedance matching is obtained. The loss constant in both cases remains almost unaltered as compared with the calculated value of the original version.

It is worth stressing that these examples of optimization are useful to identify design trade-offs and sensitivities to all the parameters involved, and that they can only provide a first starting point guess and beneficial tips about trends which could be helpful in the prototype design process.

Moving on the $LiNbO_3$ thin film MZM design of [94], whose features are summarized in table 5.2 and in the screenshot of Fig. (5.7), a low value of $Z_0 = 38\Omega$ catches attention. That results in a return loss (RL) value of -17.3 dB. Our optimization here will then again focus on improvement of the impedance matching condition as well as B extension. We start by entering all the relevant fields

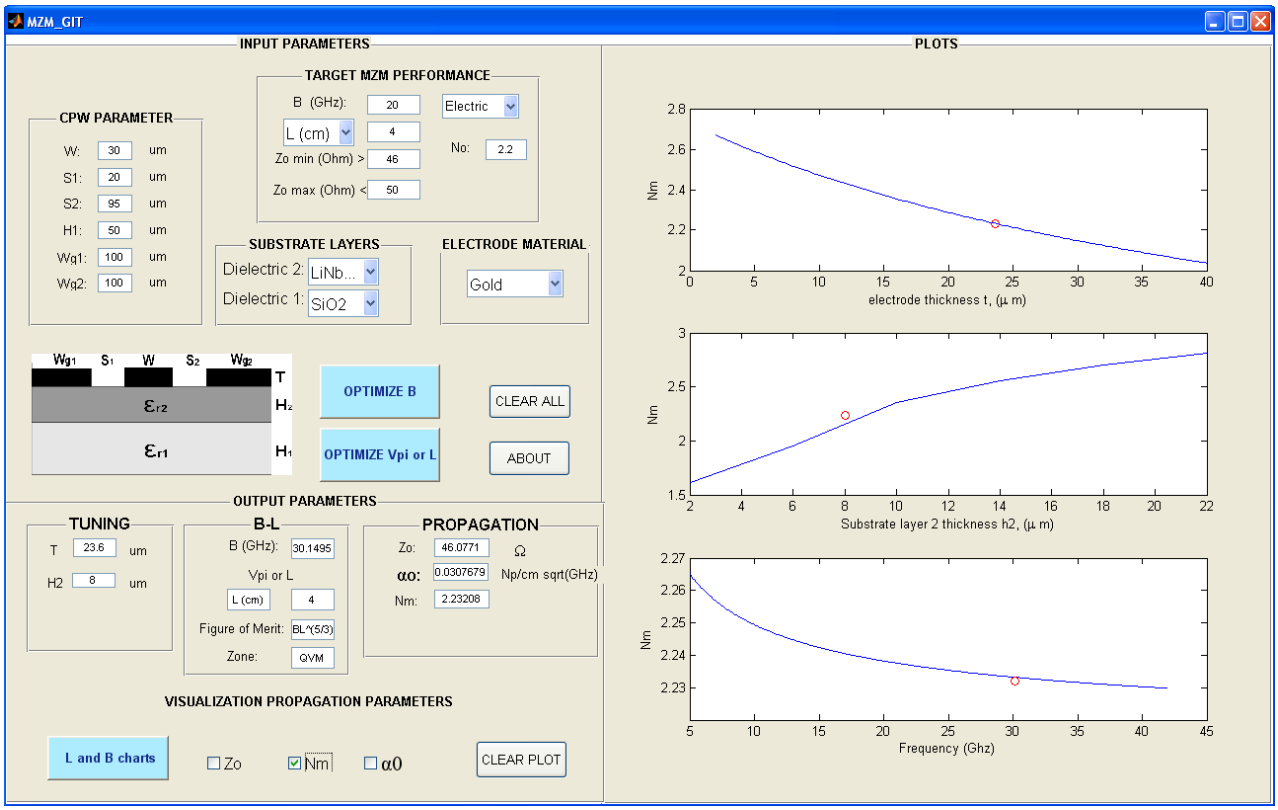

Figure 5.6: MZM-GIT screenshot of the optimized version 2 of the design of [35].

into the MZM-GIT as shown in Fig. (5.7) with a Z_0 margin between $48.5 - 50\Omega$. The MZM-GIT pops up an error message, so we relax the matching to $40 - 50\Omega$. The result is now $B = 33$ GHz and $Z_0 = 42\Omega$ which are achieved by reducing T from 20 to $12.6\mu m$ and H_2 from 8.5 to $4.5\mu m$. It is worth noting that the resultant configuration indeed has a better velocity matching (with $n_m < n_{opt}$) but a higher α_0. This is in contrast to common belief that better performance should always come from more reduced values of α_0 and ν, but it rather proofs that optimized configurations could be found through appropriate α_0 and ν trade-offs. In order to further illustrate this idea, the optimization path followed from the original configuration of [94] to optimized Version 1 has been added to the normalized $B - L$ charts in Fig. (5.7).

A second optimization was aimed to achieve a better Z_0 result, and then, following the trends observed in section 2.4.2, we choose to increase S at the risk of increases in V_π, with Z_0 margin again to $48.5 - 50\Omega$, as observed in Fig. (5.8). First, we try to raise S from 21 to $23\mu m$, and performed

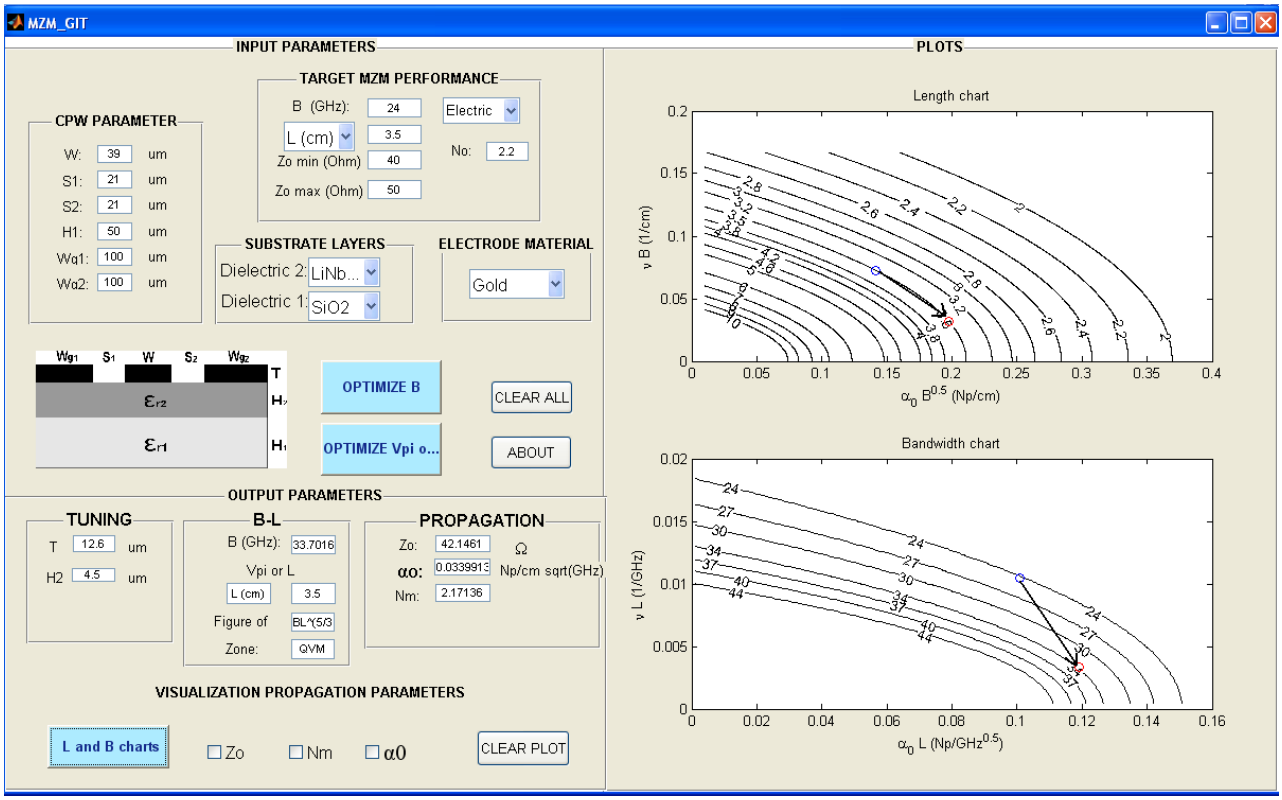

Figure 5.7: MZM-GIT screenshot of the optimized version 1 of the design of [94].

again a B optimization with no positive results, and then we set S to $25\mu m$. In this case, B rises to 36 GHz and the Z_0 reaches the value of 49.8Ω, with an improved $RL = -54$ dB. This is achieved trough a significant decrease in T down to $7.5\mu m$, with H_2 fixed to $4.5\mu m$, same as in the previous optimization. The downside is that as S is extended in $\sim 20\%$, V_π will increase approximately by the same amount. The plots of Fig. (5.8) show opposing trends of α_0 against the two tuning parameters, while the decrease in T causes α_0 to increase, that is compensated by the decrease in H_2. The extension in S also contributes to making α_0 lower. However, the large drop in T (from 20 to $7.5\mu m$) makes α_0 in this version to be finally higher than in the original configuration. This effect is compensated in the overall $B - L$ performance with a better velocity matching accomplished by a decrease in H_2, as observed in the n_m plots of Fig. (5.6). For better assessment of the quality of the cross-section of Version 2, the applicable $B - L$ rule was applied (QVM, as seen in Fig. (5.8)), in order to have a design with $V_\pi = 2$ V. The resulting performance values are listed as Version 2a in table 5.2.

Table 5.2 summarizes the MZM parameters of the original design of [94] and the versions obtained with the MZM-GIT. As observed, in both versions α_0 slightly increases, but this is compensated with a better result in n_m. In both designs B and Z_0 are optimized trough reductions in both T and H_2 while keeping the same L. In Version 2 the increase in gap width allows for better values of B and Z_0, by a further T reduction at the expense of an increase in V_π.

As observed in this last version, the electrode gap S is a very good third choice for another degree of freedom for optimizing the MZM performance, which also is a key parameter for the value of V_π.

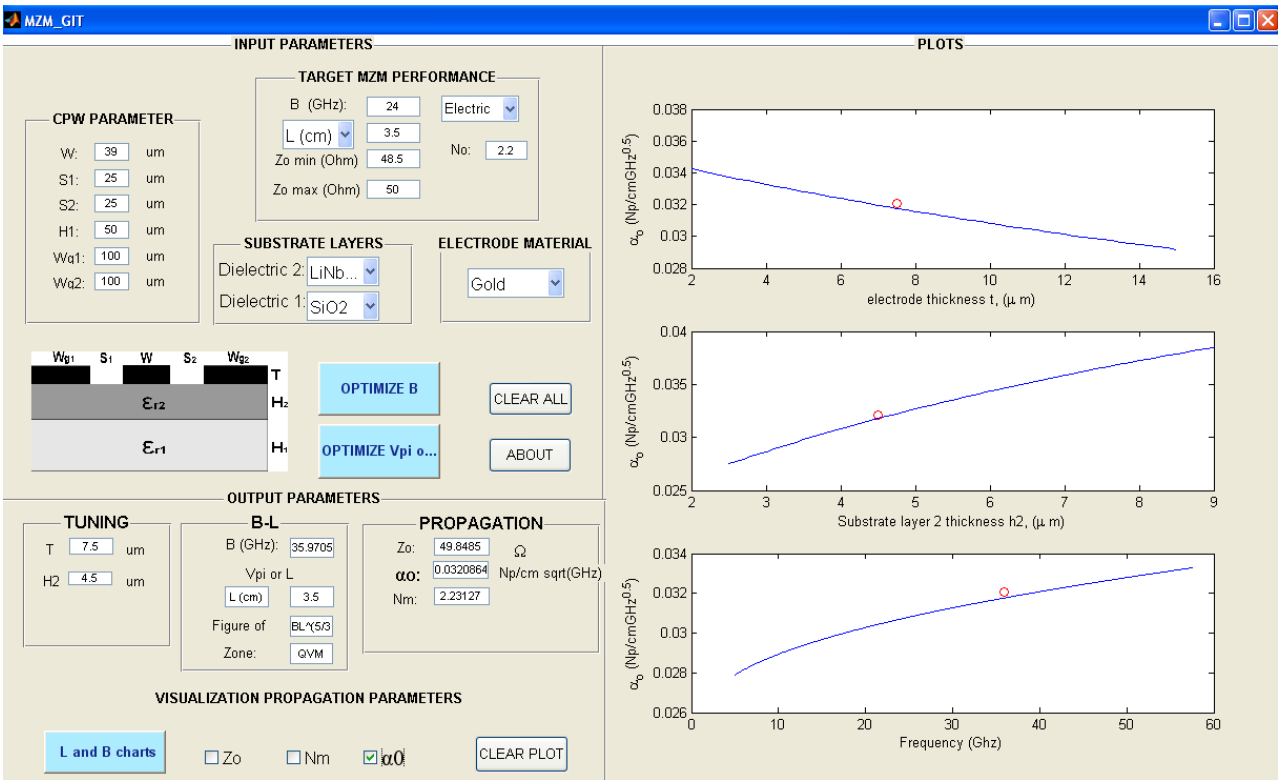

Figure 5.8: MZM-GIT screenshot of the optimized version 2 of the design of [94].

The third design to improve is the SiO_2 buffer layer MZM of [95]. This design has a $L = 2.4$ cm, with a $V_\pi \sim 5$ V and $B = 16.4$ GHz. The complete list of features is summarized in the first column of table 5.3 and in the filled up fields in the screenshot shown in Fig. (5.9). The Z_0 value is not provided by the authors, so we calculated it with the PP model approach obtaining $Z_0 = 40\Omega$. The optical index is 2.15.

Table 5.2: Parameters of the CPW structure of [94] and the resultant versions for its optimization.

	[94]	Version 1	Version 2 - Version 2a
L (cm)	3.5	3.5	3.5 - **4.2**
B (GHz)	24.2	**33**	**36** - **26.5**
V_π (V)	2	2	**2.4** - 2
Z_0 (Ω)	38	**42** ($DM = 5\%$)	**49.8** ($DM = 4.41\%$)
$\alpha_0\ dB/cm - \sqrt{GHz}$	0.0288	**0.0339** ($DM = 2.54\%$)	**0.0320** (DM=6.15 %)
n_m	2.29	**2.171** ($DM = 1.32\%$)	**2.231** ($DM = 0.01\%$)
w (μm)	39	39	39
$s^{\pm}$ (μm)	21	21	**25**
h_1 (μm)	50	50	50
t (μm)	20	**12.6**	**7.5**
h_2 (μm)	8.5	**4.5**	**4.5**

In a first version we will try to extend the value of B under the impedance matching condition with a $48.5 - 50\Omega$ range while keeping L to 2.4 cm. The first optimization attempt reaches $B \sim 30$ GHz, which is almost twice the original value. We achieve almost perfect impedance matching with $Z_0 = 49.9\Omega$, as observed in Fig. (5.9). Here T is reduced from 18 to $11.8\mu m$, which entails a poorer velocity matching but better Z_0. The loss in velocity matching is compensated by an increase in H_2 from 0.95 to $1.5\mu m$, which is translated in a rise in V_π as the electric field involved in Γ decreases by the factor EFR of equation (2.19). The EFR of the original version for $H_2 = 0.95\mu m$ is 0.47, while increasing to $H_2 = 1.5\mu m$ in the optimized Version 1 decreases EFR down to 0.37. This is a drop of 23%, therefore the V_π will approximately rise to 6.15 V. If we would like to keep $V_\pi = 5$ V unaltered, the pertinent $B - L$ rule (VM) can be used, to see that Version 1a achieves an increase of up to 19.5 GHz in B with an improved almost perfect Z_0 matching and the same $V_\pi = 5$ V.

A second optimization over [95] aims at reducing V_π. In an first attempt the S value is kept constant, and the tentative V_π is set to 4 V, keeping the same Z_0 margin of $48.5 - 50\Omega$, and $B = 16$ GHz fixed. The MZM-GIT found no valid results and therefore a less challenging Z_0 margin of $40-50\Omega$ is set leading to the same unsuccessful result. As a third option then a change in S is considered. As seen in section 2.3 in non-buffered structures the V_π decreases as the S is decreased, but in presence of a buffer layer, the S has an added impact coming from the EFR factor, see Fig. (2.8).

The S is increased to $20\mu m$, since as seen in the trending analysis in section 2.4.2, this helps both the impedance and velocity matching, and this time the results are satisfactory, as observed in Fig. (5.10). The V_π is reduced to 3.6 V ($\sim 30\%$). As seen in the Z_0 plots, when increasing the buffer layer thickness the Z_0 will rise, but also V_π. Once again, it is demonstrated that the S parameter is key for

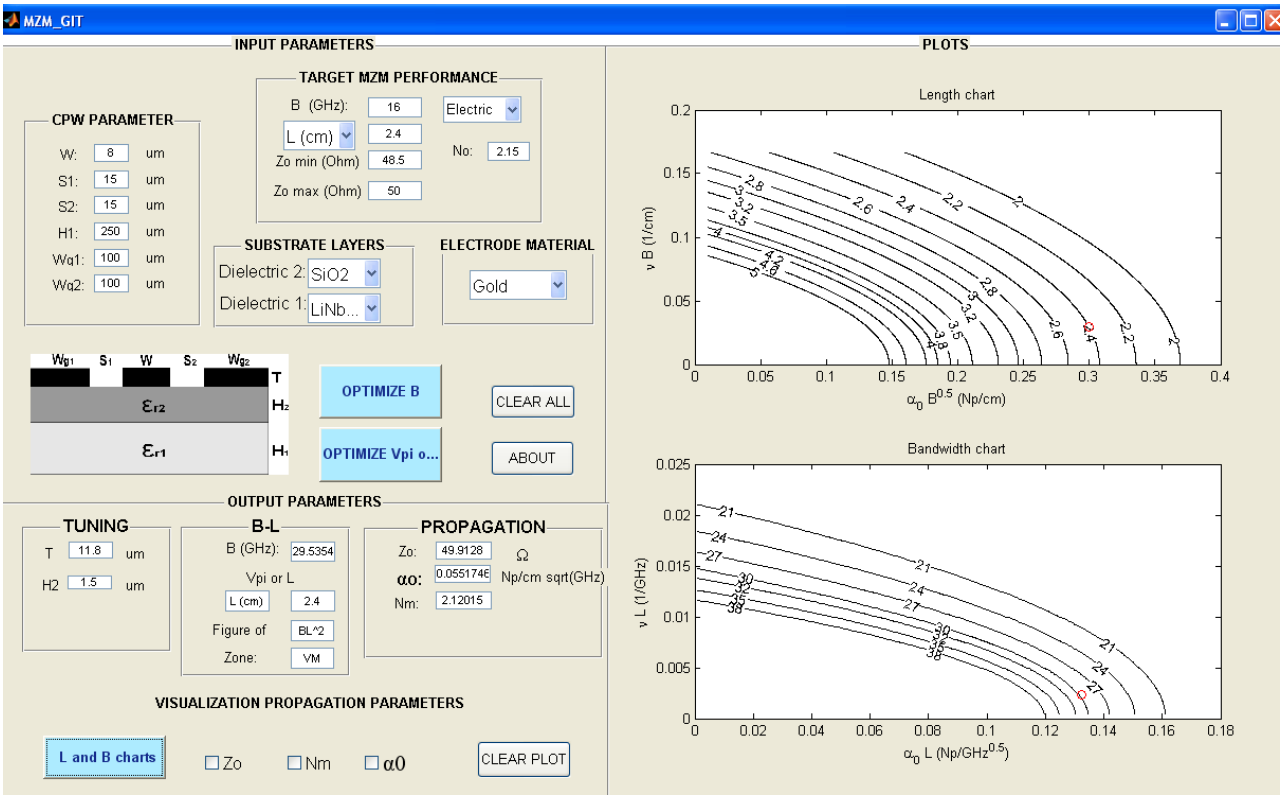

Figure 5.9: MZM-GIT screenshot of the version 1 of the design of [95].

the tuning of the CPW cross-section.

In table (5.3) the MZM characteristic of [95] and the two versions are shown. Results given by the MZM-GIT have been compared with HFSS simulations. Again, excellent agreement is observed.

The three MZM designs under analysis were optimized with different versions. In the next section high frequency and low switching voltage MZMs are proposed and discussed.

5.4 Optimized MZM design proposals

Modern optical communications demand high speed MZM, presently reaching up to 100 Gb/s. Also designs with low switching voltages ($V < 2$ V) are needed for inexpensive drivers [29].

In this section, we use the MZM-GIT to obtain the parameters that can achieve a MZM design with $B^e \sim 100$ GHz. Another example where the L will be enlarged to obtain a low V_π will be also

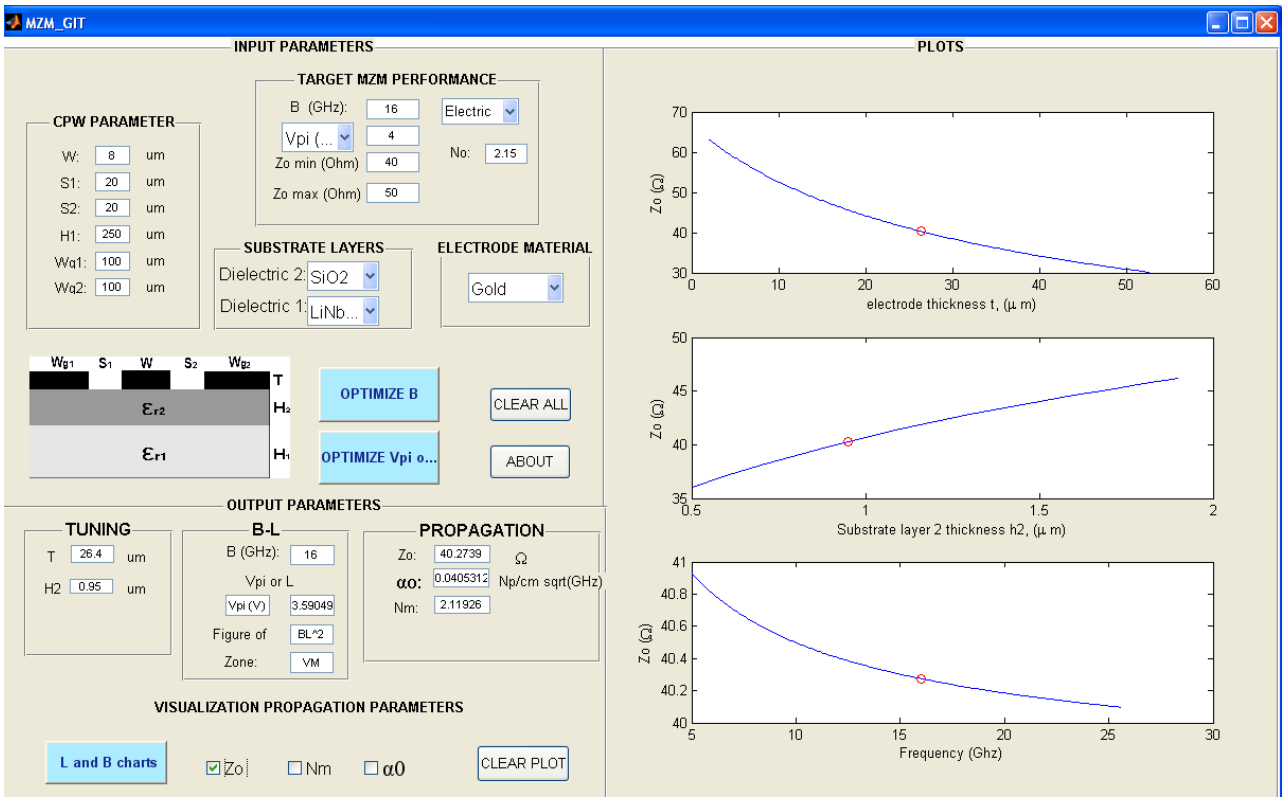

Figure 5.10: MZM-GIT screenshot of the version 2 of the design of [95].

Table 5.3: Parameters of the CPW structure of [95] and the resultant versions for its optimization.

	[95]	Version 1 - Version 1a	Version 2
L (cm)	2.4	2.4 - **2.95**	**4.4**
B (GHz)	16	**29.5** - **19.5**	16
V_π (V)	5	**6.15** - 5	**3.59**
Z_0 (Ω)	40 (calculated)	**49.9** ($DM = 5.4\%$)	**40.27** ($DM = 4.5\%$)
α_0 $dB/cm - \sqrt{GHz}$	0.0610	**0.0552** ($DM = 4.8\%$)	**0.0405** (DM=1.6 %)
n_m	2.3	**2.120** ($DM = 4.6\%$)	**2.119** ($DM = 4.4\%$)
w (μm)	8	8	8
$s^{\pm}$ (μm)	15	15	**20**
h_1 (μm)	250	250	250
t (μm)	18	**11.8**	**26.4**
h_2 (μm)	0.95	**1.5**	**0.95**

shown. In both examples, the structure will be a $LiNbO_3$ x-cut thin film. The parameters w_x and w_y will be set to $4\mu m$. This time the position of the optical guides will be tailored to get the highest

possible Γ/s relation, since as it was shown in section 2.3, a shift towards the inner edge of the hot electrode improves the value of Γ/s.

For the first proposal of broadband MZM, we fixed W, S, W_g and H_1 to usual values in experimental designs of thin film MZM in literature as a starting point, see [35], [91], [97]. Following the trendings in section 2.4.2, after several optimization attempts, where the fixed parameters were tailored, finally a $B \sim 100$ GHz, with $Z_0 = 49.7\Omega$ is attained, as shown in Fig. (5.11). A short $L = 2$ cm is fixed, which will probably translate into a high V_π, therefore special care has to be put in the optical guides size and position.

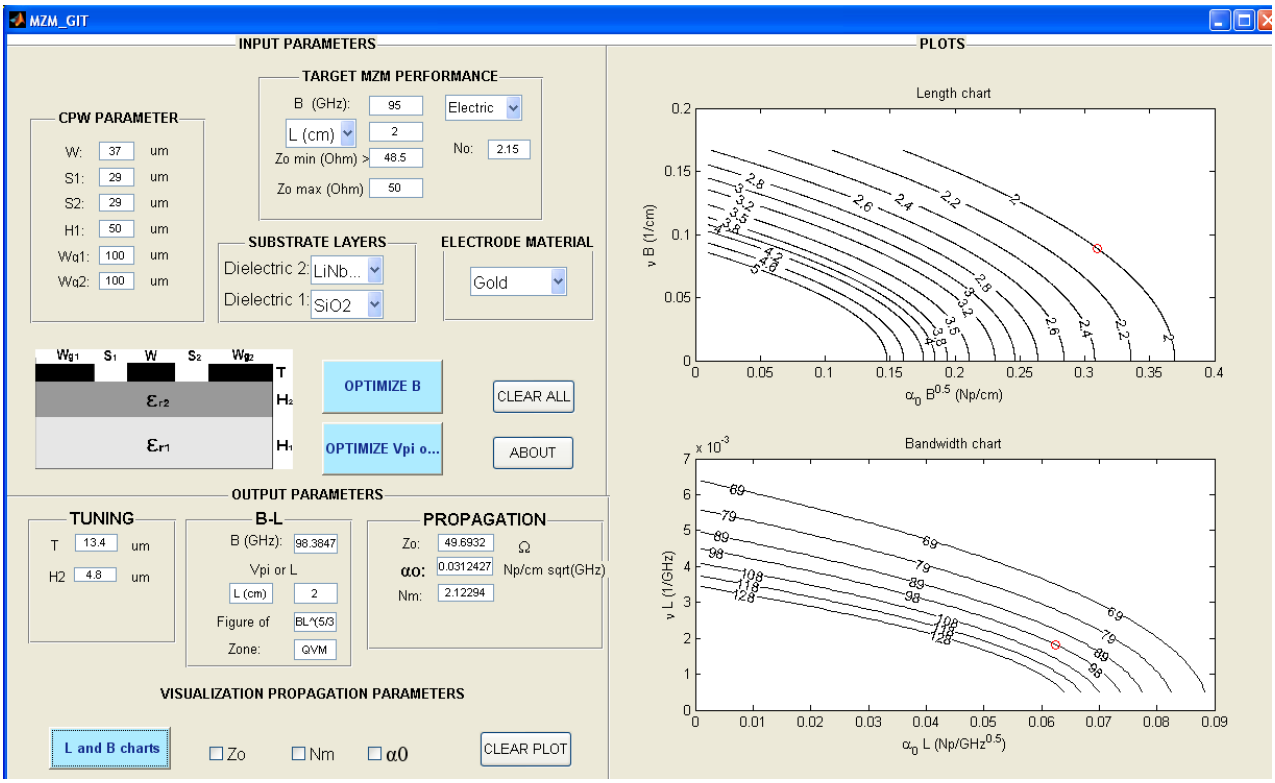

Figure 5.11: MZM-GIT screenshot of the MZM proposal 1.

To find the best horizontal placement of the guide, a plot of the Γ/s versus the guide peak position p is displayed in Fig. (5.11). The Γ/s highest value, calculated using the procedure explained in section 2.3, is 0.0285 obtained for $p = 21.8\mu m$, so we choose to place the center of the guides at this point. The value of V_π is approximately 9 V for phase modulation into each branch which translates into 4.5

V of switching voltage [60]. Table (5.4) lists the characteristics of this MZM proposal.

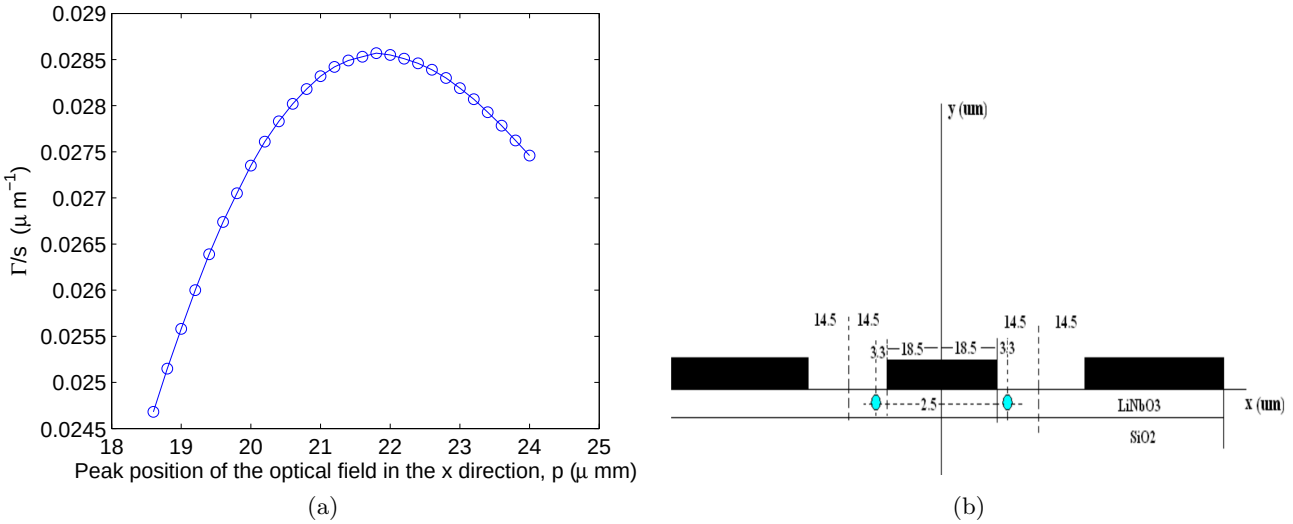

(a) (b)

Figure 5.12: (a) Overlap integral versus peak position of the optical field in the x direction for the MZM proposal 1 with $w_x = w_y = 4\mu m$, (b) position of the optical guide in the CPW.

Table 5.4: Characteristics of the MZM proposal 1.

	Version
L (cm)	2
B (GHz)	98.4
V (V)	4.5
Z_0 (Ω)	49.7 ($DM = 2.26\%$)
$\alpha_0\ dB/cm - \sqrt{GHz}$	0.0312 ($DM = 14\%$)
n_m	2.123 ($DM = 0.83\%$)
w (μm)	37
$s^{\pm}$ (μm)	29
h_1 (μm)	50
t (μm)	13.4
h_2 (μm)	4.8

In the second design, the main effort is devoted to achieving long enough L that combined with the tailoring of the optical guides position, gives a $V_\pi < 2$ V. The B will be fixed to 10 GHz with a Z_0 range between $48.5 - 50\Omega$. The tentative L is calculated through the minimum switching voltage desired, in this case 2 V. First, the fixed CPW parameters are set and the optimal placement of the optical guide in the substrate for these parameters found, as shown in the graphic of Γ/s versus p of Fig. (5.13a). A maximum value of $\Gamma/s \sim 0.0295$ is observed for $p = 23\mu m$. The shift corresponds to a $10\mu m$ from the center of the gap toward the hot electrode, as displayed in Fig. (5.13b). With these

values a minimum $L = 4.3$ cm for a switching voltage of 2 V is necessary.

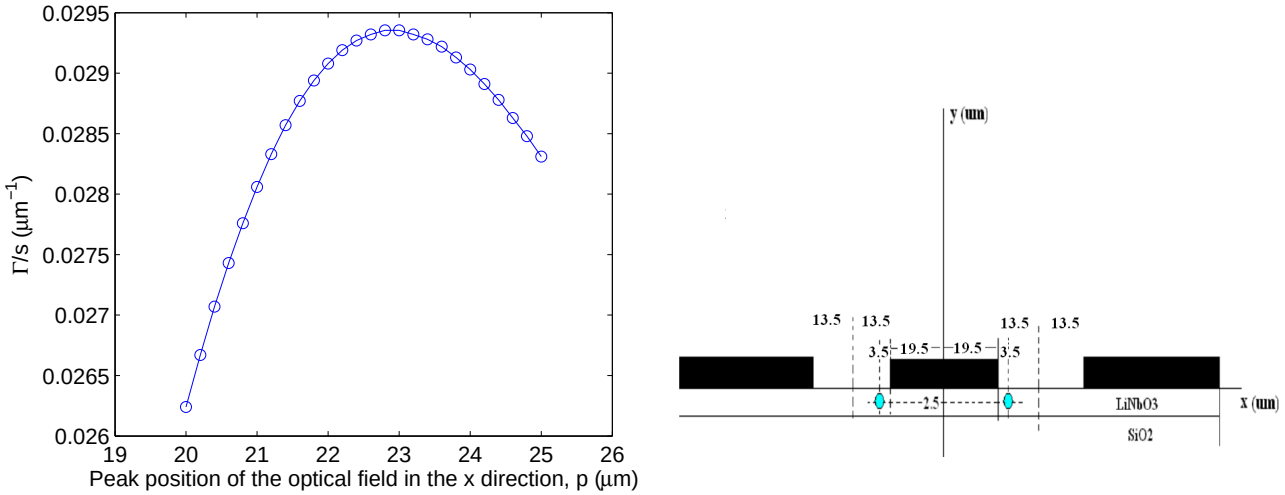

(a) (b)

Figure 5.13: (a) Overlap integral versus peak position of the optical field in the x direction for the MZM proposal 2 with $w_x = w_y = 4\mu m$, (b) position of the optical guide in the CPW.

The tentative value will be set beyond this value to $L = 6$ cm, to guarantee the lowest possible switching voltage. The outcome parameters of the MZM-GIT are displayed in Fig. (5.14). The L is 8.4 cm with a $Z_0 = 49.7\Omega$. The V_π obtained using expression (2.11) is 2 V for each arm, which is translated to a switching voltage of 1 V. Table 5.5 summarizes the parameters of this MZM proposal. The goal of low voltage is achieved, even though an increment in the insertion loss coming from the long TW distance is expected. Small footprint packages with this long L value are possible by using S-shaped bend modulators which have been developed by Doi et. al. in [29], making the chip shorter in about one-fourth.

The two MZM proposals achieved the targets, the first reaches $B \sim 100$ GHz, with $L = 2$ cm, with a switching voltage of 4.5 V. The second one, guarantees a switching voltage of 1 V, for a $B = 10$ GHz, with $L = 8.4$ cm. In both cases almost perfect impedance matched with $Z_0 = 49.7\Omega$ was achieved.

Three other MZM designs are proposed for $B = 20$, $B = 40$ GHz and $B = 65$ GHz, which are common trend values for commercial modulators, and their features are shown in table 5.6. To get the optimal value of Γ, the optical waveguide position has been chosen as in the proposals 1 and 2.

A list of the relevant performance parameters of representative MZM designs as reported by MZM provider companies and also some published research prototypes, together with our proposals, is shown in table 5.7. A more visual comparison in terms of $B - V_\pi$ can be made over Fig. (5.15).

It is observed that our optimized designs are competitive options for the 10, 20, 40 market segments,

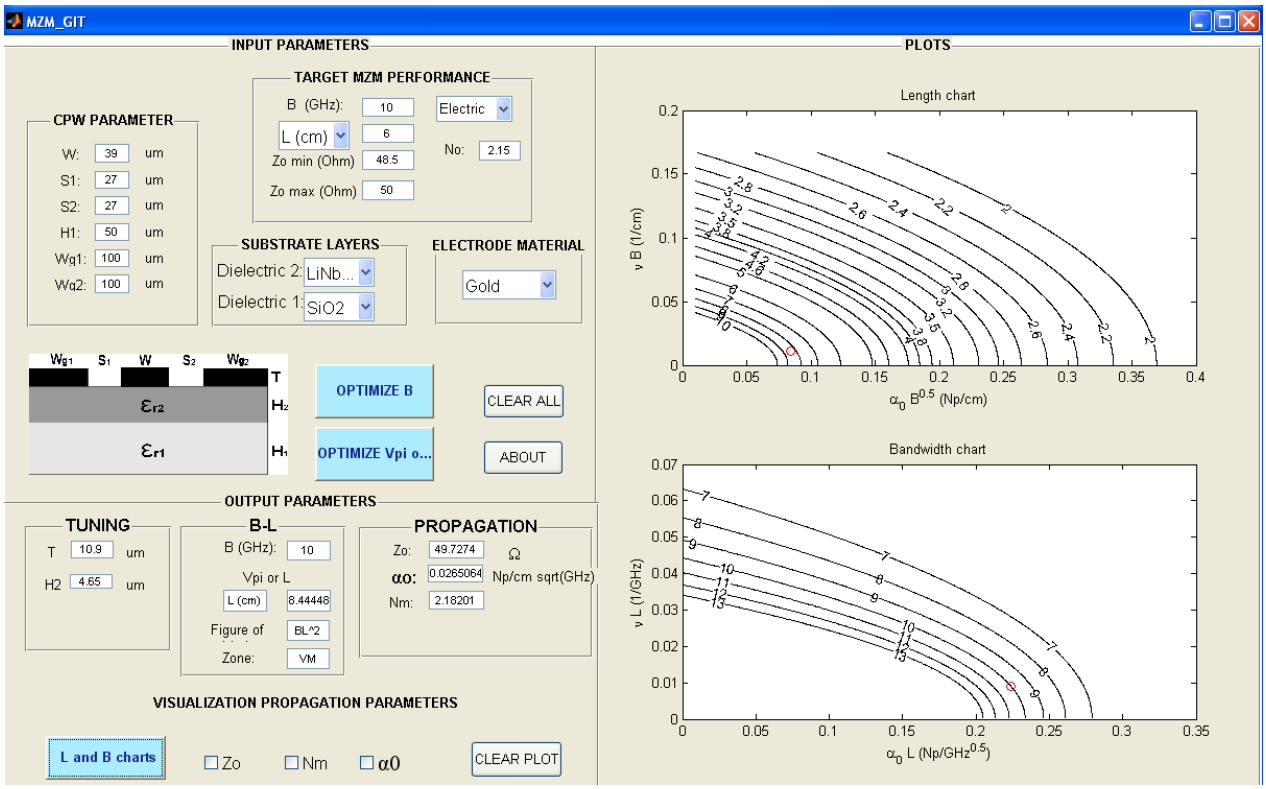

Figure 5.14: MZM-GIT screenshot of the MZM proposal 2.

Table 5.5: Characteristics of the MZM proposal 2.

	Version
L (cm)	8.44
V(V)	1
B (GHz)	10
Z_0 (Ω)	49.7 ($DM = 2.46\%$)
α_0 $dB/cm - \sqrt{GHz}$	0.0265 ($DM = 0.76\%$)
n_m	2.182 ($DM = 0.2\%$)
w (μm)	39
$s^{\pm}$ (μm)	27
h_1 (μm)	50
t (μm)	10.9
h_2 (μm)	4.65

and also for the extremely broadband commercial options available to date ($B \sim 65$ GHz, Gigoptix), featuring low switching V_π values with almost perfect Z_0 matching.

As already discussed, the design methodology object of this Thesis focuses on the electrical transmission structure and therefore performance parameters which typically rely on optimized design of the optical structure such as the insertion loss (IL) or the extinction ratio (ER) have been left out. For comparison purposes, the performance of our designs with regards to those features will be estimated based on reported state-of- the art. The insertion loss has been estimated through a proportionality rule based on the obtained lengths, taking the values of $IL = 9$ dB for $L = 12$ cm for the MZM PSI-3600 (Photonic System). As for ER, we will assume state-of-the art values, around 20 dB.

Table 5.6: Characteristics of the MZM proposals 3, 4 and 5.

	Version 3	Version 4	Version 5
L (cm)	4.31	3.76	2.3
V(V)	1.8	2.2	3.5
B (GHz)	20	40	65
Z_0 (Ω)	49.99	49.63	47.56
$\alpha_0\ dB/cm - \sqrt{GHz}$	0.03161	0.02738	0.03519
n_m	2.214	2.12	2.119
w (μm)	29	28	20
$s^{\pm}$ (μm)	25	32	25
h_1 (μm)	50	50	50
t (μm)	10.9	19.6	17.9
h_2 (μm)	4.5	5.5	4.55

It goes without saying that as relying on a simple analytical model, our proposals need to be taken as just a first-order approach to performance values that could actually be found in practice. They constitute alternatives worth exploring in practical prototypes, where the necessary corrections have to be applied until the optimized final product device can be fabricated. While predicting the dependence among the many parameters involved, our models also provide useful guidelines that aid in the prototype building process. Another great advantage of the combined optimization strategy enabled by our analytical models is that the impact of all the relevant parameters in the overall performance can be simultaneously assessed and the best trade-off found. In this work a preliminary version of a combined optimization strategy based on a simple shooting algorithm has been presented, which has allowed the definition of optimized proposals that constitute competitive alternatives to state-of-the-art MZM designs. More sophisticated algorithms, such as for example a branch-and-bound algorithm [98], could be used to bring performances to their best possible values.

As seen in Fig. (5.15), a record 1 V switching voltage with a 10 GHz B has been predicted (proposal 2 red asterisk) which is 1 V less than the design of [53]. As discussed, to achieve such a low V_π a long ($L = 8.4$ cm) device was required which has lead to an estimated $IL \sim 6.3$ dB, while only 3 dB was reported by [53]. A strong point of our solution is the perfect impedance matching, but unfortunately the Z_0 was not reported in [53]. In [94] they do provide $Z_0 = 38\Omega$ for a 20 GHz with a $V_\pi = 2$ V. Our perfectly matched proposal 3 solution features a slightly lower $V_\pi = 1.8$ V for the same B and lower $IL = 3.2$ dB versus 7 dB in [94]. Still higher $IL = 9$ dB are shown by the PSI 3600 (green rhombus), resulting from a long ($L \sim 12$ cm) device; the bright side is, a extremely low 1 V at 20 GHz. They do not provide Z_0 results either, but in any case, our proposals always show a perfect matching impedance.

Our 40 GHz proposal (4) improves by 0.3 V the V_π featured by the polymer design LX-8220 with higher $IL = 7.5$ dB against only 2.8 dB in our $LiNbO_3$ design. The advantage in V_π vanishes in the 65 GHz device, where both, our proposal 5 and the LX-8901 model achieve 3.5 V. Still losses are lower in the $LiNbO_3$ design, $IL = 1.7$ dB is opposed to a higher $IL = 9$ dB in the Gigoptix model. We haven't been able to gather impedance data for the Gigoptix products either. Lastly, with $B = 98$ GHz our extremely broadband solution stands out for the high B offered with a reasonable $V_\pi = 4.5$ V, low estimated $IL = 1.5$ dB and impedance matched. Of course, in practice, this solution will face a number of challenges related to the high frequency of signals to be dealt with, but we believe it is an alternative which holds promise to extend the B of state-of-the-art MZM.

Table 5.7: Characteristics of the commercial MZM, published research and our proposals.

MZM	Technology	V_π (V)	B(GHz)	$Z_0(\Omega)$	IL (dB)	Opt. RL (dB)	Elec. RL (dB)	ER (dB)
MX-LN-10(Photline)	$LiNbO_3$	4	12	40	2.7	-45	-12	22
MX-LN-20(Photline)	$LiNbO_3$	6.5	20	40	2.7	-45	-12	22
MX-LN-40(Photline)	$LiNbO_3$	6.5	30	35	4	-45	-12	22
LX-8901(Gigoptix)	Polymer	3.5	> 65	-	9	-	-	20
LX-8220(Gigoptix)	Polymer	2.5	40	-	7.5	-	-	20
SD-40(Oclaro)	$LiNbO_3$	5.5	33	-	3.2	-45	-10	20
PSI-3600(Photonic Sys.)	$LiNbO_3$	1	20	-	9	-40		20
[94]	$LiNbO_3$	2	20	38	7	-	-17	25
[53]	$LiNbO_3$	2	10	-	3	-	-	13.5
[45]	$LiNbO_3$	2.8	25	-	5.9	-	-10	25
[91]	$LiNbO_3$	2.4	14	45	7	-	-25	25
[42]	$LiNbO_3$	5.1	70	47	-	-	-30	-
Proposal 1	$LiNbO_3$	4.5	98	49.7	1.5	-	-50	20
Proposal 2	$LiNbO_3$	1	10	49.7	6.3	-	-50	20
Proposal 3	$LiNbO_3$	1.8	20	50	3.2	-	> -50	20
Proposal 4	$LiNbO_3$	2.2	40	49.6	2.8	-	-50	20
Proposal 5	$LiNbO_3$	3.5	65	47.5	1.7	-	-32	20

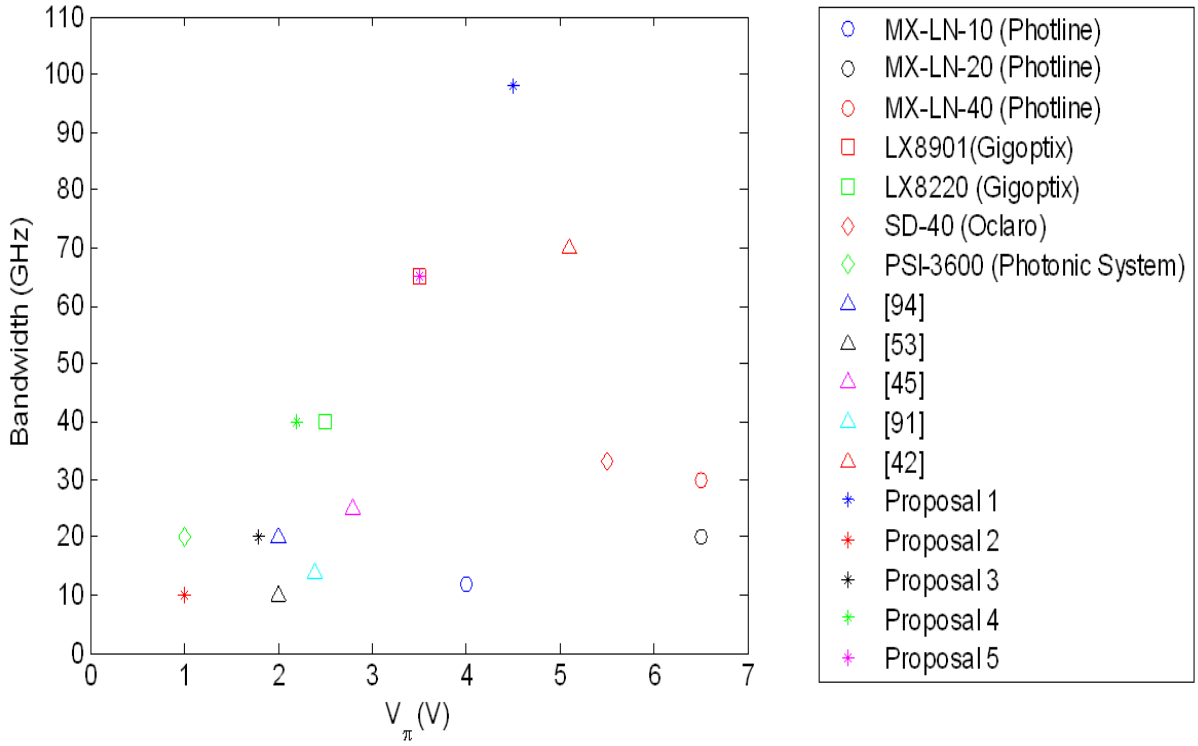

Figure 5.15: Comparison between different MZM performance in terms of B and V_π.

5.5 Summary

In this Chapter a graphic interface tool for the optimization and design of MZM has been presented. This tool allows, entering a tentative $B-L$ and Z_0 performance, and fixing some CPW geometrical parameters, to get the electrode thickness and the dielectric layer thickness of the substrate immediately underneath the electrodes, being it a thin film or a buffer layer. These outputs come from the association of the $B-L$ new expressions developed in Chapter 4, and the novel PP model approach for the CPW propagation parameters. The process of MZM optimization using the MZM-GIT has been illustrated with examples based on published MZM designs representative of an asymmetric gap width, a thin film electro-optical layer and a SiO_2 buffer layer structures. Several optimized MZM proposals have been made exploiting the capabilities of the MZM-GIT yielding competitive performances relative to state-of-the art MZM designs.

The graphic interface thus has shown to be a very useful tool for the optimization and design of

MZM in an easy and accurate form. The flexibility of the PP model allows to include other different CPW geometries and materials. Also it is possible to include in the graphic interface some properties of the optical guides which are determinant for the Γ calculation and thus for V_π minimization.

6

Conclusions and Future Works

This Thesis work has addressed the problem of the systematic design and optimization of electro-optical Traveling Wave (TW) Mach-Zehnder (MZ) modulators based on coplanar waveguides (CPW). The main focus of the research has been on commonplace $LiNbO_3$ electro-optical substrates, but other kinds of electro-optical substrates can easily be included into the analysis. Even though at first sight this may seem a quite mature and established field which has already been pushed to the maximum, we believe that the results of our work allow to conclude that there's still room for improvement if proper balances between all the parameters involved are found.

The main contributions steaming from our work are summarized next:

- A revision of the fundamentals of CPW-MZM modulators has been conducted in which the main involved parameters have been precisely defined and the principal design trade-offs assessed and analyzed with the aid of numerical simulations of the CPW using the finite-element HFSS commercial software tool. The overlap integral value (Γ) definition and impact over the MZM driving voltage (V_π) relation with the TW length (L) has been established. Calculation of Γ through simple and direct numerical estimation techniques based on analytical expressions for the fields in the electro-optical substrate has been validated through HFSS results and measures in literature.

- A review of the many closed-form approaches to obtain the propagation parameters of CPW as a function of the cross-section geometry has been carried out by benchmarking against finite-element HFSS simulated results. The main conclusions of the review are:

1. Conformal approaches (CM) are not suited to electro-optical CPW-TW-MZ modulators (MZM) design and optimization mainly due to poor approximation of thick electrode structures.
2. Empirical approaches such as that reported in [73], allow to extend the range of electrode thicknesses which can be accurately modeled with CM, but still they are not suited to a systematic design of CPW for MZM.
3. The Heinrich formulation [74], yields good accuracy levels and it is appropriate for predicting the performance of CPW-MZM but the formulas are cumbersome, hindering the derivation of intuitive insights, and show little flexibility to changes on the basic CPW geometry such as for example gap width asymmetry and bi-layered substrates.
4. The Frankel [67] and Heinrich [68] high-frequency extensions are effective formulations that allow to accurately extend the quasi-TEM results to the high-frequency range. Due to slightly better performance, the Frankel formulation has been employed throughout this work.

- Novel closed-form expressions to obtain the propagation parameters of CPW as a function of the cross-section geometry in the quasi-TEM range have been derived. The formulas are based on a CM approach and include the effect of electrode thickness by adding the capacitance due to the gap region to the distributed free-space line capacitance. The simplest parallel plate capacitance model has been adopted to approximate this capacitance, and hence the formulation has been dubbed Parallel Plate (PP) formulation. The Wheeler rule has been used to obtain the internal inductance and hence, the resistance values, from the external inductance value. Extensive testing of the PP formulation against HFSS results and against measures reported in literature allows to draw the conclusion that the PP formulation constitutes a extremely useful tool for the systematic design and optimization of CPW-MZM.

- In order to connect the CPW propagation parameters with the MZM system performances (B, L, V_π), the $B-L$ trade-off in MZM has been revisited. Analytical expressions for the trade-off have been available in the limits of velocity matching (VM) and low loss (LL), but in a general case, with arbitrary values of the cross-sectional parameters α and ν, the $B-L$ relation has traditionally been found by numerical solution of a transcendental equation. In this Thesis, novel closed-form formulas explicitly relating B and L have been found through numerical curve fitting of the constant B (L) curves to a second-order polynomial. The formulas are given in a

convenient normalized form which uses the newly defined reference modulator bandwidth and length (B_M, L_M). Besides the known LL and VM regimes, in which defined figures of merit governing the cross-section $B-L$ trade-off already existed, the new $B-L$ formulas have allowed to identify two new intermediate ranges, quasi-low-loss (LL) and quasi-velocity-matching (QVM), in which the figure of merit takes simple forms. A normalized $B-L$ chart has been built which clearly shows the different $B-L$ trade-off ranges of MZM operation and their limits of validity. The newly defined B_M and L_M values have been seen to provide a convenient compact expression for the 4 Figures of Merit as well as a unified way to express their ranges of validity.

- All the systematic design tools developed through the Thesis have been integrated into a software platform in Matlab code, which conveniently and user-friendly allows to tackle the design and optimization problem in MZM by looking for optimized CPW geometries that could satisfy a defined set of performance requirements. Examples of the potential of the tool have been provided based on MZM designs reported in literature. In order to unleash the full potential of the tool a total of 5 different optimized proposals have been described that show competitive performances as compared with state-of-the-art commercial as well as research prototype devices.

As future lines to extend the results of our research of course we envision to work towards prototypes based on the proposals made through the MZM-GIT. On the other hand, even though in its current version the MZM-GIT has allowed to come up with very attractive MZM proposals with impressive performances, it would be useful to extend its capabilities so that sophisticated optimization algorithms beyond the simple shooting method could be employed. Also, more design parameters such as the optimum position and design of optical guides should be included in the automatic MZM optimization. It may even be worth exploring interest of MZM prototype designers in a commercial tool based on the MZM-GIT.

Appendices

A

List of Publications

1. Jose A. Ibarra Fuste, Maria C. Santos Blanco,"Bandwidth-Length Trade-Off Figures of Merit for Electro-Optic Traveling Wave Modulators",*Optics Letters*, Vol. 38, Iss. 9, pp.1548-1550, (2013).

2. Jose A. Ibarra Fuste, Maria C. Santos Blanco, "Closed-form expressions for the optimization of high speed electro-optical modulators",*Optics and Laser Technology*, 49, 296-300, (2013).

3. J.A Ibarra Fuste, M. C. Santos Blanco, E. Rodriguez Rodriguez,"Compact Closed-Form Expressions for the Propagation Parameters of a Finite Ground Width CPW with Thick Electrodes",*IET Microw. Antennas & Propag.*, Vol. 6, No. 3, pp 269-275,(2012).

B

MZM frequency response

The traveling RF voltage along each arm can be written as

$$V(t,z) = V_0 e^{[j(2\pi f t - \beta z) - \alpha_0 \sqrt{f} z]}, \tag{B.1}$$

where β is the propagation constant and α_0 is the field attenuation coefficient given in Nepers per unit length at 1 Ghz.

The voltage for photons incident at $t = t_0$, for a frame of reference moving with the photon's velocity

$$V(t,z) = V_0 e^{\left[j\left(\omega t - z\left(\frac{\omega}{v_m} - \frac{\omega}{v_o}\right)\right) - \alpha_0 \sqrt{f} z\right]}, \tag{B.2}$$

$$V(z) = V_0 e^{[j\omega(t - z\nu) - \alpha_0 \sqrt{f} z]}, \tag{B.3}$$

where v_m is the microwave group velocity, v_o is the optical group velocity, $\nu = (n_m - n_{opt})/c$, being n_m the microwave index, n_{opt} the optical index and c the speed of light in vacuum.

The total electro-optically induced phase shift

$$\Delta\phi(t_0) = \frac{\pi}{\lambda_0} n_{opt}^3 r_{33} \frac{\Gamma}{s} \int_0^L V(z, t_0) dz, \tag{B.4}$$

where r_{33} is the optical axis electrooptical coefficient, Γ is the overlap integral, s the CPW electrodes gap, λ is the wavelength, obtaining [99]

$$\Delta\phi = \left(\frac{\pi n_{opt}^3 r_{33} V_0 \Gamma}{s\lambda}\right) \sqrt{\frac{1 + e^{-2\alpha L} - 2e^{-\alpha L}\cos(\omega\nu L)}{(\alpha L)^2 + (\omega\nu L)^2}}, \tag{B.5}$$

using the property $\cos(2x) = 1 - 2\sin^2(x)$,

$$\Delta\phi = \left(\frac{\pi n_{opt}^3 r_{33} V_0 \Gamma}{s\lambda}\right) \sqrt{\frac{1 + e^{-2\alpha L} - 2e^{-\alpha L}(1 - 2\sin^2(\pi f \nu L))}{(\alpha L)^2 + (\omega \nu L)^2}}, \tag{B.6}$$

$$\Delta\phi = \left(\frac{\pi n_{opt}^3 r_{33} V_0 \Gamma}{s\lambda}\right) \sqrt{\frac{e^{-\alpha L}[e^{\alpha L} - e^{-\alpha L} - 2 + 4\sin^2(\pi f \nu L)]}{(\alpha L)^2 + (\omega \nu L)^2}}. \tag{B.7}$$

As

$$\sinh^2\left(\frac{\alpha L}{2}\right) = \left(\frac{e^{\frac{\alpha L}{2}} - e^{\frac{-\alpha L}{2}}}{2}\right)^2 = \frac{e^{\alpha L} - e^{-\alpha L} - 2}{4}, \tag{B.8}$$

therefore

$$4\sinh^2\left(\frac{\alpha L}{2}\right) = e^{\alpha L} - e^{-\alpha L} - 2. \tag{B.9}$$

Substituting in (B.7),

$$\Delta\phi = \frac{V_0 \pi}{V_\pi} e^{-\left(\frac{\alpha L}{2}\right)} \sqrt{\frac{\sinh^2(\frac{\alpha L}{2}) + \sin^2(\pi f \nu L)}{\left(\frac{\alpha L}{2}\right)^2 + (\pi f \nu L)^2}}. \tag{B.10}$$

The frequency response will be the total phase shift resulting from a microwave voltage applied

$$M(f) = e^{-\left(\frac{\alpha_0 \sqrt{f} L}{2}\right)} \sqrt{\frac{\sinh^2(\frac{\alpha_0 \sqrt{f} L}{2}) + \sin^2(\pi f \nu L)}{\left(\frac{\alpha_0 \sqrt{f} L}{2}\right)^2 + (\pi f \nu L)^2}}. \tag{B.11}$$

C

CPW quasi-TEM model

C.1 Characteristic Impedance

The well known Maxwell's equation are given by [100]

$$\nabla \cdot \vec{D} = \rho, \tag{C.1}$$

$$\nabla \cdot \vec{B} = 0, \tag{C.2}$$

$$\nabla \times \vec{E} = -\frac{\partial \vec{B}}{\partial t}, \tag{C.3}$$

$$\nabla \times \vec{H} = \vec{J} + \frac{\partial \vec{D}}{\partial t}, \tag{C.4}$$

where,

$\vec{E}$ - is the electric field created by charges.

$\vec{D}$ - is the electric flux density or electric induction.

$\vec{B}$ - is the magnetic flux density or magnetic induction.

$\vec{H}$ - is the magnetic field.

ρ - is the total charge density.

$\vec{J}$ - is the current density.

Applying divergence to (C.4) and combining it with (C.1)

$$\nabla\cdot(\nabla\times\vec{H}) = \nabla\cdot\left(\vec{J}+\frac{\partial\vec{D}}{\partial t}\right) = \nabla\cdot\vec{J}+\frac{\partial}{\partial t}(\nabla\cdot\vec{D}).$$

Taking to account that $\nabla\cdot(\nabla\times\vec{H}) = 0$

$$\nabla\cdot\vec{J} = -\frac{\partial\rho}{\partial t}. \tag{C.5}$$

The equation obtained is the charge conservation equation, that in simple words means that the current flowing in or out of a surface is equal to the charge gain or loss of the volume representing this surface respectively. The current density is related to the electric current as

$$\vec{I} = \vec{J}\cdot A, \tag{C.6}$$

where A is the area where current flows.

The electric current is the rate as electric charge change in a surface

$$I = \frac{\partial q}{\partial t}. \tag{C.7}$$

All these yield to the Kirchhoff's current law, establishing that the current flowing into a node is equal at the current flowing out of this node.

A circuit equivalent diagram of a transmission line is analyzed, as is represented in Fig. C.1. It can be represented as an infinite models of infinitesimally short segments of size z of a transmission line formed by primary elements R, L, G, C, where,

R- is the resistance per unit of length (Ω/m).
L- is the inductance per unit of length (H/m).
G- is the conductance per unit of length (S/m).
C- is the capacitance per unit of length (F/m).

The variation of current within the infinitesimal cell is given by the current flowing through the capacitance and conductance. The capacitance is define as the ratio of charge between conductors to the voltage between them, that is, $C = q/V$, or what is the same, $q = CV$.

The current trough the capacitor is given by

$$I = \frac{\partial q}{\partial t} = C\frac{\partial V}{\partial t}. \tag{C.8}$$

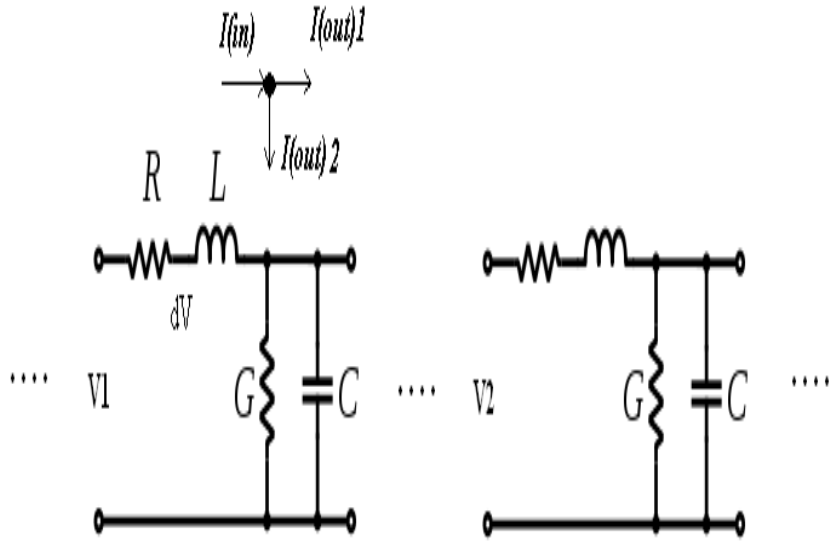

Figure C.1: Equivalent diagram of a transmission line.

The conductance due the dielectric material is represented as a shunt resistance between conductor and is

$$G = \frac{1}{R}, \tag{C.9}$$

using Ohm's law, the current due conductance

$$I = GV. \tag{C.10}$$

Applying Kirchhoff's current law,

$$\frac{\partial I}{\partial z} = -\left(GV + C\frac{\partial V}{\partial t}\right). \tag{C.11}$$

In the same way we can use the Kirchhoff's law of voltages derived from the conservation energy equation, establishing that the sum of the voltage in any closed loop is equivalent to the sum of the voltage drops in that loop. Realizing that the voltage dropped in the quadrapole of Fig. C.1 are the tensions dropped in the inductance and resistance, we get,

$$\frac{\partial V}{\partial z} = -\left(RI + L\frac{\partial I}{\partial t}\right). \tag{C.12}$$

Deriving expression (C.12)

$$\frac{\partial^2 V}{\partial z^2} = -\left[R\frac{\partial I}{\partial z} + L\frac{\partial}{\partial t}\left(\frac{\partial I}{\partial z}\right)\right]. \tag{C.13}$$

Using (C.11) in (C.13)

$$\frac{\partial^2 V}{\partial z^2} = RGV + (RC + LG)\frac{\partial V}{\partial t} + LC\frac{\partial^2 V}{\partial t^2}. \tag{C.14}$$

In the same way,

$$\frac{\partial^2 I}{\partial z^2} = RGI + (RC + LG)\frac{\partial I}{\partial t} + LC\frac{\partial^2 I}{\partial t^2}. \tag{C.15}$$

Writing (C.14) in a phasor form (frequency domain),

$$\frac{\partial^2 V}{\partial z^2} = RGV + (RC + LG)j\omega V - \omega^2 LCV,$$

$$\frac{\partial^2 V}{\partial z^2} = (R + j\omega L)(G + j\omega C)V. \tag{C.16}$$

Solution of (C.16) is given by

$$V(z) = V_1 e^{-\gamma z} + V_2 e^{\gamma z}, \tag{C.17}$$

being

$$\gamma = \sqrt{(R + j\omega L)(G + j\omega C)}, \tag{C.18}$$

the propagation constant, also given by $\gamma = \alpha + j\beta$.

Using equation (C.12) in phasor terms, we can get the current

$$I = -\frac{\frac{\partial V}{\partial z}}{R + j\omega L}. \tag{C.19}$$

As

$$\frac{\partial V}{\partial z} = V_1\frac{\partial}{\partial z}[e^{-\gamma z}] + V_2\frac{\partial}{\partial z}[e^{\gamma z}],$$

$$\frac{\partial V}{\partial z} = \gamma[V_1 e^{-\gamma z} + V_2 e^{\gamma z}] = \gamma V(z). \tag{C.20}$$

Combining (C.19) y (C.20)

$$I = \sqrt{\frac{G + j\omega C}{R + j\omega L}} V. \tag{C.21}$$

Applying Ohm's law, the equation of characteristic impedance in terms of the line parameters is given by

$$Z_0 = \sqrt{\frac{R + j\omega L}{G + j\omega C}}. \tag{C.22}$$

For the lossless line ($R = G = 0$), or for high frequency cases ($R << j\omega L$ and $G << j\omega C$), equation (C.22) reduces to

$$Z_0 = \sqrt{\frac{L}{C}}. \tag{C.23}$$

C.2 Attenuation

We can get the attenuation using equation (C.18)

$$\alpha + j\beta = \sqrt{(R + j\omega L)(G + j\omega C)}.$$

Doing some math inside the square root

$$\alpha + j\beta = [RG - \omega^2 LC + j\omega(CR + LG)]^{\frac{1}{2}}. \tag{C.24}$$

The term RG of (C.24) may be neglected because for low loss line $R << \omega L$ and $G << \omega C$, and using the property of binomial expansions [101]

$$\alpha + j\beta \simeq (-\omega^2 LC)^{1/2} + \frac{1}{2}(-\omega^2 LC)^{-\frac{1}{2}}[j\omega(CR + LG)] - \frac{1}{8}(-\omega^2 LC)^{\frac{1}{2}-1}[j\omega(CR + LG)]^2.$$

Neglecting second order terms and so on, we get

$$\alpha + j\beta \simeq j\omega\sqrt{LC} + \frac{1}{2}\sqrt{LC}\left(\frac{R}{L} + \frac{G}{C}\right),$$

and finally

$$\alpha \simeq \frac{1}{2}\left(\frac{R}{Z_0} + GZ_0\right), \tag{C.25}$$

$$\beta = \omega\sqrt{LC}. \tag{C.26}$$

C.3 Effective dielectric constant

The dielectric constant ε_r of a material is the ratio of its permittivity ε to the permittivity of vacuum ε_0, so $\varepsilon_r = \frac{\varepsilon}{\varepsilon_0}$. The dielectric constant is therefore also known as the relative permittivity of the material. Since the dielectric constant is just a ratio of two similar quantities, it is dimensionless.

The refractive index of a medium is the ratio of the speed of light in vacuum to the phase velocity of the propagation wave through this medium, and is given by

$$n = \sqrt{c}v_p = \sqrt{\frac{\varepsilon}{\varepsilon_0}}, \tag{C.27}$$

with $v_p = \frac{\omega}{\beta}$, where β is the phase constant given by (C.26). From (C.26) and (C.27) is easy to establish,

$$\varepsilon_r = c^2 LC. \tag{C.28}$$

D

Extension formulas for high frequency dispersion in CPW

The empirical formula of Frankel et. al. in [67] was derived through the fitting of full-wave simulation results and is given by

$$\sqrt{\varepsilon_{eff}} = \sqrt{\varepsilon_q} + \frac{\sqrt{\varepsilon_r} - \sqrt{\varepsilon_q}}{\left(1 + a\left(\frac{f}{f_{TE}}\right)^{-1.8}\right)}. \tag{D.1}$$

Here ε_q is the quasi-static effective permittivity and $f_{TE} = c/(4h_1\sqrt{\varepsilon_r - 1})$ is the surface wave TE_1 mode cutoff frequency, ε_r is the relative permittivity of the substrate material, and c is the speed of light in vacuum. The parameter a is related to the transmission line geometry as

$$\ln(a) = u\ln(w/s + v), \tag{D.2}$$

where,

$$u = 0.54 - 0.64q + 0.015q^2, \tag{D.3}$$

$$v = 0.43 - 0.86q + 0.54q^2, \tag{D.4}$$

$$q = \ln(w/h). \tag{D.5}$$

Schnieder et al. [68] also provided an expression to account for high frequency dispersion. In this approach a frequency-domain finite-difference method is used as a reference to fit the analytical

expression. The investigation reveals that ε_{eff} depends only on the ratio d/w_{tot}, ($w_{tot} = w + 2s + 2w$), and on frequency f being normalized to f_g, which is the frequency where the phase constants of the CPW mode and the first lateral higher order mode intersect

$$f_g = \frac{2}{w_{tot}\sqrt{2\mu_0\varepsilon_0(\varepsilon_r - 1)}}, \tag{D.6}$$

where $\varepsilon_q = \frac{\varepsilon r+1}{2}$.

Thus, the CPW high-frequency dispersion can be described by the following formula, with ε_{eff} being the quasi-static value

$$\varepsilon_{eff_{final}} = \varepsilon_{eff}\left[1 + \left(\sqrt{\frac{\varepsilon_r}{\varepsilon_q}}p\left(\frac{f}{f_g}\right)^2\right)\right], \tag{D.7}$$

where p is a fitting parameter to a full-wave simulation given by

$$p = \frac{2.86465\left(\frac{d}{w_{tot}}\right)^2}{0.15075 + \frac{d}{w_{tot}}}. \tag{D.8}$$

E

Internal inductance equation

The analysis starts from expression

$$L_{int}^{t} = \frac{\delta}{2\varepsilon_0 c^2 (2A_0 + \frac{t}{s})^2} \left[\frac{t}{s^2} - 2\frac{\partial A_0}{\partial w} - 2\frac{\partial A_0}{\partial s} + \frac{1}{s}. \right] \tag{E.1}$$

Rewriting the approximation for the elliptic integrals A_i of [77]

$$Ai = \frac{K(k_i)}{K(k_i')} = \left\{ \begin{array}{ll} \frac{\pi}{2\ln(\frac{4}{k_i})}; & \text{for } 0 < k_0 < 10^{-5} \\ \\ \frac{\pi}{\ln(4\frac{1+k_i'}{1-k_i'})}; & \text{for } 10^{-5} \leq k_0 < \frac{1}{\sqrt{2}} \\ \\ \frac{1}{4}\ln(4\frac{1+k_i}{1-k_i}); & \text{for } k_0 \geq \frac{1}{\sqrt{2}} \end{array} \right\}. \tag{E.2}$$

For the interval $0 < k_0 < 10^{-5}$, doing $y = ln\frac{4}{k_0}$

$$\frac{\partial A_0}{\partial s} = \frac{\pi}{2}\frac{\partial (1/y)}{\partial s} = \frac{\pi}{2k_0 y^2}\frac{\partial k_0}{\partial s} = \frac{2A_0^2}{\pi k_0}\frac{\partial k_0}{\partial s}. \tag{E.3}$$

Similarly

$$\frac{\partial A_0}{\partial w} = \frac{\pi}{2k_0 y^2}\frac{\partial k_0}{\partial w} = \frac{2A_0^2}{\pi k_0}\frac{\partial k_0}{\partial w}. \tag{E.4}$$

Solving the derivatives

$$\frac{\partial k_0}{\partial w} = k_0 \left[\frac{2s}{w(w+2s)} + \frac{1}{2(w+2s+w_g)} - \frac{1}{2(w+s+w_g)} \right], \tag{E.5}$$

$$\frac{\partial k_0}{\partial s} = k_0 \left[-\frac{2}{w+2s} + \frac{1}{w+2s+w_g} - \frac{1}{2(s+w_g)} - \frac{1}{2(s+w+w_g)} \right]. \tag{E.6}$$

Finally we get

$$\begin{aligned} L_{int} &= \frac{\delta}{2\varepsilon_0 c^2 \left(2A_0 + \frac{t}{s}\right)^2} \times \\ &\left[\frac{4A_0^2}{\pi} \left(\frac{2}{w+2s} \left(\frac{s}{w} + 1 \right) - \frac{1}{2(w+2s+w_g)} + \frac{1}{2(s+w_g)} \right) + \frac{1}{s} \left(\frac{t}{s} + 1 \right) \right]. \end{aligned}$$

For the interval $10^{-5} \leq k_0 < \frac{1}{\sqrt{2}}$, doing $y = ln\left(4\frac{1+k_o^{'}}{1-k_0^{'}}\right)$

$$\begin{aligned} \frac{\partial A_0}{\partial s} &= -\frac{\pi}{y^2}\frac{\partial y}{\partial s} = -\frac{\pi}{y^2}\frac{\partial [ln(4) + ln(1+k_0^{'}) - ln(1-k_0^{'})]}{\partial s} \\ &= -\frac{\pi}{y^2}\left[\frac{\frac{\partial (1+k_0^{'})}{\partial s}}{1+k_0^{'}} - \frac{\frac{\partial (1-k_0^{'})}{\partial s}}{1-k_0^{'}} \right] = -\frac{\pi}{y^2}\frac{\partial k_0^{'}}{\partial s}\left(\frac{1}{1+k_0^{'}} + \frac{1}{1-k_0^{'}} \right) \\ &= -\frac{\pi}{y^2\left(1-(k_0^{'})^2\right)}\frac{\partial k_0^{'}}{\partial s} = -\frac{2A_0^2}{\pi\left(1-(k_0^{'})^2\right)}\frac{\partial k_0^{'}}{\partial s}, \end{aligned}$$

and

$$\frac{\partial k_0^{'}}{\partial s} = \frac{\frac{\partial (1-k_0^2)}{\partial s}}{2\sqrt{1-k_0^2}} = -\frac{k_0}{k_0^{'}}\frac{\partial k_0}{\partial s}. \tag{E.7}$$

We get

$$\frac{\partial A_0}{\partial s} = \frac{2A_0^2}{\pi\left(1-(k_0^{'})^2\right)}\frac{k_0}{k_0^{'}}\frac{\partial k_0}{\partial s} = \frac{2A_0^2}{\pi k_0^2}\frac{k_0}{k_0^{'}}\frac{\partial k_0}{\partial s} = \frac{2A_0^2}{\pi k_0 k_0^{'}}\frac{\partial k_0}{\partial s}. \tag{E.8}$$

Similarly

$$\frac{\partial A_0}{\partial w} = \frac{2A_0^2}{\pi k_0 k_0^{'}}\frac{\partial k_0}{\partial w}.$$

Finally we get for this interval

$$\begin{aligned} L_{int} &= \frac{\delta}{2\varepsilon_0 c^2 \left(2A_0 + \frac{t}{s}\right)^2} \times \\ &\left[\frac{4A_0^2}{\pi k_0^{'}} \left(\frac{2}{w+2s} \left(\frac{s}{w} + 1 \right) - \frac{1}{2(w+2s+w_g)} + \frac{1}{2(s+w_g)} \right) + \frac{1}{s} \left(\frac{t}{s} + 1 \right) \right]. \end{aligned}$$

For the interval $k_0 \geq \frac{1}{\sqrt{2}}$

$$\begin{aligned}\frac{\partial A_0}{\partial s} &= \frac{1}{\pi}\frac{\partial[ln(4)+ln(1+k_0)-ln(1-k_0)]}{\partial s} = \frac{1}{\pi}\left[\frac{1}{1+k_0}+\frac{1}{1-k_0}\right]\frac{\partial k_0}{\partial s} \\ &= \frac{2}{\pi[1-(k_0^2)]}\frac{\partial k_0}{\partial s} = \frac{2}{\pi(k_0')^2}\frac{\partial k_0}{\partial s},\end{aligned}$$

similarly

$$\frac{\partial A_0}{\partial w} = \frac{2}{\pi(1-k_0^2)}\frac{\partial k_0}{\partial w} = \frac{2}{\pi(k_0')^2}\frac{\partial k_0}{\partial w}.$$

Finally for this interval

$$\begin{aligned}L_{int} &= \frac{\delta}{2\varepsilon_0 c^2\left(2A_0+\frac{t}{s}\right)^2}\times \\ &\quad \left[\frac{4}{\pi(k_0')^2}\left(\frac{2}{w+2s}\left(\frac{s}{w}+1\right)-\frac{1}{2(w+2s+w_g)}+\frac{1}{2(s+w_g)}\right)+\frac{1}{s}\left(\frac{t}{s}+1\right)\right].\end{aligned}$$

F

CPW B-L expression

As observed in Fig. 4.3 the curves follow a parabolic pattern, with axes intersection in $(0, \frac{k_\nu}{BL})$, $(\frac{\sqrt{k_\alpha}}{\sqrt{BL}}, 0)$ and $(0, \frac{-k_\nu}{BL})$, this last one in the imaginary axis. Replacing the points in the parabola equation $(ay^2 + by + c)$, a three equation system is obtained

$$0 = a\left(\frac{k_\nu}{BL}\right)^2 + b\frac{k_\nu}{BL} + c, \tag{F.1}$$

$$0 = a\left(-\frac{k_\nu}{BL}\right)^2 - b\frac{k_\nu}{BL} + c, \tag{F.2}$$

$$\frac{\sqrt{k_\alpha}}{\sqrt{BL}} = c. \tag{F.3}$$

Clearing the unknown a

$$a = -c\left(\frac{BL}{k_\nu}\right)^2 = -\frac{\sqrt{k_\alpha}}{k_\nu^2}B^{1.5}L, \tag{F.4}$$

and the unknown $b = 0$.

These lead to the curve expression given by

$$\alpha_0 = -\frac{\sqrt{k_\alpha}}{k_\nu^2}B^{3/2}L\nu^2 + \frac{\sqrt{k_\alpha}}{\sqrt{BL}}. \tag{F.5}$$

Rearranging the equation, finally we get

$$B^2L^2 + \frac{k_\nu^2}{\sqrt{k_\alpha}}\frac{\alpha_0}{\nu^2}\sqrt{BL} = \frac{k_\nu^2}{\nu^2}. \tag{F.6}$$

This expression allows to relate all the key parameters of the modulator, and we can get L and B solving this quadratic expression, obtaining,

$$L = \frac{1}{2}\frac{k_\nu^2}{\sqrt{k_\alpha}}\frac{\alpha_0}{\nu^2}\frac{1}{B^{1.5}}\left[\sqrt{(2\frac{\sqrt{k_\alpha}}{k_\nu}\frac{\nu}{\alpha_0}\sqrt{B})^2+1}-1\right], \tag{F.7}$$

$$B = 2^{-4/3}T\left(\frac{k_\nu^2}{\sqrt{k_\alpha}}\frac{\alpha_0}{\nu^2}\frac{1}{L}\right)^{2/3}\left[1-\sqrt{T^{-3/2}-1}\right]^2, \tag{F.8}$$

where,

$$T = \frac{1}{2}W^{-1/3}(S^{1/3}-S^{-1/3}), \tag{F.9}$$

$$S = W+\sqrt{1+W^2}, \tag{F.10}$$

$$W = \frac{3^{3/2}}{2^4}\left(\frac{k_\nu}{k_\alpha}\frac{\alpha_0^2}{\nu}L\right). \tag{F.11}$$

G

Shooting method optimization parameters

The limits of the shooting method optimization parameters used in the MZM GIT were:

- $\alpha_{0_{min}} = 0.001 Np/cm - \sqrt{GHz}$; $\alpha_{0_{max}} = 0.1 Np/cm - \sqrt{GHz}$; step=0.001 Np/cm
- $\nu_{min} = 0.001$ ns/cm; $\nu_{max} = 0.05$ ns/cm; step=0.001 ns/cm
- $t_{min} = 2\mu m$; $t_{max} = 40\mu m$; step=0.01 μm
- $h_{2_{min}} = 0.1\mu m$; $h_{2_{max}} = 2\mu m$, for SiO_2 buffer layer; step=0.01 μm
- $h_{2_{min}} = 4.5\mu m$; $h_{2_{max}} = 10\mu m$, for $LiNbO_3$ thin film; step=0.01 μm

List of Figures

List of Tables

Acronyms

$BaTiO_3$	barium titanate
CPW	coplanar waveguide
CM	conformal mapping
DPSK	differential phase shift keying modulation
DM	discrepancy margin
dB	decibel
EO	electro-optic
FEM	finite element method
GaAs	gallium arsenide
GCPW	grounded coplanar waveguide
Ge	germanium
HFSS	high frequency structural simulator
IC	integrated circuit
IM/DD	intensity modulation and direct detection
LL	low-loss
$LiNbO_3$	lithium niobate
MZM	Mach Zehnder modulator
MZM-GIT	Mach Zehnder modulator graphic interface tool
PC	partial capacitance
PP	parallel plate
QLL	quasi low-loss
QVM	quasi velocity matching
RF	radio frequency

SiO_2	silicon dioxide
TE	transverse electric
TM	transverse magnetic
TEM	transverse electro-magnetic
TW	traveling wave
VM	velocity matching

Symbols & Notations

Roman Symbols

A_i	approximation for the elliptic integral
B	bandwidth (Hz)
B^e	electrical bandwidth (Hz)
B^o	optical bandwidth (Hz)
c	speed of light in free space (m/s)
C	capacitance per unit length (F/m)
C_0	free space capacitance (F)
C_s	dielectric capacitance (F)
C_0'	free-space partial capacitance (F)
C_g	gap capacitance (F)
d	distance (m)
$\vec{D}$	electric displacement vector (C/m^2)
E	electric field (V/m)
E_{opt}	optical field (V/m)
E_m	microwave field (V/m)
$\vec{E}$	electric field vector (V/m)
f	frequency (Hz)
f_g	normalized frequency (Hz)
G	conductance per unit length (S/m)
H	magnetic field (A/m)
I	current (A)

h	total substrates height of a coplanar waveguide (m)
h_1	bottom substrate height of a coplanar waveguide (m)
h_2	upper substrate height of a coplanar waveguide (m)
J	current density (A/m^2)
j	$\sqrt{-1}$
k_0	free-space wavenumber (m^{-1})
$K(k)$	complete elliptic integral of the first kind
L	inductance per unit length (H/m); also length (m)
L_{int}	internal inductance (H)
L_{out}	external inductance (H)
$M(f)$	small-signal modulation response
n_0	ordinary refractive index
n_e	extraordinary refractive index
n_m	microwave refractive index
n_{opt}	optical refractive index
$n(E)$	refractive index as a function of the electric field
n_x	refractive index in the x direction
n_y	refractive index in the y direction
n_z	refractive index in the z direction
p	peak position of the optical field in the lateral direction (m)
r	Pockel coefficient (m/V)
R	resistance per unit length (Ω/m)
s	Kerr coefficient (m^2/V^2); also gap width between electrodes of a coplanar waveguide (m)
t	electrode thickness of a coplanar waveguide (m)
$tan\delta$	dielectric loss tangent
V	voltage (V)
V_π	half-wave voltage (V)
v_m	microwave group velocity
v_o	optical group velocity
w	hot electrode width of a coplanar waveguide (m)
w_g	ground electrode width of a coplanar waveguide (m)

w_{tot}	coplanar waveguide total width (m)
w_x	width parameters indicating how rapidly the field decays from its maximum value in x (m)
w_y	width parameters indicating how rapidly the field decays from its maximum value in y (m)
x	horizontal position (m)
y	vertical position (m)
z_i	vector normal to wall i
Z_0	characteristic impedance (Ω)

Greek Symbols

α	field attenuation coefficient (Np/cm)
α_0	frequency dependent attenuation loss ($Np/cm\sqrt{f}$)
δ	skin depth (m)
ν	velocity mismatch parameter (s/m)
β	propagation constant (m^{-1})
η	impermeability tensor
η_{ij}	components of the impermeability tensor
ε_0	electric permittivity of free space (F/m)
ε_q	quasi-static effective permittivity (F/m)
ε_{eff}	effective permittivity (F/m)
ε_r	relative permittivity
ϵ_i	component of the electric permittivity tensor (F/m)
μ_0	magnetic permeability of free space (H/m)
μ	magnetic permeability (H/m)
μ_i	magnetic permeability of dielectric i (H/m)
ϕ	phase shift (m^{-1})
σ	conductivity (S/m)
Γ	overlap integral
λ_0	free-space wavelength (m)
ω	angular frequency (rad/s)

Bibliography

[1] T. Kitazawa, D. Polifko, and H. Ogawa, "Analysis of CPW for LiNbO3 optical modulator by extended spectral-domain approach," *IEEE Micro and Guided Wave Letters*, vol. 2, No. 8, pp. 313–315, 1992. [cited at p. ii, 43, 44, 115, 117]

[2] L. Gheorma, P. Savi, and R. M. O. Jr., "Thin layer design of X-Cut LiNbO3 modulators," *IEEE Phot. Tech. Lett*, vol. 12, No. 12, pp. 1618–1620, 2000. [cited at p. ii, 4, 46, 47, 115, 117]

[3] M. Liu, X. Yin, E. Ulin-Avila, B. Geng, T. Zentgraf, L. Ju, F. Wang, and X. Zhang, "A graphene-based broadband optical modulator," *Nature*, vol. 474, pp. 64–67, 2011. [cited at p. 1]

[4] J. Gosciniak and D. T. H. Tan, "Theoretical investigation of graphene-based photonic modulators," *Scientific Reports*, pp. 1–6, 2013, Article number: 1897. [cited at p. 1]

[5] B. Sensale-Rodriguez, S. Rafique, R. Yan, M. Zhu, V. Protasenko, D. Jena, L. Liu, and H.G.Xing, "Terahertz imaging employing graphene modulator arrays," *Optics Express*, vol. 21, No. 2, pp. 2324–2330, 2013. [cited at p. 1]

[6] A. E. Willner and S. R. Nuccio, "Electro-optic polymer modulators," in *Optical Fiber Communication Conference and Exposition (OFC/NFOEC), 2012 and the National Fiber Optic Engineers Conference*, 2012. [cited at p. 1]

[7] D. Chena, H. R. Fetterman, A. Chen, W. H. Steier, L. R. Dalton, W. Wang, and Y. Shi, "Demonstration of 110 GHz electro-optic polymer modulators," *Appl. Phys. Lett*, vol. 70, No. 25, pp. 3335–3337, 1997. [cited at p. 1]

[8] S. Hyun-Chae, O. Min-Cheol, A. Seh-Won, W. H. Steier, H. R. Fetterman, and C. Zhang, "Flexible low-voltage electro-optic polymer modulators," *Appl. Phys. Lett*, vol. 82, Issue 25, pp. 4432–4434, 2003. [cited at p. 1]

[9] P.Tang, D. J. Towner, T. Hamano, and A. L. Meier, "Electrooptic modulation up to 40 GHz in a barium titanate thin film waveguide modulator," *Optics Express*, vol. 12, No. 24, pp. 5962–5967, 2004. [cited at p. 1]

[10] P. Tang, D. J. Towner, A. L. Meier, and B. W. Wessels, "Low-loss electrooptic BaTiO3 thin film waveguide modulator," *IEEE Phot. Tech. Lett*, vol. 16, No. 8, pp. 1837–1839, 2004. [cited at p. 1]

[11] M. Zgonik, P. Bernasconi, M. Duelli, R. Schlesser, and P. Gunter, "Dielectric, elastic, piezoelectric, electro-optic, and elasto-optic tensors of BaTiO3 crystals," *PHYSICAL REVIEW B*, vol. 50, No. 9, pp. 5941–5949, 1994. [cited at p. 1]

[12] A. Brimont, "Towards compact and high speed silicon modulators," Ph.D. dissertation, Universitat Politcnica de Valencia, 2011. [cited at p. 1]

[13] L. Liao, A. Liu, D. Rubin, J. Basak, Y. Chetrit, H. Nguyen, R. Cohen, N. Izhaky, and M. Paniccia, "40 Gbit/s silicon optical modulator for high speed applications," *Elect. Lett.*, vol. 43, No. 22, 2007. [cited at p. 1]

[14] D. J. Thomson, F. Y. Gardes, J. Fedeli, S. Zlatanovic, Y. Hu, B. P. P. Kuo, E. Myslivets, N. Alic, S. Radic, G. Z. Mashanovich, and G. T. Reed, "50-Gb/s silicon optical modulator," *IEEE Phot. Tech. Lett*, vol. 24, No. 4, pp. 234–236, 2012. [cited at p. 1]

[15] B. E. A. Saleh and M. C. Teich, *Fundamental of Photonic*. John Wiley & Sons, Inc., 1991. [cited at p. 1, 7, 9, 10, 11]

[16] H. Lee, G. Lee, S. K. Kim, H. Cheung, S. Kim, H. Kim, S. Hwang, Y. Oh, J. Jeong, and C. Shim, "Cost-effective 10-Gb/s optical duobinary transmission systems using a nonbuffered X-Cut LiNbO3 mach zehnder modulator," *IEEE Phot. Tech. Lett*, vol. 16, No. 4, pp. 1188–1190, 2004. [cited at p. 1]

[17] L. Wooten, K. Kissa, A. Yi-Yam, E. Murphy, D. Lafaw, P. Hallemeir, D. Maack, D. Attanasio, D. Fritz, G. McBrien, and D. Bossi., "A review of lithium niobate modulators for fiber-optic communications systems," *IEEE J. Sel. Top. Quantum Electron*, vol. 6, pp. 69–82, 2000. [cited at p. 1, 12, 13, 14, 18, 23]

[18] D. Tulli, "Micro-nano structured electro-optic devices in LiNbO3 for communication and sensing," Ph.D. dissertation, Institute de Ciencies Fotoniques & Universitat Politecnica de Catalunya, 2012. [cited at p. 1, 2, 11, 14]

[19] D.Janner, D. T. ad M. Jofre, D. Yudistira, S. Balsamo, M. Belmonte, and V. Pruneri, "Domain inverted acousto- and electrooptic devices and their application to optical communication, sensing, laser sources, and quantum key distribution," *IEEE J. Sel. Top. Quantum Electron*, vol. 19, N0. 6, 2013. [cited at p. 1, 2]

[20] C. Wen, "Coplanar waveguide: a surface strip transmission line suitable for nonreciprocal gyromagnetic device application," *IEEE Trans. Microwave Theory Tech*, vol. 17, pp. 1087 – 1090, December 1969. [cited at p. 1, 2, 18]

[21] R. W. Jackson, "Considerations in the use of coplanar waveguide for millimeter-wave integrated circuits," *IEEE Trans. Microwave Theory Tech*, vol. MTT-34, No. 12, pp. 1450–1456, 1986. [cited at p. 1, 2]

[22] K. Kubota, J. Noda, and O. Mikami, "Traveling wave optical modulator using a directional coupler LiNbO3 waveguide," *IEEE Journal of Quantum Electronics*, vol. QE-16, No. 7, pp. 754–760, 1980. [cited at p. 2]

[23] N. Dagli, "Wide-bandwidth lasers and modulators for RF photonics," *IEEE Trans. Microwave Theory Tech*, vol. Vol-47, No.7, pp. 1151–1171, 1999. [cited at p. 2, 3, 52]

[24] T. Kawanishi, "Parallel mach zehnder modulators for quadrature amplitude modulation," *IEICE Electronic Express*, vol. 8, No. 20, pp. 1678–1688, 2011. [cited at p. 2, 3]

[25] A. Kanno, T. Sakamoto, A. Chiba, T. Kawanishi, K. Higuma, M. Sudou, and J. Ichikawa, "120-Gb/s NRZ-DQPSK signal generation by a thin-lithium-niobate-substrate modulator," *IEICE Electronic Express*, vol. 7, pp. 817–822, 2010. [cited at p. 2, 3]

[26] I. L. Gheorma and G. Gopalakrishnan, "Flat frequency comb generation with an integrated dual parallel modulator," *IEEE Phot. Tech. Lett*, vol. 19, No. 13, pp. 1011–1013, 2007. [cited at p. 2]

[27] T. Sakamoto, T. Kawanishi, and M. Izutsu, "Optical frequency comb generation using asymmetrically dual driven mach-zehnder modulator," in *Proc. ECOC 2005, Vol. 3*, 2005. [cited at p. 2]

[28] D. Y. Kubo, R. Srinivasan, H. Kiuchi, and M. T. Chen, "Development of a mach-zehnder modulator photonic local oscilator source," *IEEE Trans. Microwave Theory Tech*, vol. 61, No. 8, pp. 3005–3013, 2013. [cited at p. 2]

[29] M. Doi, M. Sugiyama, K. Tanaka, and M. Kawai, "Advanced LiNbO3 optical modulators for broadband optical communications," *IEEE Journal of Selected Topics in Quantum Electronics*, vol. 12, No. 4, pp. 745–750, 2006. [cited at p. 2, 3, 78, 82]

[30] J. Ho-Ha and H. Jung, "Integrated-optic electric field sensors utilizing Ti:LiNbO3 mach-zehnder interferometric modulators," in *Opto-Electronics and Communications Conference (OECC)*, 2012. [cited at p. 2]

[31] L. Tsung-Hsin, H. Fu-Tsai, S. Wen-Tron, and L. Ching-Ting, "Electromagnetic field sensor using mach-zehnder waveguide modulator," *Microwave and Opt. Tech. Letters*, vol. 48, No. 9, pp. 1897–1899, 2006. [cited at p. 2]

[32] H. Porte, V. Gorel, and J. Goedgebuer, "Micromachined pressure sensor integrated with an imbalanced mach-zehnder waveguide on silicon for coherence modulation scheme," *Proc. SPIE 3555, Optical and Fiber Optic Sensor Systems*, vol. 194, 1998. [cited at p. 2]

[33] A. L. Kernec, M. S. B. Bnazet, J. Barbero, L. Peate, M. Maignan, I. Esquivias, F. Lopez, and N. Karafolas, "Space evaluation of optical modulators for microwave photonic on-board applications," in *International Conference on Space Optics, Rhodes, Greece*, 2010. [cited at p. 2]

[34] S. Bonino, R. Galeotti, L. Gobbi, M. Belmonte, and M. Bonazzoli, "High speed packaging solutions for LiNbO3 electro-optical modulator," in *Microelectronics and Packaging Conference*, 2009. [cited at p. 3]

[35] K. Aoki, J. Kondo, A. Kondo, T. Ejiri, T. Mori, Y. Mizuno, M. Imaeda, O. Mitomi, and M.Minakata, "Single-drive x-cut thin-sheet LiNbO3 optical modulator with chirp adjusted using asymmetric CPW electrode," *J. of Light. Tech*, vol. 24, No.25, pp. 2233 – 2237, 2006. [cited at p. 3, 4, 13, 47, 48, 59, 71, 72, 73, 74, 80, 114, 116, 117]

[36] H.Nagata, "Long-term DC drift in x-cut LiNbO3 modulators without oxide buffer layer," *IEE Proc. - Optoelectron.*, vol. 147, No. 5, pp. 350–354, 2000. [cited at p. 3]

[37] J. P. Salvestrini, L. Guilbert, M. Fontana, M. Abarkan, and S. Gille, "Analysis and control of the DC drift in LiNbO3 -based - mach zehnder modulators," *Journal of Lightwave Technology*, vol. 29, no. 10, pp. 1522–1534, 2011. [cited at p. 3]

[38] H. Nagata, H. Honda, and K. Akizuki, "Initial bias dependency in dc drift of z-cut LiNbO3 optical intensity modulators," *Opt. Eng.*, vol. 39, No. 4, pp. 1103–1105, 2000. [cited at p. 3]

[39] J. Kondo, K. Aoki, T. Ejiri, Y. Iwata, A. Hamajima, O. Mitomi, and M. Minakata, "Ti-diffused optical waveguide with thin LiNbO3 structure for high-speed and low-drive-voltage modulator," *IEICE TRANS. COMMUN*, vol. E89-B, No. 12, pp. 3428–3429, 2006. [cited at p. 4, 45, 69, 70]

[40] K. Noguchi, H. Miyazawa, and . Mitomi, "Frequency-dependent propagation characteristics of coplanar waveguide electrode on 100 GHz Ti:LiNb03 optical modulator," *Electronics Letters*, vol. 34, No. 7, pp. 661–663, 1998. [cited at p. 4]

[41] O. Mitomi, K. Noguchi, and H. Miyazawa, "Design of ultra-broad-band and LiNbO3 optical modulators with ridge structure," *IEEE Trans. Microwave Theory Tech*, vol. 34,No.9, pp. 2203 – 2207, 1995. [cited at p. 4]

[42] K. Noguchi, O. Mitomi, and H. Miyazawa, "Millimeter-wave Ti:LiNbO3 optical modulators," *J. of Light. Tech*, vol. 16,No.4, pp. 615 – 619, 1998. [cited at p. 4, 85]

[43] B. Rahman and S. Haxha, "Optimization of microwave properties for ultrahigh-speed etched and unetched lithium niobate electro-optic modulators," *J. of Light. Tech*, vol. 20, No.10, pp. 1856–1863, 2002. [cited at p. 4]

[44] S. Haxha, B. M. A. Rahman, and K. T. V. Grattan, "Bandwidth estimation for ultra-high-speed lithium niobate modulators," *Applied Optics*, vol. 42, No. 15, pp. 2674–2682, 2003. [cited at p. 4]

[45] J. Kondo, A. Kondo, K. Aoki, S. Takatsuji, . Mitomi, M. Imaeda, Y. Kozuka, and M. Minakata., "High-speed and low-driving-voltage x-cut LiNbO3 optical modulator with two step backside slot." *Elect. Lett.*, vol. 38,No.10, pp. 472 – 473, 2002. [cited at p. 4, 85, 114]

[46] J. Kondo, A. Kondo, K. Aoki, M. Imaeda, T. Mori, Y. Mizuno, S.Takatsuji, Y. Kozuka, O. Mitomi, and M. Minakata, "40-Gb/s x-cut LiNbO3 optical modulator with two-step back-slot structure," *Journal of Lightwave Technology*, vol. 20, No. 12, pp. 2110–2114, 2002. [cited at p. 4]

[47] T. Gorman and S. Haxha, "Thin layer design of X-Cut lithium niobate electrooptic modulator with slotted SiO2 substrate," *IEEE Phot. Tech. Lett*, vol. 20, No. 2, pp. 111–113, 2008. [cited at p. 4]

[48] T. Kishino, R. F. Tavlykaev, and R. V. Ramaswamy, "70+ um deep domain inversion in x-cut LiNbO3 and its use in a high-speed bandpass integrated-optic modulator," *Appl. Phys. Lett*, vol. 76, No. 26, pp. 3852–3854, 2000. [cited at p. 4]

[49] N. Courjal, H. Porte, A. Martinez, and J. Goedgebuer, "LiNbO3 mach zehnder modulator with chirp adjusted by ferroelectric domain inversion," *IEEE Phot. Tech. Lett*, vol. 14, No. 11, pp. 1509–1511, 2002. [cited at p. 4]

[50] D. Janner, D. Tulli, M. Garcia-Granda, M.Belmonte, and V. Pruneri, "Micro-structured integrated electro-optic LiNbO3 modulators," *Laser and Photon. Rev*, vol. 3, No. 3, pp. 301–313, 2009. [cited at p. 4]

[51] D. Janner, D. Tulli, M. Belmonte, and V. Pruneri, "Waveguide electro-optic modulation in micro-engineered LiNbO3," *Journal Of Optics A: Pure And Applied Optics*, vol. No.10, pp. 1–6, August, 2008. [cited at p. 4, 51]

[52] J. Ichikawa, "Technical trends of LiNbO3 optical modulators," Sumitomo Osama Cement Co. Ltd., Tech. Rep., 2008. [cited at p. 4, 114]

[53] F. Lucchi, D. Janner, M. Belmonte, S. Balsamo, M. Villa, S. Giurgola, P. Vergani, and V. Pruneri, "Very low voltaje single drive domain inverted LiNbO3 integrated electro-optic modulator." *Opt. Exp*, vol. 15, No. 17, pp. 10 739–10 743, 2007. [cited at p. 6, 57, 58, 59, 85, 117]

[54] O. Mitomi, K. Noguchi, and H. Miyazaka, "Broadband and low driving-voltage LiNbO3, optical modulators," *IEEE Proc. Optoelectron*, vol. 145, No.6, pp. 360 – 364, 1998. [cited at p. 6, 12, 51, 52, 53]

[55] A. Chowdhury and L. McCaughan, "Figure of merit for near-velocity-matched traveling-wave modulators," *Optics Letters*, vol. 26, No. 17, pp. 1317–1319, September 2001. [cited at p. 6, 51, 56]

[56] C. M. Kim and R. V. Ramaswamy, "Overlap integral factors in integrated optic modulators and switches," *Journal of Lightwave Technology*, vol. 7, No. 7, pp. 1063–107, 1989. [cited at p. 11, 13, 14, 15, 16, 70, 114, 117]

[57] D. Marcuse, "Optimal electrode design for integrated optics modulators," *IEEE Journal of Quantum Electronics*, vol. QE-18, No. 3, pp. 393–398, 1982. [cited at p. 13, 14, 15, 16]

[58] O. G. Ramer, "Integrated optic electrooptic modulator electrode analysis," *IEEE Journal of Quantum Electronics*, vol. QE-18, No. 3, pp. 386–392, 1982. [cited at p. 13, 70]

[59] H. Jin, M. Belanger, and Z. Jakubczyk, "General analysis of electrodes in integrated-optics electrooptic devices," *IEEE Journal of Quantum Electronics*, vol. 27, No. 2, pp. 243–251, 1991. [cited at p. 13]

[60] R. Becker and B. Kincaid, "Improved electrooptic efficiency in guided-wave modulators," *Journal of Lightwave Technology*, vol. 11, No. 12, pp. 2076–2079, 1993. [cited at p. 14, 16, 81]

[61] a. M. W. K. Burns and R. P. Moeller, "Performance and modeling of proton exchanged LiTaO3 branching modulators," *Journal of Lightwave Technology*, vol. 10, No. 10, pp. 1403–1407, 1992. [cited at p. 16]

[62] G. E. Ponchak, M. Matloubian, and L. P. B. Katehi, "A measurement-based design equation for the attenuation of MMIC-compatible coplanar waveguides," *IEEE Trans. On Micro. Theo. And Tech.*, vol. Vol. 47, No. 2, pp. 241–243, 1999. [cited at p. 18]

[63] R. Simons, *Coplanar Waveguide Circuits, Components, and System.* John Wiley & Sons, Inc., 2001. [cited at p. 18]

[64] Y. Huang, "Calculations of microwave parameters of CPW with buffer layer," in *Proc. Int. Conf. on Microw. and Millimeter Wave Tech. 2002*, 2002. [cited at p. 19]

[65] G. Ghione and M. Goano, "The influence of ground-plane width on the ohmic losses of coplanar waveguides," *IEEE Transactions on Microwave Theory and Techniques*, vol. 45, No. 9, pp. 1640 – 1642, Sept. 1997. [cited at p. 19]

[66] M. Kobayashi and R. Terakado, "New view on an anisotropic medium and its application to transformation from anisotropic to isotropic problems," *IEEE Tr*, vol. MTT-27, pp. 769–775, 1979. [cited at p. 20]

[67] M. Frankel, S. Gupta, J. A. Valdmanis, and G. A. Mourou, "Terahertz attenuation and dispersion characteristics of coplanar transmission lines," *IEEE Transactions on Microwave Theory and Techniques*, vol. 39, pp. 910–916, June 1991. [cited at p. 23, 24, 30, 90, 105]

[68] F. Schnieder, T. Tischler, and W. Heinrich, "Modeling dispersion and radiation characteristics of conductor backed cpw with finite ground width," *IEEE Trans. Microwave Theory Tech*, vol. 51, No.1, pp. 137 – 143, Jan. 2003. [cited at p. 23, 30, 90, 105]

[69] G. Ghione and C. Naldi, "Coplanar waveguides for MMIC applications: effects of upper shielding, conductor backing, finit-extent ground planes and line-to-line coupling," *IEEE Trans. Microwave Theory Tech*, vol. 35, No.3, pp. 260–267, Mar 1987. [cited at p. 23, 25, 26, 36]

[70] R. C. Alferness, "Waveguide electrooptic modulators," *IEEE Trans. Microwave Theory Tech*, vol. MTT-30, No. 8, pp. 1121–1137, 1982. [cited at p. 23, 51]

[71] E. J. Denlinger, "Losses of microstrip lines," *IEEE Trans. Microwave Theory Tech*, vol. MTT-28, No. 6, pp. 513–522, 1980. [cited at p. 24]

[72] R. A. Pucel, D. J. Masse, and C. P. Hartwig, "Losses in microstrip," *IEEE Trans. Microwave Theory Tech*, vol. MTT-16, No. 16, pp. 342–350, 1968. [cited at p. 24]

[73] H. Chung, W. Chang, and G. E. Adler, "Modelling and optimization of traveling-wave LiNbO3 interferometric modulators," *IEEE J. of Quantum Electronics*, vol. 27, No.3, pp. 608 – 617, March 1991. [cited at p. 24, 25, 28, 33, 60, 90]

[74] W. Heinrich, "Quasi-TEM description of MMIC coplanar lines including conductor-loss effects." *IEEE Trans. Microwave Theory Tech*, vol. 41, pp. 45 – 52, Jan 1993. [cited at p. 24, 25, 28, 90]

[75] V. F. Hanna and D. Thebault, "Theoretical and experimental investigation of asymmetric coplanar waveguides," *IEEE Trans. Microwave Theory Tech*, vol. MTT-32, no. 12, pp. 1649–1651, 1984. [cited at p. 25]

[76] S. S. Bedair and I. Wolff, "Fast, accurate and simple approximate analytic formulas for calculating the parameters of supported coplanar waveguides for (M)MICs ," *IEEE Trans. Microwave Theory Tech*, vol. 40, No. 1, pp. 41–48, 1992. [cited at p. 25]

[77] S. Gevorgian, P. Linnr, and E. Kollberg., "CAD models for shielded multilayered CPW." *IEEE Trans. Microwave Theory Tech*, vol. 43,No.43, pp. 772–779, April 1995. [cited at p. 25, 33, 37, 38, 39, 107]

[78] E. Chen and S. Y. Chou, "Characteristics of coplanar transmission lines on multilayer substrates: Modeling and experiments," *IEEE Trans. Microwave Theory Tech*, vol. 45, No. 6, pp. 939–945, 1997. [cited at p. 25]

[79] K. C. Gupta, R. Garg, and I. J. Bahl, *Microstrip Lines and Slotlines*, M. A. H. Norwood, Ed., 1979. [cited at p. 27]

[80] H. A. Wheeler, "Transmission line properties of parallel strips separated by a dielectric sheet," *IEEE Trans. Microwave Theory Tech*, vol. 13, no. 2, 1965. [cited at p. 27]

[81] M. V. Schneider, "Microstrip lines for microwaves integrated circuits," *Bell Syst. Tech. J.*, vol. 48, pp. 1421–1444, 1969. [cited at p. 28]

[82] E. Rodriguez, "Study and characterization of coplanar transmission lines for electro-optic modulators design and optimization," Master's thesis, Universitat Politecnica de Catalunya, 2008. [cited at p. 28]

[83] H. Wheeler, "Formulas for the skin effect," *Proc IRE*, vol. 30, pp. 412 – 424, 1942. [cited at p. 28, 32, 33, 39]

[84] G. Ghione and M. Goano, "Revisiting the partial-capacitance approach to the analysis of coplanar transmission lines on multilayered substrates," *IEEE Trans. Microwave Theory Tech*, vol. 51, No. 9, pp. 2007–2014, 2003. [cited at p. 29, 36, 37, 38]

[85] J. A. Ibarra-Fuste and M. C. Santos-Blanco, "Compact closed form expression for the propagation parameters of a finite ground width CPW with thick electrodes," *IET Microw. Antennas Propag.*, vol. 6, pp. 269 – 275, Feb. 2012. [cited at p. 31, 41]

[86] J. A. Ibarra Fuste and M. C. Santos Blanco, "Closed-form expressions for the optimization of high speed electro-optical modulators," *Optics and Laser Technology*, vol. 49, pp. 296–300, 2013. [cited at p. 31]

[87] G.Ghione, M. Goano, G. Madonna, G.Omegna, M. Pirola, S. Bosso, D. Frassati, and A. Perasso, "Microwave modeling and characterization of thick coplanar waveguides on oxide coated lithium niobate substrates for electrooptical applications," *IEEE Trans. Microwave Theory Tech*, vol. 47, No. 12, pp. 2287 – 2293, December,1999. [cited at p. 38]

[88] D. Janner, M. Belmonte, and V. Pruneri, "Tailoring the electrooptic response and improving the performance of integrated LiNbO3 modulators by domain engineering," *J. of Light. Tech*, vol. 25, No.9, pp. 2402–2408, 2007. [cited at p. 51]

[89] J. A. Ibarra Fuste and M. C. Santos Blanco, "Bandwidth-length trade-off figures of merit for electro-optic traveling wave modulators," *Optics Letters*, vol. 38, Iss. 9, pp. 1548–1550, 2013. [cited at p. 55]

[90] K. Noguchi, . Mitomi, K. Kawano, and M. Yanagibashi, "Highly efficient 40-GHz bandwidth Ti:LiNbO3, optical modulator employing ridge structure," *IEEE Phot. Tech. Lett*, vol. 5, No. 1, pp. 52–54, 1993. [cited at p. 57, 59]

[91] K. Aoki, J. Kondo, Y. Iwata, A. Hamajima, T. Ejiri, O. Mitomi, and M. Minakata, "High-speed, low-driving-voltage and small-footprint x-cut thin LiNbO3 sheet optical modulator with a folded mach-zehnder waveguide," in *European Conference on Optical Communications. ECOC 2006.*, 2006. [cited at p. 57, 58, 80, 85, 117]

[92] M. Rangaraj, T. Hosoi, and M. Kondo, "A wide-band Ti:LiNbO3, optical modulator with a conventional coplanar waveguide type electrode," *IEEE Photonics Technology Letters*, vol. 4, No. 9, pp. 1020–1022, 1992. [cited at p. 57, 59]

[93] M. Minakata, "Recent progress of 40 GHz high-speed LiNbO3 optical modulator," *Proceedings of SPIE*, vol. 4532, pp. 16–27, 2001. [cited at p. 57, 59, 67]

[94] K. Aoki, J. Kondo, Y. Iwata, A. Hamajima, T. Ejiri, O. Mitomi, and M. Minakata, "High- speed x-cut thin-sheet LiNbO3 optical modulator with folded structure," *Journal of Lightwave Technology*, vol. 25, No.7, pp. 1805–1810, 2007. [cited at p. 61, 62, 63, 71, 73, 74, 75, 76, 77, 85, 116, 117]

[95] G. K. Gopalakrishnan, C. H. Bulmer, W. K. Burns, R. W. McElhanon, and A. S. Greenblatt, "40 GHz, low half-wave voltage Ti: LiNbO3 intensity modulator," *Electronics Letters*, vol. 28, No. 9, pp. 826–827, 1992. [cited at p. 61, 62, 63, 71, 76, 77, 78, 79, 116, 117]

[96] A. B. White, "Numerical solution of two-point boundary-value problems," Ph.D. dissertation, California Institute of Technology, 1974. [cited at p. 70]

[97] K. Aoki, J. Kondo, A. Kondo, T. Mori, Y. Mizuno, S.Shimodaira, M. Imaeda, Y.Kozuka, O. Mitomi, and M. Minakata, "High-performance optical modulator with a wide center electrode and thin x-cut LiNbO3 substrate," *IEEE Phot. Tech. Lett*, vol. 16, No. 12, pp. 2610–2612, 2004. [cited at p. 80]

[98] A. H. Land and A. G. Doig, "An automatic method of solving discrete programming problems," *Econometrica*, vol. 28, No. 3, p. 497520, 1960. [cited at p. 84]

[99] F. Y. Gan, "Traveling wave electrode design for high speed LiNbO3 intensity modulators," Ph.D. dissertation, McGill University, 1996. [cited at p. 97]

[100] D. M. Pozar, *Microwave Engineering*. Wiley and Sons, 1997. [cited at p. 99]

[101] R. E. Collin, *Foundation for Microwave Engineering*. John Wiley and Sons, 2001. [cited at p. 103]